Project No. 12-3363

Advanced Reactors-Intermediate Heat Exchanger (IHX) Coupling: Theoretical Modeling and Experimental Validation

Reactor Concepts Research Development and Demonstration (RDRD&D)

Vivek Utgikar

University of Idaho

In collaboration with:

The Ohio State University

Carl Sink, Federal POC

Michael McKellar, Technical POC

NEUP Nuclear Energy University Programs

U.S. Department of Energy

Final Report

Project Title:	Advanced Reactors-Intermediate Heat Exchanger (IHX) Coupling: Theoretical Modeling and Experimental Validation
Date of Report:	December 29, 2016
Milestone Level:	2
Recipient:	University of Idaho Office of Sponsored Programs P.O. Box 443020 Moscow ID 83844
Award Number:	128504
Project Number:	12-3363
Project Period:	September 10, 2012 – September 30, 2016
Principal: Investigator	Utgikar, Vivek 208-885-6970 vutgikar@uidaho.edu
Collaborators:	Sun, Xiaodong (The Ohio State University) 614-247-7646 Sun.200@osu.edu Christensen, Richard N. (The Ohio State University/University of Idaho) 208-533-8102 rchristensen@uidaho.edu Sabharwall, Piyush (Idaho National Laboratory) 208-526-6494 piyush.sabharwall@inl.gov
TPOC	Michael McKellar
Federal Manager	Carl Sink
Workscope	NGNP-2

Executive Summary

Goals, Objectives, and Approach

The overall goal of the research project was to model the behavior of the advanced reactor-intermediate heat exchange system and to develop advanced control techniques for off-normal conditions. The specific objectives defined for the project were:

1. To develop the steady-state thermal hydraulic design of the intermediate heat exchanger (IHX);
2. To develop mathematical models to describe the advanced nuclear reactor-IHX-chemical process/power generation coupling during normal and off-normal operations, and to simulate models using multiphysics software;
3. To develop control strategies using genetic algorithm or neural network techniques and couple these techniques with the multiphysics software;
4. To validate the models experimentally

The project objectives were accomplished by defining and executing four different tasks corresponding to these specific objectives. The first task involved selection of IHX candidates and developing steady state designs for those. The second task involved modeling of the transient and off-normal operation of the reactor-IHX system. The subsequent task dealt with the development of control strategies and involved algorithm development and simulation. The last task involved experimental validation of the thermal hydraulic performances of the two prototype heat exchangers designed and fabricated for the project at steady state and transient conditions to simulate the coupling of the reactor-IHX-process plant system. The experimental work utilized the two test facilities at The Ohio State University (OSU) including one existing High-Temperature Helium Test Facility (HTHF) and the newly developed high-temperature molten salt facility.

Accomplishments and Outcomes

The summary of these activities conducted and the resulting outcomes is as follows:

- Steady state designs for four different candidate compact heat exchanger designs – Wavy-Channel Printed Circuit Heat Exchanger (PCHE), Offset Strip-Fin Heat Exchanger (OSFHE), Helical Coil Heat Exchanger (HCHE), and Twisted Tube Heat Exchanger (TTHE) – were completed for various combinations of primary and secondary heat transfer media that included helium and fluoride salts.

- Mathematical models for describing the transient behavior of the advanced reactor-IHX-process application system were developed. Model simulations were conducted through development of MATLAB programs, as well as by using commercially available process simulation programs PRO/II and Dynsim.
- The system was analyzed with respect to possible disturbances and their impacts on the system. Three control blocks – Reactor, Intermediate Heat Exchanger (IHX), and Secondary Heat Exchanger (SHX) – were defined. Controlled variables, manipulated variables and load variables (disturbances) were identified for each block. Transfer functions relating the controlled variables to the manipulated and load variables were developed for the SHX and IHX blocks. Stability analysis and estimation of controller parameters was conducted on the basis of the transfer functions.
- Dynamics and control of the system were simulated for various scenarios using user developed MATLAB codes. It was found that the disturbances in the primary loop had an overall greater impact on the system than the disturbances in other loops. It may be best to have a control strategy in which the manipulated variables depend on where the disturbance occurs. In addition, switching of the manipulated variable after a certain pre-set limit ($\pm$20% change in the manipulated variable) was reached for that variable was investigated. This limit is reached for large temperature disturbances in the system, which triggered a switching of the manipulated variables. Using this approach, the system was able to control the variables at their set points.
- The behavior of the system under a comprehensive control scheme, where the nuclear reactor operation is also controlled, was also simulated. The reactor model included the point kinetic equations with 3 groups of delayed neutrons, which achieved the best balance between the computational load and accuracy. Various control options were investigated that included manipulating flow rates, or reactor power or a combination thereof. Each option was successful in resetting the controlled variables to their set points.
- A comprehensive model was developed to obtain the dynamics of the helium Brayton Cycle PCS in response to any system disturbances. Temperature transients of various streams in response to different disturbance stimuli were obtained indicating the utility of this approach.
- Prototype wavy-channel (zigzag) printed circuit heat exchanger (PCHE) and helically-coiled twisted tube heat exchangers were designed and fabricated for experimental testing. Experiments were also conducted with an available straight channel PCHE.
- The PCHE testing was conducted in the HTHF. Experimental data were obtained by introducing disturbances in the laboratory and monitoring the response. Transient numerical models

developed for the PCHE were run and validated by comparison with the dynamic test data. The data indicate that the transient model can accurately predict the behavior of the system.

- Thermal-hydraulic performance testing of the helically-coiled fluted tube heat exchanger was conducted under water to water conditions. Experimental data were analyzed for the pressure drop, thermal duty, heat loss, and heat exchanger effectiveness aspects. The heat exchanger effectiveness values obtained from the experiments compared well with those obtained from theoretical calculations.

Refereed Journal Publications

A) Published

1. Bartel N, Chen M, Utgikar VP, Sun X, Kim I-H, Christensen R, Sabharwall P. 2015. Comparison of compact heat exchangers for application as the intermediate heat exchanger for advanced nuclear reactors. *Annals of Nuclear Energy*, 81: 143-149.
2. Chen M, Kim I, Sun X, Christensen RN, Utgikar V, Sabharwall P. 2015. Transient analysis of an FHR coupled to a helium Brayton cycle. *Progress in Nuclear Energy*, 83: 283-293.
3. Skavdahl I, Utgikar V, Sabharwall P, Chen M, Sun X, Christensen R. 2016. Modeling and Simulation of Control System Response to Temperature Disturbances in a Coupled Heat Exchangers-AHTR System. *Nuclear Engineering and Design*, 300: 161-172, DOI 10.1016/j.nucengdes.1016.01.010.
4. Skavdahl I, Utgikar V, Christensen R, Chen M, Sun X, Sabharwall P. 2016. Control of Advanced Reactor-Coupled Heat Exchangers System: Incorporation of Reactor Dynamics in System Response to Load Disturbances. *Nuclear Engineering and Technology*, 48: 1349-1359, DOI: 10.1016/j.net.2016.05.001.
5. Chen M, Sun X, Christensen R, Shi S, Skavdahl I, Utgikar V, Sabharwall P. 2016. Experimental and Numerical Study of a Printed Circuit Heat Exchanger. *Annals of Nuclear Energy*, 97: 221-231, DOI 10.1016/j.anucene.2016.07.010.
6. Chen M, Sun X, Christensen R, Skavdahl I, Utgikar V, Sabharwall P. 2016. Pressure Drop and Heat Transfer Characteristics of a High-temperature Printed Circuit Heat Exchanger. *Applied Thermal Engineering*, 108: 1409-1417, DOI 10.1016/j.applthermaleng.2016.07.149.

B) In Progress

1. Chen M, Sun X, Christensen RN, Skavdahl I, Utgikar V, and Sabharwall P. “Transient Analysis of a High-Temperature Printed Circuit Heat Exchanger: Numerical Modeling and Experimental Investigation,” submission to *Nuclear Engineering and Design*. (In revision)

2. Skavdahl I, Utgikar V, Torres C, Chen M, Sun X, Christensen R, Sabharwall P. "Determination of the Dynamic Behavior of the Advanced Reactor-Heat Exchanger System using Process Simulation Softwares," submission to *Journal of Thermal Science and Engineering Applications* (In review).

Conference Papers and Presentations

1. "Thermal-Hydraulic Design of Wavy-Channel Printed Circuit Heat Exchangers," N Bartel, V Utgikar, M Chen, X Sun, I-H Kim, R Christensen, P Sabharwall, 2013 ANS Annual Meeting, June 2013, Atlanta, Georgia.
2. "Design of Printed Circuit Heat Exchangers for Very High Temperature Reactors," M Chen, X Sun, I-H Kim, R Christensen, N Bartel, V Utgikar, P Sabharwall, 2013 ANS Annual Meeting, June 2013, Atlanta, Georgia.
3. "Dynamic Response Analysis of a Scaled-Down Offset Strip-Fin Intermediate Heat Exchanger," M Chen, I-H Kim, X Sun, RN Christensen, N Bartel, V Utgikar, and P. Sabharwall, 2013 ANS Winter Meeting, November 2013, Washington, DC.
4. "Transient Model of Wavy-Channel Printed Circuit Heat Exchangers," N Bartel, V Utgikar, P Sabharwall, M Chen, X Sun, I-H Kim, RN Christensen, 2013 ANS Winter Meeting, November 2013, Washington, DC.
5. "Transient Analysis of Advanced High Temperature Reactors Using Process Simulation Software," I Skavdahl, V Utgikar, P Sabharwall, M Chen, X Sun, I-H Kim, RN Christensen, 2014 ANS Winter Meeting, November 2014, Anaheim, California.
6. "Preliminary Design of a Helical Coil Heat Exchanger for a Fluoride Salt-Cooled High-Temperature Test Reactor," M Chen, I Kim, X Sun, RN Christensen, I Skavdahl, V Utgikar, and P Sabharwall, 2014 ANS Winter Meeting, November 2014, Anaheim, California.
7. "Control Strategy Development of Advanced High Temperature Reactor System," I Skavdahl, V Utgikar, P Sabharwall, M Chen, X Sun, R Christensen, 2015 Annual Meeting of the ANS, June 2015, San Antonio, Texas.
8. "Simulation of Advanced High Temperature Reactor Control System using MATLAB," I Skavdahl, V Utgikar, P Sabharwall, M Chen, X Sun, R Christensen, 2015 Winter meeting of the American Nuclear Society (ANS), November 2015, Washington, DC.
9. "Development of a Thermal-Hydraulic Analysis Code for an FHR," M Chen, X Sun, RN Christensen, S Shi, I Skavdahl, V Utgikar, P Sabharwall, 11th International Topical Meeting on Nuclear Reactor Thermal Hydraulics, Operation and Safety (NUTHOS-11), October 2016, Gyeongju, South Korea.

10. “Experimental and Numerical Study of Heat Transfer and Pressure Drop in a High-Temperature Printed Circuit Heat Exchanger,” M Chen, S Shi, X Sun, RN Christensen, I Skavdahl, V Utgikar, P Sabharwall, 8th International Topical Meeting on High Temperature Reactor Technology 2016 (HTR2016), November 2016, Las Vegas, NV.
11. “Helium Brayton Cycle Design for Advanced High Temperature Reactor System,” I Skavdahl, V Utgikar, R Christensen, P Sabharwall, M Chen, X Sun, 2016 ANS Winter Meeting, November 2016, Las Vegas, NV.

Mentoring of Students

1. Isaac Skavdahl, M.S. (Major: Chemical Engineering), University of Idaho, Spring 2016. Thesis: *Analysis of transients and control of advanced high temperature reactor-coupled heat exchangers system*.
2. Minghui Chen, M.S. (Major: Nuclear Engineering), The Ohio State University, Summer 2015. Thesis: *Design, fabrication, testing, and modeling of a high-temperature printed circuit heat exchanger*.
3. Minghui Chen, Ph.D. (Major: Nuclear Engineering), The Ohio State University, In Progess. Dissertation: *Performance testing and Dynamic modeling of high-temperature heat exchangers for an FHR*.
4. Cesar Torres, B.S. (Major: Chemical Engineering), University of Idaho, Fall 2015. Undergraduate research assistant.
5. Michael Cron, B.S. (Major: Chemical Engineering), Spring 2014. Undergraduate research assistant.
6. Nathan Bartel, M.S. (Major: Nuclear Engineering), University of Idaho.

Table of Contents

REPORT NARRATIVE

1. Introduction

Advanced reactors (such as the high temperature gas-cooled reactor – HTGR, or advanced high temperature reactor – AHTR) from the Gen IV program are required to deliver electricity and process heat with high efficiency. The electric power production may be through a high-pressure steam generator (Rankine cycle) or a direct- or indirect-cycle gas turbine (Brayton cycle). The process heat applications may include co-generation, coal-to-liquids conversion, and synthesis of chemical feedstocks. The process heat applications of these advanced reactors are critically dependent upon an effective intermediate heat exchanger (IHX), which is a key component transferring heat from the primary coolant to a secondary coolant as shown in Figure 1.1. The secondary coolant will then further transfer heat to a chemical process or a power conversion system (Sabharwall et al., 2009; 2010). The IHX also serves as the primary coolant boundary, and must be robust enough to maintain system integrity under normal and abnormal conditions.

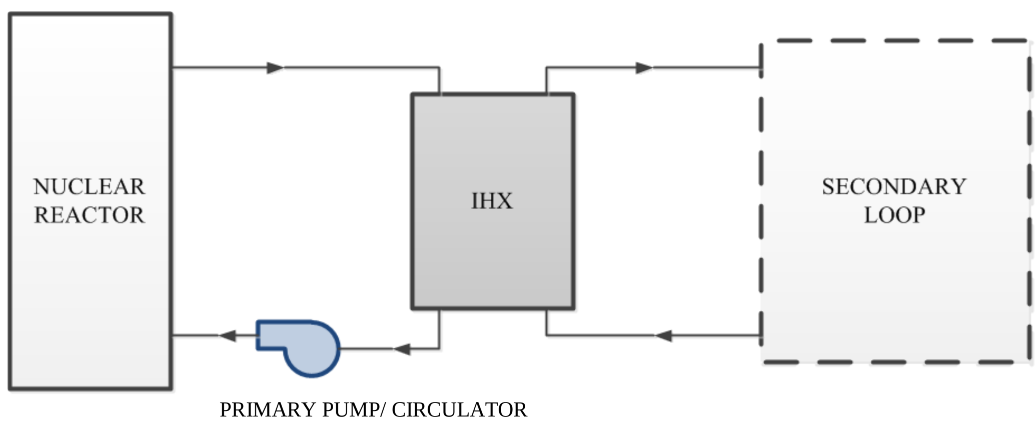

Figure 1.1 A schematic showing the coupling of the reactor and the secondary loop via an IHX.

Several candidate designs for IHX are available, with the final decision still to be made. These designs include shell-and-tube, helical coil, and compact heat exchangers: plate-and-fin, and micro-channel (printed circuit heat exchangers or PCHEs). The secondary heat transfer medium may be helium (power generation through Brayton cycle), water (power generation through Rankine cycle), or molten salts (process heat applications).

Despite its significance, the safety implications of the nuclear reactor-IHX-chemical process coupling/power generation have not received much attention. Little information is available on the transient behavior of the advanced reactor-IHX system, particularly under abnormal conditions. And yet, this information is critical for the overall safety assessment of the reactor system and therefore for regulatory design certification review. The normal and off-normal behavior of these reactors differs from those of conventional light water reactors. The complexity of the system requires the development of advanced techniques to ensure proper control of the system. This research was conducted to fulfill this need through the development and application of these advanced techniques to the advanced reactor-IHX system. The theoretical results were validated through experiments at The Ohio State University.

1.1 Goals and Objectives

The overall goal of the proposed research was to model the behavior of the Advanced Reactor-IHX-Chemical Process/Power Generation system and develop advanced control techniques for off-normal conditions. The specific objectives defined for the project were:

1. To develop the steady-state thermal hydraulic design of the intermediate heat exchanger (IHX);
2. To develop mathematical models to describe the advanced nuclear reactor-IHX-chemical process/power generation coupling during normal and off-normal operations, and to simulate models using multiphysics software;
3. To develop control strategies using genetic algorithm or neural network techniques and couple these techniques with the multiphysics software;
4. To validate the models experimentally.

1.2 Research Approach and Methods

The above objectives were accomplished through the execution of the tasks described below:

Task 1: Steady-State Thermal Hydraulic Design of IHX

Candidate heat exchangers types were identified for the IHX application for different combinations of Primary and secondary coolants and the thermal hydraulic designs developed for the IHXs operating under various steady-state conditions. Heat exchangers were specified with respect to the design requirements of output power, inlet and outlet temperatures and mass flow rates of the streams.

Task 2: Modeling of the IHX under Transient and Off-Normal Conditions

The second task involved modeling the behavior of the reactor-IHX system under transient and off-normal conditions. The transient conditions involved changes in the reactor power output as well as demand changes from the secondary side (power generation and process applications) due to variations in flow rates and fluid temperatures.

Task 3: Devising Control Strategy

The complexity of the system requires advanced control techniques to ensure operational safety. Detailed analysis of the system was conducted to identify the system disturbances (load variables), controlled variables, and manipulated variables. Mathematical models were developed to describe the relationships (transfer functions) between the various variables, and controllers specified for the system. The control system response was simulated for various flow and temperature disturbances.

Task 4: Experimental Validation

Prototype IHXs were designed and fabricated for the experimental validation of the system models. Experiments were conducted using the two test facilities – the high-temperature helium test facility (HTHF) and the high-temperature molten salt facility at The Ohio State University – to examine the thermal performance of these IHXs at steady state and transient conditions and to simulate the coupling of the reactor-IHX-process system.

The activities conducted and results obtained through the research are described in the following sections, with each section presenting details corresponding to each of the four tasks.

2. Steady State Thermal Hydraulic Design of Heat Exchangers

A literature search of the candidate IHXs was the first step to understanding their applicability to the nuclear reactor-IHX-chemical process/power generation plant. The literature search helped identify the printed circuit heat exchanger (PCHE) and offset strip-fin PCHE as the primary candidates. Helical coil heat exchanger and the twisted tube heat exchanger were the other two candidates identified as of interest.

Operational Parameters

The operational parameters for the heat exchanger designs were modified from the NGNP reference VHTR system from the Gen-IV Program (Oh and Kim, 2008). The Reactor Outlet Temperature (ROT) has been decreased from 900 °C to 800 °C due to material concerns and the mass flow rate [kg/s] was balanced. These operating conditions are shown in Table 2.1 for the Helium/Helium primary and secondary loop fluid combination.

Table 2.1. Operating Conditions for the 600 MW_{th} Design

Parameters	Hot Channel In	Hot Channel Out	Cold Channel In	Cold Channel Out
Fluid	Helium		Helium	
T [°C]	800	543	520	776
P [MPa]	7	6.95	7.97	7.92
$\dot{m}$ [kg/s]	450	450	450	450
ρ [kg/m^3]	3.117	4.059	4.78	3.603
c_p [kJ/kg-K]	5.19	5.19	5.19	5.19
k [W/m-K]	0.3822	0.3164	0.3106	0.3767
μ [kg/m-s]	4.859e-05	4.008e-05	3.929e-05	4.783e-05
Prandtl Number	0.66	0.66	0.66	0.66

The different heat exchangers and their thermal hydraulic designs are described below:

2.1 Printed Circuit Heat Exchanger (PCHE)

A PCHE is a type of compact heat exchanger where the coolant flow channels are photo-chemically etched on one side of thin plates. The fluid passages are approximately semicircular in cross-section. These plates are then formed into a heat exchanger core through a diffusion bonding process that includes a thermal soaking period to allow grain growth. This diffusion bonding process enables an interface-free join between the plates and gives the base material strength and a very high pressure containment capability (Hesselgreaves, 2001). One type of configuration for the physical geometry of the PCHE core is shown in Figure 2.1.

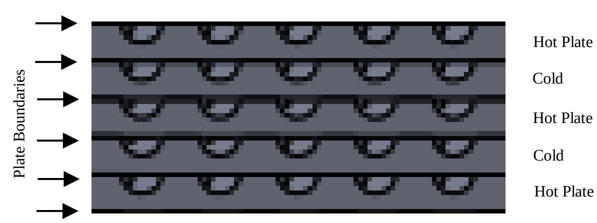

Figure 2.1. PCHE Core Geometry

There are three different channel geometries that have been prevalent in research literature: straight channels, wavy channels, and an offset strip-fin configuration where the flow channels are discontinuous. The geometry of a wavy channel is shown in Figure 2.2. The effects of the channel bends interrupts the boundary layer and cause local reverse flows and eddies to form which in turn increases the Nusselt number of the fluid and the overall heat transfer of the channels. The wavy channel geometry also effects the overall pressure drop across the PCHE as the pitch angle, ϕ, increases.

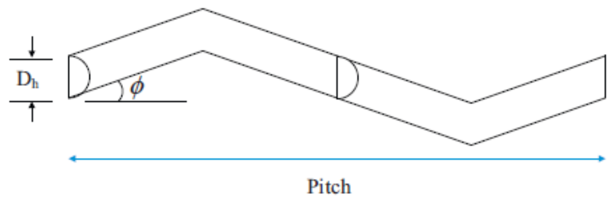

Figure 2.2. Wavy Channel Geometry (Kim and No, 2012)

The full-scale thermal hydraulic design of the helium/helium wavy channel and offset strip-fin PCHE is described below. The following assumptions were made for the design: the heat exchanger operates at steady state, flow distribution in each channel is uniform, the hot and cold plates have equivalent geometry, the flow passages are approximately semicircular, and heat loss from the PCHE surface is neglected.

Wavy Channel PCHE:

The flow regime for a semicircular duct can be defined as follows: the laminar region $\left(\mathrm{Re} < 2300\right)$, the transitional region $\left(2300 \le \mathrm{Re} \le 10{,}000\right)$, and the turbulent region $\left(\mathrm{Re} \ge 10{,}000\right)$.

Laminar Region – Wavy Channel PCHE

The laminar region of semicircular channels in PCHEs has been characterized by Hesselgreaves as occurring below a Reynolds number of 2300. According to research done by Mylavarapu (2011) the transition regime occurs at a value much lower than 2300, approximately 1700. The wavy channels provide constant boundary layer interruption; this makes it very hard to identify where the flow regime becomes transitional because it is believed that boundary layer effect is much greater than the transitional flow effect. For the sake of brevity, we will assume that the corresponding critical Reynolds number identified by Mylavarapu is acceptable for design calculations.

Laminar Flow - Overall Pressure Drop Characteristics:

The Fanning friction factor is used to find the overall pressure drop across the PCHE. The straight channel Fanning friction factor correlation suggested by Hesselgreaves (2001) for the laminar region is given by,

$$f\,\mathrm{Re} = 15.78 \qquad \left(\mathrm{Re} < 2300\right) \qquad (2.1)$$

Kim and No (2012) proposed a new correlation modifying Equation 2.1 by using fitting constants for wavy channel geometries. The fitting constants are dependent on channel pitch angle, ϕ, and single pitch length. The modified correlation is,

$$f\,\mathrm{Re} = 15.78 + a\,\mathrm{Re}^{b} \quad \left(\mathrm{Re} < 2300\right) \tag{2.2}$$

A selection of the fitting constants appropriate to the PCHE geometry is shown in Table 2.2.

Table 2.2. Fanning Friction Factor Fitting Constants (Kim and No, 2012)

Angle, ϕ	a	b	RMS error of the correlation
10°	0.01775	0.90795	1.319%
15°	0.06455	0.81021	1.104%
20°	0.08918	0.8136	0.876%

Laminar Flow - Heat Transfer Characteristics:

The Nusselt number is defined as the ratio of convective to conductive heat transfer orthogonal to a boundary (in this case, the heat exchanger flow channel surface). The Nusselt number can be found using the correlation below (Hesselgreaves, 2001):

$$\mathrm{Nu} = 4.089 \quad \left(\mathrm{Re} < 2300\right) \tag{2.3}$$

Kim and No (2012) proposed a correlation modifying equation 2.3 by using fitting constants for wavy channel geometries. The fitting constants are dependent on channel pitch angle, ϕ, and single pitch length. The modified correlation is shown next,

$$\mathrm{Nu} = 4.089 + c\,\mathrm{Re}^{d} \quad \left(\mathrm{Re} < 2300\right) \tag{2.4}$$

A selection of fitting constants appropriate to the PCHE geometry is shown in Table 2.3.

Table 2.3. Nusselt Number Fitting Constants (Kim and No, 2012)

Angle, ϕ	c	d	RMS error of the correlation
10°	0.0022	0.99841	0.459%
15°	0.00544	0.91361	1.849%
20°	0.00894	0.86708	1.589%

Two different semicircular channel diameters: 1.5 and 2 mm, corresponding to the hydraulic diameters of 0.922 and 1.2 mm, were considered. For the full scale 600 MW_{th} intermediate heat exchanger configuration, the thermal duty was split between ten 60 MW_{th} modules. The corresponding thermal-hydraulic parameters and the physical geometry of the modules are shown in Table 2.4 and Table 2.5. For the wavy channel PCHE design the pitch angle, ϕ, was selected to be 15° for the optimal performance. The 15° wavy channel pitch angle gave the best results in terms of increased heat transfer and pressure drop penalty.

Table 2.4. 15° Wavy Channel Thermal-Hydraulic Performance

Parameters	**Hot Channel**	**Cold Channel**	**Hot Channel**	**Cold Channel**
Thermal Duty [MW]	92.07		69.82	
Hydraulic Diameter [mm]	0.922 mm		1.22 mm	
Surface Area [m^2]	2.5319e+03		2.4885e+03	
Reynolds Number	1745.6	1715.6	2326.5	2367.2
Δp **[kPa]**	100.57	85.56	72.59	60.96
Nusselt Number	8.9935	9.0717	10.63	10.73
h **[W/m^2-K]**	3326.1	3294.6	2970.8	2544.9
U **[W/m^2-K]**	1562.5		1205.6	

Table 2.5. 15° Wavy Channel Module Configuration

Parameters	$D_h = 0.922$ mm	$D_h = 1.2$ mm
Number of Plates Per Side	700	550
Channels	900	850
Plate Width [m]	1.225	1.2375
Plate Length [m]	1.0	1.0
Core Height [m]	2.6280	2.4820
Total Volume [m^3]	3.8763	3.6920
Compactness [m^2/m^3]	786.466	810.1931

From the results above, it is seen that the nominal duty of the smaller wavy channel diameter is much larger than the design duty. This is because more plates are required for maintaining the Reynolds number small enough for the flow to be considered laminar. The design equations are not valid at higher Reynolds numbers, which may lead to unreliable design of the heat exchanger. A larger hydraulic diameter is preferable in the modules.

Thermal Hydraulic Design of a Prototype PCHE with Helium

The operating parameters for the HTHF prototype were modified for testing the OSU facility. The maximum pressures were changed to reflect the operating conditions that the HTHF is capable of testing in. These operating parameters are shown in Table 2.6. The model PCHEs to be tested in the HTHF has been scaled according to the mass flow rate of the facility.

Table 2.6. Operating Conditions for the 16 kW Design

Parameters	Hot Channel In	Hot Channel Out	Cold Channel In	Cold Channel Out
Fluid	Helium		Helium	
T [°C]	800	543	520	776
P [MPa]	3	2.95	2	1.95
$\dot{m}$ [kg/s]	0-49		0-49	
ρ [kg/m^3]	3.117	4.059	4.78	3.603
c_p [kJ/kg-K]	5.19	5.19	5.19	5.19
k [W/m-K]	0.3822	0.3164	0.3106	0.3767
μ [kg/m-s]	4.859e-05	4.008e-05	3.929e-05	4.783e-05
Prandtl Number	0.66	0.66	0.66	0.66

The model design thermal duties were 16.6 kW and the designs are shown in Tables 2.7 and 2.8.

Table 2.7. 15° Wavy Channel Thermal-Hydraulic Performance

Parameters	**Hot Channel**	**Cold Channel**	**Hot Channel**	**Cold Channel**
Thermal Duty [kW]	16.6		16.6	
Hydraulic Diameter [mm]	0.922		1.22	
Surface Area [m^2]	0.7475		1.0060	
Reynolds Number	500.07	491.76	371.5598	365.3832
Δp [kPa]	11.001	17.077	3.2798	5.0941
Nusselt Number	5.6792	5.6551	5.4401	5.4208
h [W/m^2-K]	2030.7	2057.9	1468.6	1489.3
U [W/m^2-K]	985.995		714.385	

Table 2.8. 15° Wavy Channel Module Configuration

Parameters	$D_h = 0.922$ mm	$D_h = 1.2$ mm
Number of Plates Per Side	31	38
Channels	20	15
Plate Width [cm]	3.52	3.38
Plate Length [cm]	30	30
Core Height [cm]	9.05	12.26
Total Volume [m^3]	0.0016	0.0040
Compactness [m^2/m^3]	781.9974	810.1931

Thermal Hydraulic Design with Helium (Primary) and Fluoride Salt (Secondary)

The operating conditions are shown in Table 2.9 for the Helium/Fluoride Salt (in this case FLiNaK) primary and secondary loop fluid combination.

Table 2.9. Operating Conditions for the 600 MW_{th} Design

Parameters	Hot Channel In	Hot Channel Out	Cold Channel In	Cold Channel Out
Fluid	Helium		FLiNaK	
T [°C]	800	511	500	757
P [MPa]	7	6.95	0.101	0.100
$\dot{m}$ [kg/s]	400	400	1240	1240
ρ [kg/m^3]	3.117	4.251	2.07e+03	1.96e+03
c_p [kJ/kg-K]	5.19	5.19	1.882	1.882
k [W/m-K]	0.375	0.298	0.951	0.776
μ [kg/m-s]	4.687e-05	3.769e-05	0.0036	0.0017
Prandtl Number	0.66	0.66	5.938	5.938

The straight channel PCHE correlations were used to determine the geometry for a Helium/Fluoride Salt primary and secondary working fluid PCHE. The correlations below were used for the different flow regimes that the potential fluids could experience.

Straight Channel PCHE:

The flow regime for a semicircular duct can be defined as follows: the laminar region $\left(\mathrm{Re} < 2300\right)$, the transitional region $\left(2300 \le \mathrm{Re} \le 10{,}000\right)$, and the turbulent region $\left(\mathrm{Re} \ge 10{,}000\right)$.

Overall Pressure Drop Characteristics

The laminar flow friction factor can be approximated from the correlation recommended by Hesselgreaves (2001),

$$f\,\mathrm{Re} = 15.78 \tag{2.5}$$

The transitional flow friction factor can be approximated from the correlation developed by Techo et al. (1965) that is recommended by Hesselgreaves (2001),

$$\frac{1}{\sqrt{f}} = 1.7372 \ln\left[\frac{\mathrm{Re}}{1.964 \ln \mathrm{Re} - 3.8215}\right] \tag{2.6}$$

Overall Heat Transfer Characteristics

For laminar flow, the Nusselt number can be approximated from the correlation recommended by Hesselgreaves (2001),

$$\mathrm{Nu} = 4.089 \tag{2.7}$$

For the transitional flow region, the Nusselt number can be approximated from the correlation developed by Gnielinski (1983) recommended by Hesselgreaves (2001),

$$\mathrm{Nu} = \frac{(f/2)(\mathrm{Re}-1000)\mathrm{Pr}}{1+12.7(f/2)^{0.5}\left(\mathrm{Pr}^{\frac{2}{3}}-1\right)}\left[1+\left(\frac{d_h}{L}\right)^{\frac{2}{3}}\right] \quad (2.8)$$

This correlation is valid from $\left(2300 < \mathrm{Re} < 5\times10^4\right)$ and $\left(0.5 < \mathrm{Pr} < 2000\right)$.

Thermal Hydraulic Design of a Full Scale PCHE with Helium and Fluoride Salt

For this configuration of a gas and liquid PCHE, a different core configuration is used. This configuration utilizes a double bank geometry that allows the Helium to have the same velocity as the Fluoride Salt. This configuration is shown in Figure 2.4.

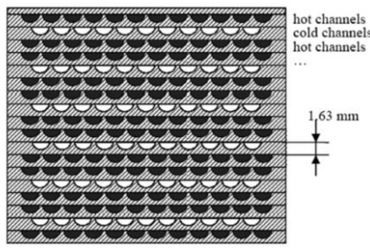

Figure 2.4. Double Bank PCHE Core (Ishizuka et al., 2005)

The full scale PCHE design for Helium (primary fluid) and Fluoride Salt (secondary fluid) is shown in Table 2.10.

Table 2.10. Helium-Fluoride Salt PCHE Design Results

	Straight Channel	
Parameters	Hot	Cold
Duty [MW]	600.67	
ΔT_{LMTD} [°C]	16.28	
A_h [m^2]	3.5675e+04	
Reynolds number	888.3	932.4
ΔP [kPa]	11.4	11.3
Nusselt number	4.089	4.089
h [W/m^2-K]	1522.1	1446.8
U [W/m^2-K]	722.7	
Hot Plate Channel Diameter [mm]	2	
Number of Hot Plates	6630	
Number of Hot Channels	2600	
Cold Plate Channel Diameter [mm]	3.5	
Number of Cold Plates	3315	
Number of Cold Channels	2000	
Core width [m]	7.7500	
Core length [m]	1.000	
Plate thickness [mm]	2	
Compactness [m^2/m^3]	619.2	

2.2 Offset Strip-Fin PCHE

Also of interest is the PCHE with offset strip-fins due to significant research in this geometry by Manglik and Bergels (1995). Offset strip-fins help interrupt the fully developed flow regions and restart the boundary layers, which can significantly increase the heat transfer coefficient. The geometry of the offset strip-fin channel is shown in Figure 2.5 and the values are shown in Table 2.11.

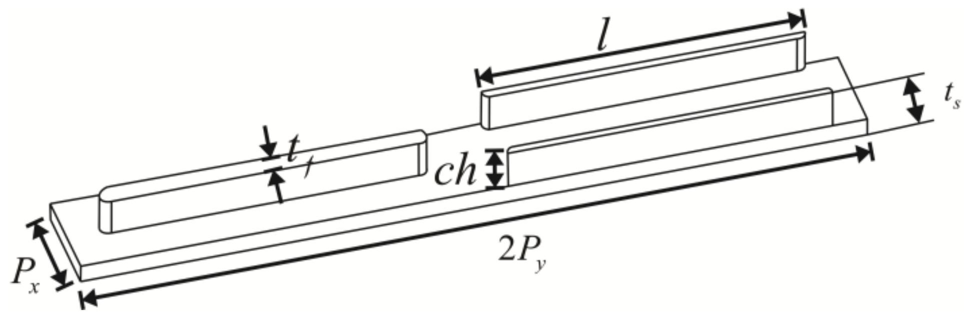

Figure 2.5. One geometry cell of offset strip-fin heat exchanger

Table 2.11. Offset Strip-Fin Geometry

Variable	**Dimension**
Channel height, ch (mm)	1.2
Fin thickness, t_f (mm)	0.6
Fin length, l (mm)	10
Plate thickness, t_s (mm)	1.8
Pitch in flow direction, P_y (mm)	12
Pitch in span-wise direction, P_x (mm)	2

The flow chart used for the design of offset strip-fin PCHE is shown in Figure 2.6 and the details of the design described below. Since the heat transfer coefficient is improved, the heat exchanger volume can be highly reduced as opposed to straight channel heat exchangers.

The correlations listed below developed by Manglik and Bergels (1995) are the most widely used. The results are obtained based on the results and conclusions of works of other researchers such as Kays and London, Joshi and Webb. The equations for the Fanning Friction Factor, f , and the Colburn factor, j , are correlated to the experimental data within $\pm 20\%$ for $120 < \mathrm{Re} < 10^4$ and $0.5 < \mathrm{Pr} < 15$.

$$f = 9.6243\,\mathrm{Re}^{-0.7422}\,\alpha^{-0.1856}\delta^{0.3053}\gamma^{-0.2659}\left(1 + 7.669\times10^{-8}\,\mathrm{Re}^{4.429}\,\alpha^{0.92}\delta^{3.767}\gamma^{0.236}\right)^{0.1} \tag{2.9}$$

$$j = 0.6522\,\mathrm{Re}^{-0.5403}\,\alpha^{-0.1541}\delta^{0.1499}\gamma^{-0.0678}\left(1 + 5.269\times10^{-5}\,\mathrm{Re}^{1.34}\,\alpha^{0.504}\delta^{0.456}\gamma^{-1.055}\right)^{0.1} \tag{2.10}$$

where the following parameters are defined as $\alpha = \left(P_x - t_f\right)/ch$, $\delta = t_f/l$, $\gamma = t_f/\left(P_x - t_f\right)$. The heat transfer coefficient of the exchanger can be found with the Colburn factor shown in Eq. (2.11).

$$j = Co = \mathrm{St}\,\mathrm{Pr}^{2/3} = \frac{\mathrm{Nu}}{\mathrm{Re}\,\mathrm{Pr}^{1/3}} \tag{2.11}$$

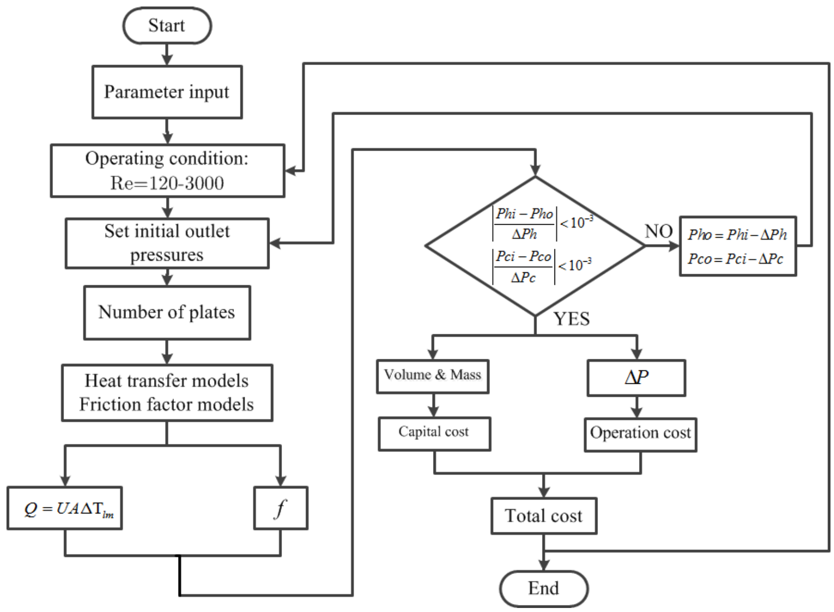

Figure 2.6. Flow Chart for the Offset Strip-Fin Design

The results of the design exercise are presented below.

Full-Scale Design Results Helium-Helium Offset Strip-Fin PCHE

In general, a large IHX consists of many modules, which are made of several blocks. There are some geometric limitations for the block due to the limited capabilities of industry: maximum plate width and non-flow length are 0.6 m and flow length is 1.5 m (Kim and No, 2012). The non-flow length of the module is 3 m when one module consists of five blocks. 65 modules need to be constructed when operating the heat exchanger at the minimal cost condition. Too many modules will certainly increase the capital cost for the entire nuclear plant. Therefore, the prototypic design limits the number of module to 16, increases the flow length and Reynolds number to 1.176 m and 2140, respectively, along with the other parameters are shown in the Table 2.12, are proposed for the offset strip-fin IHX.

Table 2.12. Thermal Hydraulic Design of Offset Strip-Fin Heat Exchanger

Parameter	Unit		Parameter	Unit	
Thermal duty	MW	600	**Hot side pressure drop**	kPa	73.5
Hot side inlet temperature	°C	800	**Cold side pressure drop**	kPa	62.7
Cold side inlet temperature	°C	520	**Hot side Nusselt number**	-	17
Hot side outlet temperature	°C	543	**Cold side Nusselt number**	-	17.1
Cold side outlet temperature	°C	777	**Hot side heat transfer**	W/m^2-K	4398.3
Hot side inlet pressure	MPa	7	**Cold side heat transfer**	W/m^2-K	4361.4
Cold side inlet pressure	MPa	7.97	**Overall heat transfer**	W/m^2-K	1706.8

Hot side Reynolds number	-	2140	**LMTD**	°C	23
Cold side Reynolds number	-	2174	**Total plate number**	-	26669
Hot side mean velocity	m/s	17.8	**Surface area density**	m^2/m^3	892
Cold side mean velocity	m/s	15.3	**Flow length**	m	1.176
Hot side hydraulic diameter	mm	1.3	**Total module number**	-	16
Cold side hydraulic diameter	mm	1.3	**Volume**	m^3	33.9

Prototype Design Results Helium-Helium Offset Strip-Fin PCHE

The volume of prototypic offset strip-fin IHX is more than 30 m^3 for a 600 MW_{th}-Reactor. It is important to know the IHX thermal-hydraulics performance from the test experiment. However, doing experiment with prototype is very expensive and time consuming. In order to get the IHX's thermal-hydraulics performance and verify its abilities for NGNP, a scaling-down approach, which is the method that can reduce the volume of the test heat exchanger with the similar performance as prototype, was adopted in this design.

For this study, the main purpose of scaling down the IHX was to ensure the flow and heat transfer mechanisms of the IHX test model were same as that of prototypical IHX, which means to keep the Reynolds number of the IHX test model similar to that of prototype. The Reynolds number can be obtained from the energy balance equations.

$$\dot{m}\bar{c}_p\Delta T = \dot{Q} \tag{2.12}$$

$$UA\Delta T_{lm} = \dot{Q} \tag{2.13}$$

From Eq. (2.12) and (2.13), the Reynolds number ratio of the test model to prototypic IHX can be expressed as Eq. (2.14).

$$\left(\mathrm{Re}\right)_R = \left(\frac{\rho v d}{\mu}\right)_R = \left(\frac{L\Delta T_{lm}}{\Delta T}\right)_R \tag{2.14}$$

In order to keep the mechanisms of test model are same as the prototypical IHX, the Reynolds number ratio should be approximately equal to one. From Eq. (2.14), only by adjusting ΔT_{lm} and ΔT can the Reynolds numbers for both test model and prototype is kept the same, since the flow length of the test model is much smaller than the length of prototype. It is important to note that densities of fluid for prototypical and test model are very different due to fact that pressure in the exiting experimental facility cannot exceed 3 MPa.

The main purpose of this project is to determine the performance of IHX at high temperature condition, so the hot side inlet temperature was maintained at 800°C for the scaled-down IHX. The flow length was chosen to be about 0.3 m due to the limitation of facility and flexibility for installation. In all, one reasonable test model can be obtained through the method described above. Table 2.13 shows the comparison between test model parameters and prototypical parameters when the Reynolds numbers on the hot sides are the same.

Table 2.13. Scale-Down of Offset Strip-Fin Design

Parameter	Units	Test Model	Prototype	Ratio
Thermal power	kW	21	600,000	3.5E-05
Hot side inlet temperature	°C	800	800	1
Cold side inlet temperature	°C	350	520	0.67
Hot side outlet temperature	°C	476	543	0.88
Cold side outlet temperature	°C	674	777	0.87
LMTD	°C	126	23	5.48
Hot side inlet pressure	MPa	2	7	0.29
Cold side inlet pressure	MPa	2	7.97	0.25
Mass flow rate	kg/h	45	1620000	2.78E-05
Total number of plate	-	17	26669	6.37E-4
Flow length	M	0.288	1.176	0.25
Non-flow length	M	0.032	0.6	0.053
Hot side Reynolds number	-	2140	2140	1
Cold side Reynolds number	-	2363	2174	1.1
Hot side Nusselt number	-	17	17	1
Cold side Nusselt number	-	18	17.1	1.1
Hot side heat transfer coefficient	W/m^2-k	4289	4398.3	0.98
Cold side heat transfer coefficient	W/m^2-K	4078	4361.4	0.94
Overall heat transfer coefficient	W/m^2-K	1585	1706.8	0.93

Capital Cost Investigation

Economic analysis plays an important role in evaluation of one new product. The cost-evaluation method used by Kim and No (2012), recommended for economic analysis of IHXs, is used in this project. The total cost assumes to be the sum of the capital cost and operating cost. In this study, an economic analysis for an offset strip-fin IHX has been performed based on a reference design of the 600 MW_{th} Very High Temperature Reactor (Kim et al., 2008).

Capital Cost

The capital cost of an IHX can be estimated based on the volume or weight of the heat exchanger. In this study, Alloy 617 was selected as the IHX material. The price of a heat exchanger is normally quoted in price/kg because this unit is independent of thermal conditions. For nuclear applications, the price of Alloy 617 was 120 US $/kg (Kim et al., 2008). Since the additional mass due to the headers is negligibly small and was neglected, the capital cost can be obtained by multiplying the material cost C_m and the IHX core volume V by the metal density ρ as:

$$C_c = C_m \rho V \tag{2.15}$$

Capital cost is a one-time expense incurred on the purchase of equipment. Since the unit of the capital cost ($) is different from that of the operating cost ($/y), it is necessary to convert the unit of capital cost ($) to that of operating cost ($/y) by taking into account bank interest rate and IHX lifetime. If a loan from a bank with interest *r* and after *n* years, the total payment C_{ct} is:

$$C_{ct} = C_c (1+r)^n \tag{2.16}$$

Assume a constant payback is made to the bank then the payment C_{cp} for every year can be calculated as:

$$C_{ct} = \sum_{i=1}^{i=n} C_{cp}(1+r)^{i-1} = \frac{C_{cp}}{r}\left[(1+r)^n - 1\right] \tag{2.17}$$

Operating Cost

Operating cost for IHXs is proportional to the pumping power, which can be determined by the pressure drop across the IHX:

$$P_{\text{pump}} = \frac{\dot{m}\Delta p}{\rho\eta} \tag{2.18}$$

where η is the pump efficiency, in general, $\eta = 0.80 - 0.85$, $\dot{m}$ is the mass flow rate. The electricity cost C_e can be obtained from the U.S. Energy Information Administration for the industrial sector. So the operating cost C_o can be assessed as:

$$C_o = C_e P_{\text{pump}} \tag{2.19}$$

Total Cost

As described above, the total cost of IHX is the summation of the capital cost and operating cost. The reference-operating period for IHXs is assumed to be 20 years, and the interest rate of a bank is assumed to be 5% (Kim and No, 2012). Then the total cost can be obtained from:

$$C_t = C_{cp} + C_o \tag{2.20}$$

Effects of Geometric Parameters of Offset Strip-Fin PCHEs

To get reasonable geometric parameters of offset strip-fin IHXs, geometric parameters evaluations were performed based on the economic analysis described above. Five geometry parameters were evaluated, namely, pitch in span-wise direction, pitch in flow direction, fin height, fin length, and fin thickness. In the first calculation, five geometric parameters were selected from Losier et al. (2007), which were evaluated by the CFD calculations. Table 2.13 lists the geometric parameters for both prototypic design and test model design which were obtained by iterating the cost-evaluation process with only one parameter changing per iteration.

The relationship between the total cost and Reynolds number is shown in Figure 2.7(a). When the Reynolds number equal to 532, the total cost reaches the minimum and the heat exchanger volume is about 58.5 m^3. The total costs of heat exchanger versus of geometric parameters under the minimal cost condition are given in Figure 2.7(b)-(f). As can be seen in these figures, the total cost will decrease only when the fin length increasing. While increasing other factors, the total cost will increase. This is because increasing the fin length, the volume of IHX will decrease greatly due to the increasing overall heat transfer coefficient and heat exchanger compactness. At this time, decreasing capital cost is the primary factor in the total cost and results in total cost reduction. As shown in Figure 2.7(b)-(d), increasing fin height, pitch in span-wise direction, and pitch in flow direction, will decrease the overall heat transfer coefficient and area density, which will increase the volume of IHX, resulting in increasing the capital cost significantly. Therefore, the total costs will increase though the operating cost decreasing. However, increasing the fin thickness, the capital cost will decrease because of the increased overall heat transfer coefficient and heat exchanger compactness lead to decreasing the volume. While at this time, the operating costs will increase significantly and play a primary role in the total cost. As presented in Figure 2.7(f), the total cost increases with the increasing fin thickness.

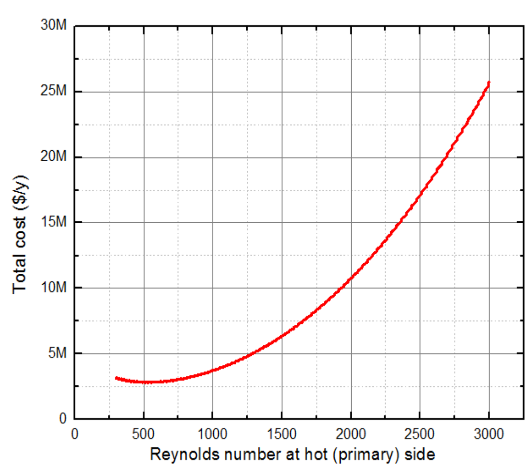

(a)

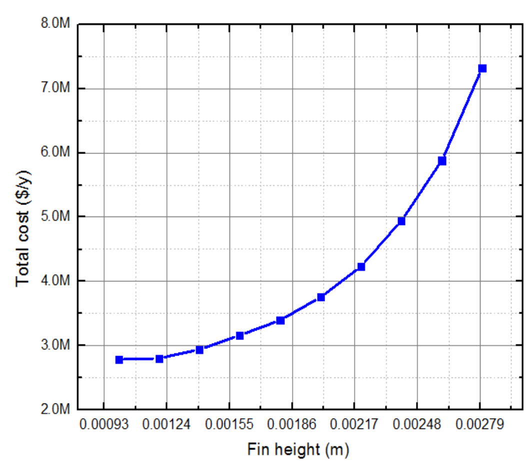

(b)

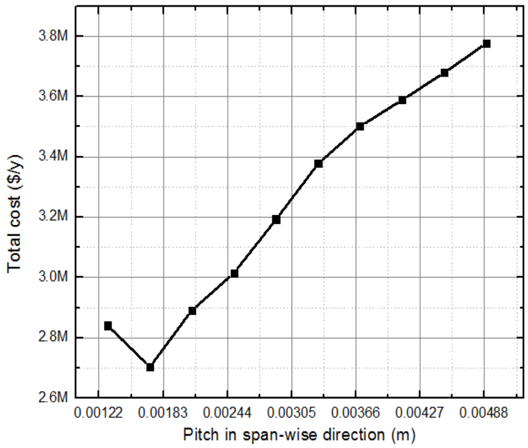

(c)

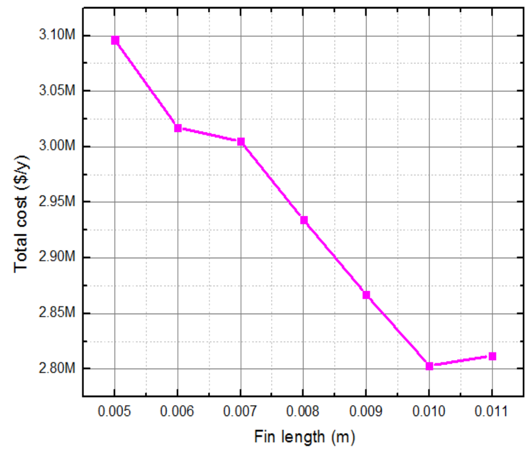

(d)

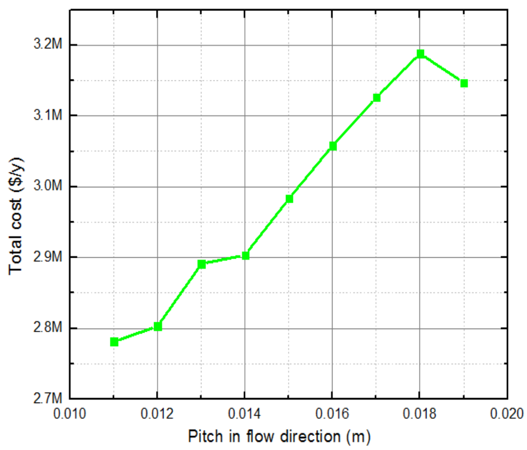

(e)

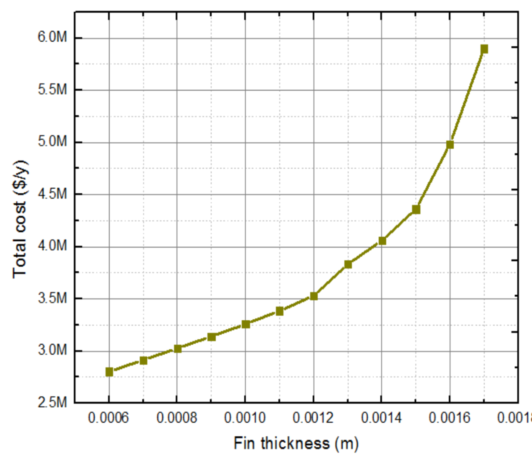

(f)

Figure 2.7. Factors that affect the total cost of the offset strip-fin heat exchanger: (a) Reynolds number, (b) Pitch in span-wise direction, (c) Pitch in flow direction, (d) Fin height, (e) Fin length, and (f) Fin thickness

2.3 Helical Coil Heat Exchanger

The Helical Coil Heat Exchanger (HCHE) offers several advantages over the conventional shell-and-tube heat exchangers in a variety of situations. The design of HCHEs offers a more compact heat transfer medium and can operate efficiently in the laminar and transitional flow regime. The curved shape of the tube causes the flowing fluid to striate and allows the outer fluid particles to have higher velocities than those flowing near the pipe wall. This results in secondary flows (or vortices) that produce additional convective transport through the helical coils. The effect of coil curvature also suppresses turbulent fluctuations arising in the flowing fluid and the emergence of turbulence. This increases the Reynolds number required to attain a fully turbulent flow (Jayakumar, 2012).

One of the most interesting phenomena associated with fluid flowing in a helical tube is that the laminar-to-turbulent transition region is a function of the curvature ratio. The curvature ratio is defined as the tube radius divided by the radius curvature and influences the critical Reynolds number at which point the laminar flow regime begins its transitions to the turbulent flow regime. Figure 2.8 shows the influence of curvature ratio on the critical Reynolds number for HCHEs.

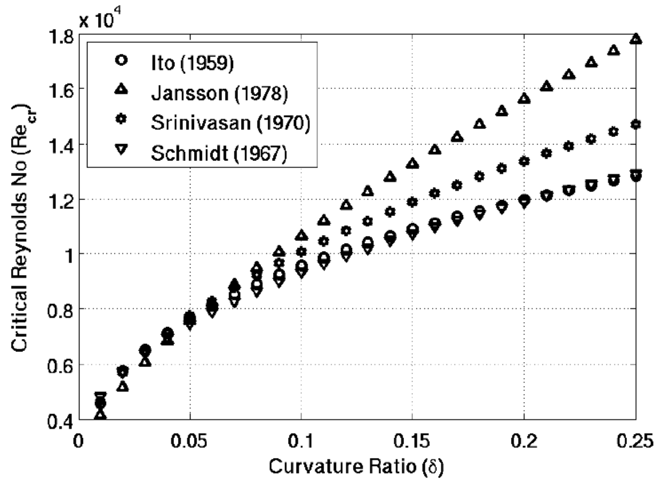

Figure 2.8. Critical Reynolds number as a function of Curvature Ratio (Jayakumar, 2012)

Figure 2.9 shows one such HCHE design for an IHX for the very high/high temperature reactor. Figure 2.10 shows an interior view of the HCHE and tube bundle orientation. The inner annulus of the exchanger allows the primary fluid to flow and gives a better temperature control for transient situations.

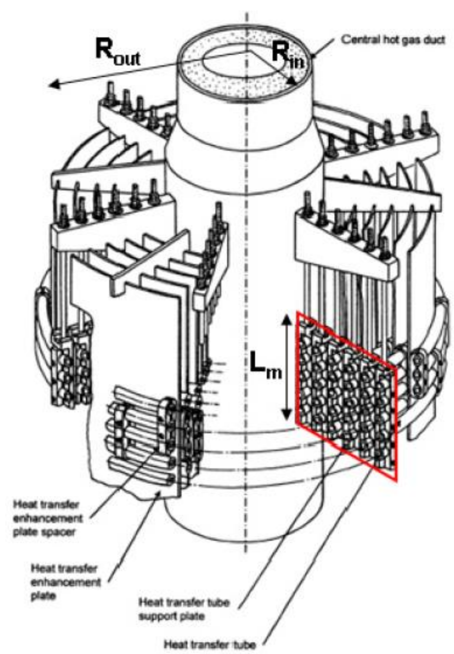

Figure 2.9. Diagram of HCHE bundle (Kato et al. 2007)

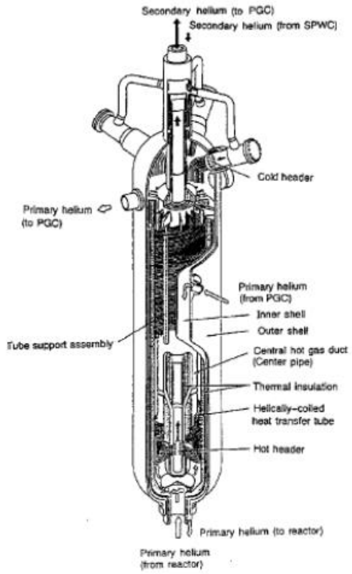

Figure 2.10. Schematic of HCHE (Kato et al. 2007)

Figure 2.11 shows the helical coil geometry.

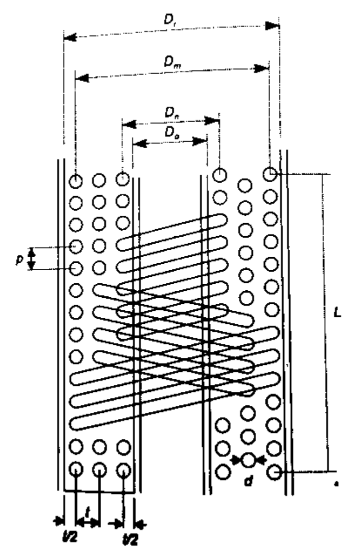

Fig.5.1 Helical tube bundle with start factor r = 1

Figure 2.11. Helical Coil Geometry (Smith, 2005).

HCHE Model Development

The number of required tubes, N_t, for the bundle can be found from the equation,

$$N_t = \frac{(R_{out} - R_{in})}{p} \frac{L_m}{p} \quad (2.21)$$

where R_{out} and R_{in} are the outer and inner radius of the shell, L_m is the height of the tube bundle and p is the tube pitch. The length of the inner, outer and middle layer of tubes can be found from the equation,

$$L_{t,in} = 2\pi R_{in} N_b \quad (2.22)$$

$$L_{t,out} = 2\pi R_{out} N_b \quad (2.23)$$

$$L_{t,mid} = 2\pi (R_{in} + R_{out}) N_b \quad (2.24)$$

where N_b is the total number of tube rotations of the tube bundle.

The length of the shell, L_s, can be calculated from the number of rotations of the tube bundle and the height of the tube bundle.

$$L_s = L_m \cdot N_b \quad (2.25)$$

The outer area heat transfer surface area of the tube bundle can be approximated from the equation,

$$A_s = \pi \cdot D_{t,out} \cdot L_{t,mid} \cdot N_t \quad (2.26)$$

Thermal-Hydraulic Characteristics

The total heat transfer of the heat exchanger can be calculated from the equation,

$$Q = U \cdot A_s \cdot \Delta T_{LMTD} \quad (2.27)$$

where U is the overall heat transfer coefficient and ΔT_{LMTD} is the log mean temperature difference of the heat exchanger.

$$U = \left[\frac{1}{h_s} + R_w + \frac{1}{h_t}\right]^{-1} \quad (2.28)$$

Where $h_s$is the shell-side convective heat transfer coefficient, R_w is the thermal resistance of the pipe wall, and h_t is the tube-side convective heat transfer coefficient.

The log mean temperature difference, ΔT_{LMTD}, of the fluid in counterflow is defined as,

$$\Delta T_{LMTD} = \frac{\left(T_{h,1} - T_{c,1}\right) - \left(T_{h,2} - T_{c,2}\right)}{\ln\left(\frac{(T_{h,1} - T_{c,1})}{(T_{h,2} - T_{c,2})}\right)} \quad (2.29)$$

The counterflow fluid orientation for the HCHE is chosen because it utilizes a larger temperature difference and results in a closer temperature approach and higher temperature effectiveness than heat exchangers in concurrent flow.

Shell-side Correlations:

The fluid flowing in the shell is primarily in cross flow. The in-line bundle orientation is shown below in Figure 2.12. The correlations for the Nusselt number, Nu_b, were developed by Zukauskas et al. (1987) for the following Reynolds number ranges:

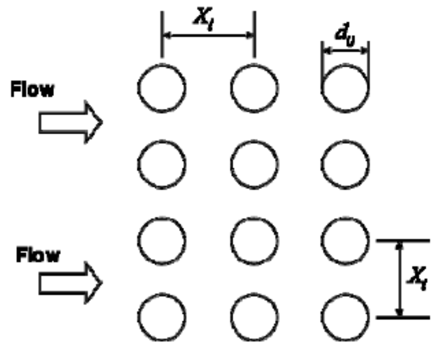

Figure 2.12. Tube Bundle Arrangement (Zukauskas et al., 1987)

$$Nu_b = 0.9 \cdot c_n \cdot {Re_b}^{0.4} \cdot Pr^{0.36} \cdot \left(\frac{Pr_b}{Pr_w}\right)^{0.25} \quad (Re_b = 1 - 10^2) \qquad (2.30)$$

$$Nu_b = 0.52 \cdot c_n \cdot {Re_b}^{0.4} \cdot Pr^{0.36} \cdot \left(\frac{Pr_b}{Pr_w}\right)^{0.25} \quad (Re_b = 10^2 - 10^3) \qquad (2.31)$$

$$Nu_b = 0.27 \cdot c_n \cdot {Re_b}^{0.62} \cdot Pr^{0.36} \cdot \left(\frac{Pr_b}{Pr_w}\right)^{0.25} \quad (Re_b = 10^3 - 2 \cdot 10^5) \qquad (2.32)$$

$$Nu_b = 0.033 \cdot c_n \cdot {Re_b}^{0.8} \cdot Pr^{0.36} \cdot \left(\frac{Pr_b}{Pr_w}\right)^{0.25} \quad (Re_b = 2 \cdot 10^5 - 2 \cdot 10^6) \quad 2.33)$$

The coefficient, c_n, is a correction factor for the number of tube rows which approaches 1 only when $n > 16$. $Re_{shell,b}$ is the shell-side bulk fluid Reynolds number and Pr the fluid and wall Prandtl number. The Reynolds number is defined below.

$$Re_b = \frac{V_{shell,max} D_{t,out} \rho}{\mu} \qquad (2.34)$$

$V_{shell,max}$ is the maximum average velocity of the fluid flowing through the shell, $D_{t,out}$ is the outer diameter of the tubes in the tube bundle, ρ is the fluid density, and μ is the dynamic viscosity of the fluid.

The shell-side pressure drop for the fluid flowing across the tube bundles in cross flow was defined by Kakac & Liu (2002). This pressure drop correlation was developed for the multirow bundle and is given below.

$$\Delta P_{shell} = \left(\frac{Eu}{\chi}\right) \cdot \chi \cdot \frac{1}{2} \cdot \rho \cdot V_{shell,max}{}^{2} \cdot n \qquad (2.35)$$

Eu is defined as the fluid Euler number, χ is a correction factor, and n is the number of tube rows counted in the flow direction.

Tube-side Correlations:

Schmidt's correlation for the Nusselt number correlation of a helical tube in turbulent flow can be described from the relationship to the Nusselt number of a straight tube at the same Reynolds number.

$$\frac{Nu_t}{Nu_s} = 1.0 + 3.6\left[1 - \left(\frac{a}{R}\right)\right]\left(\frac{a}{R}\right)^{0.8} \qquad (2.36)$$

In the above equation, a, is the radius of the helical tube and R is the radius of the curvature for the helical tube. The straight tube Nusselt number can be calculated from the Dittus-Boelter correlation

$$Nu_s = 0.022 \cdot Re_{tube,b}{}^{0.8} Pr_{tube,b}{}^{0.5} \qquad (2.37)$$

The tube-side pressure drop correlation in tube bundles in crossflow based on experimental results is given by Kakac & Liu (2002):

$$\Delta P_{tube} = 4f \cdot \frac{L}{D_{tube,i}} \cdot \rho \cdot \frac{V_{tubes,m}{}^{2}}{2} \qquad (2.38)$$

In the above equation, f is the friction factor, L is the mean tube length, $D_{tube,i}$ is the tube inner diameter, and $V_{tube,m}$ is the mean flow velocity in the tube. The mean flow velocity of the tubes is given by the equation

$$V_{tubes,m} = \frac{\dot{m}_{tubes}}{\rho \cdot \left(\pi D_{shell,i}{}^{2}\right) \cdot N_t} \qquad (2.39)$$

The tube mass flow rate is $\dot{m}_{tubes}$.

The friction factor for a helical coil in turbulent flow was based off experimental work done by Srinivasan (1993) defined for the conditions $Re\left(\frac{R}{a}\right)^{-2} < 700$ and $7 < \frac{R}{a} < 104$.

$$f \cdot \left(\frac{R}{a}\right)^{0.5} = 0.0084 \cdot \left[Re\left(\frac{R}{a}\right)^{2}\right]^{-0.2} \qquad (2.40)$$

The full-scale design results for the helium-helium and helium-fluoride salt combinations are shown in Tables 2.14 and 2.15, respectively.

Table 2.14. Helium-Helium Helical Coil Heat Exchanger Full-Scale Design Results

Parameters	HCHE Tubes	HCHE Shell
Duty [MW]	600	
ΔT_{LMTD} [°C]	75.85	
A_h [m^2]	8.0734e+03	
Reynolds number	4.6e+04	7.16e+04
ΔP [kPa]	94.51	66.86
Nusselt number	148.4	97.8
h [W/m^2-K]	2813.4	1728.7
U [W/m^2-K]	987.79	
Number of Tubes	6900	
Number of Tubes in radial direction	69	
Rows of tubes	100	
Length of Shell [m]	6.990	
Outer Diameter of Shell [m]	4.6	
Inner Diameter of Shell [m]	0.49	
Outer Diameter of Tubes [mm]	20	
Inner Diameter of Tubes [mm]	18	

Table 2.15. Helium-Fluoride Salt Helical Coil Heat Exchanger Full-Scale Design Results

Parameters	HCHE Tubes	HCHE Shell
Duty [MW]	609.54	
ΔT_{LMTD} [°C]	45.09	
A_h [m^2]	9.6881e+03	
Reynolds number	8.46e+04	4.036e+03
ΔP [kPa]	127.42	7.15
Nusselt number	169.48	62.75
h [W/m^2-K]	3212.9	3059.0
U [W/m^2-K]	1395.5	
Number of Tubes	8280	
Number of Tubes in radial direction	69	
Rows of tubes	120	
Length of Shell [m]	8.388	
Outer Diameter of Shell [m]	4.6	
Inner Diameter of Shell [m]	0.49	
Outer Diameter of Tubes [mm]	20	
Inner Diameter of Tubes [mm]	18	

2.4 Twisted Tube Heat Exchanger (TTHE)

The Advanced High-Temperature Reactor (AHTR) core consists of coated particle fuel embedded in graphite fuel elements and the heat is removed by liquid fluoride salt coolant (Holcomb et al., 2009). The power generation and process heat applications of AHTR are dependent upon an effective IHX, which transfers heat from the primary loop to the secondary loop. A Twisted Tube Heat Exchanger (TTHE) is proposed as an Intermediate Heat Exchanger in the current design of the AHTR system shown below in Figure 2.13.

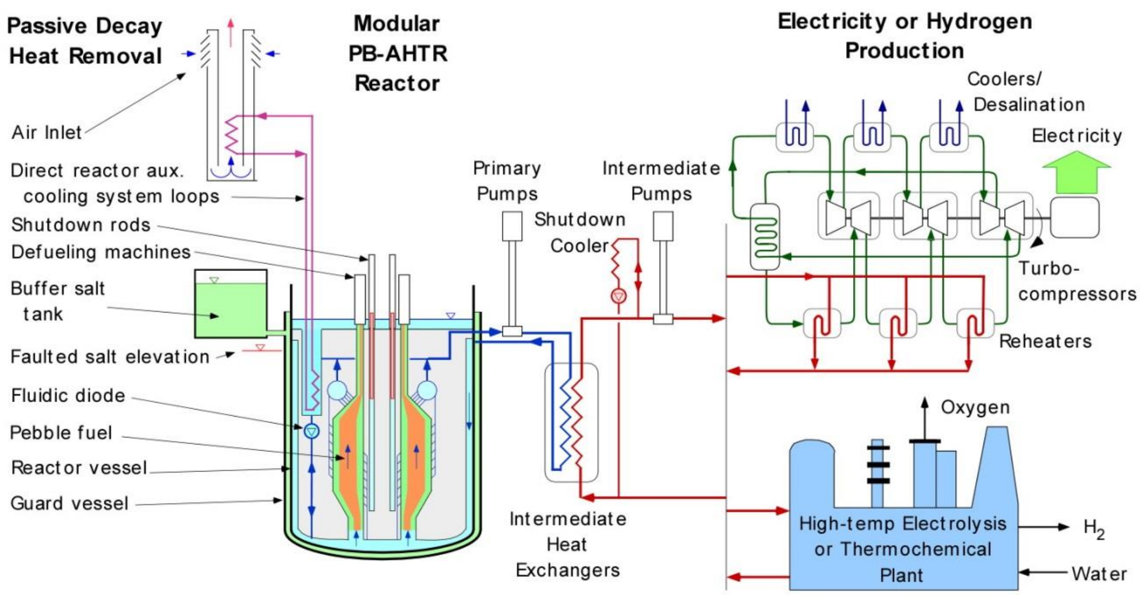

Figure 2.13. Schematic drawing of the modular PB-AHTR

As for the selection of salts, Williams et al. (2006) suggested that FLiBe (^7LiF-BeF_2, 66-34 in mol%) enriched with more than 99.995% ^7Li (which provides a large moderating ratio and small coolant parasitic capture probability) was selected as the primary coolant. FLiNaK (LiF-NaF-KF, 46.5-11.5-42 in mol%) was chosen as the secondary salt due to its good heat transfer capability, low melting point, and low cost. Table 2.16 summarizes the operating conditions for the TTHE based on this fluoride salt combination.

Table 2.16. Operating Conditions for the 225 MW FLiBe-FLiNaK Design

	Hot Channel		Cold Channel	
Parameters	In	Out	In	Out
Nominal Duty [MW]	225.00			
Fluid	FLiBe		FLiNaK	
T [°C]	704	600	545	690
$\dot{m}$ [kg/s]	905.87		823.6	
ρ [kg/m^3]	1936	1987	2132	2026
c_p [kJ/kg-K]	2.39	2.39	1.88	1.88
μ [10^3 kg/m-s]	5.4	8.6	6.5	3.0
Prandtl Number	11.55	19.14	18.49	7.91

Twisted Tube IHX Thermal Hydraulic Design

The heat transfer and pressure drop characteristics of twisted tube were comprehensively studied by Garimella and Christensen (1995) at Ohio State University. The detailed description of twisted tube was presented in the studies by Garimella and Christensen (1995) and also in the dissertation by Garimella (1990). The design of the twisted tube IHX (tube bundle shown in Figure 2.14) is based on the design procedure described by Garimella and Christensen (1995), which briefly presented below.

Figure 2.14. Twisted Tube Bundle insert for Shell-and-Twisted Tube Heat Exchanger [Koch, 2013]

<u>Tube Side:</u>
As for the pressure drop calculations at tube side, the friction factor can be calculated by:

$$f = \frac{64}{Re - 45.0}\left(0.554e^{*0.384}p^{*(-1.454+2.083e^{*})}\theta^{*-2.426}\right) \quad (100 \leq Re \leq 1500) \quad (2.41)$$

$$f = 1.209Re^{-0.261}\left(e^{*(1.26-0.05p^{*})}p^{*(-1.660+2.033e^{*})}\theta^{*(-2.699+3.67e^{*})}\right) \quad (Re \geq 3000) \quad (2.42)$$

These two equations are only valid for:

$$0.11 \leq e^{*} \leq 0.42; 0.41 \leq p^{*} \leq 7.29; 0.28 \leq \theta^{*}0.65$$

As for the heat transfer calculations at tube side, the Nusselt number can be calculated by:

$$Nu = 0.014Re^{0.842}(e^{*-0.067}p^{*-0.293}\theta^{*-0.705}Pr^{0.4}) \quad (500 \leq Re \leq 5000) \quad (2.43)$$

$$Nu = 0.064Re^{0.773}(e^{*-0.242}p^{*-0.108}\theta^{*-0.599}Pr^{0.4}) \quad (5000 \leq Re \leq 80000) \quad (2.44)$$

These two equations are only valid for:

$$0.11 \leq e^{*} \leq 0.42; 0.41 \leq p^{*} \leq 7.29; 0.28 \leq \theta^{*}0.65; 2.5 \leq Pr \leq 7.0$$

Shell Side:

As for the pressure drop calculations at shell side, the friction factor can be calculated by:

$$f = \frac{96r^{*0.035}}{Re}\left(1 + 101.7Re^{0.52}e^{*(1.65+2.0\theta^{*})}r^{*5.77}\theta^{*-2.426}\right) \quad (Re \leq 800) \quad (2.45)$$

$$f = 4\left[1.7372ln\left(\frac{Re}{1.964ln(Re) - 3.8215}\right)\right]^{-2}(1 + 0.0925r^{*})e_f \quad (800 \leq Re \geq 40000) \quad (2.46)$$

where, $e_f = 1 + 222Re^{0.09}e^{*2.40}p^{*-0.49}\theta^{*-0.38}r^{*2.22}$

These two equations are only valid for:

$$0.124 \leq e^{*} \leq 0.309; 0.358 \leq p^{*} \leq 1.302; 0.431 \leq \theta^{*} \leq 0.671; 0.388 \leq r^{*} \leq 0.688$$

As for the heat transfer calculations at shell side, the Nusselt number can be calculated by:

$$Nu = \left[\frac{(f/8)RePr}{1 + 9.77(Pr^{2/3} - 1)\sqrt{f/8}}\right]Re^{-0.20}e^{*-0.32}p^{*-0.28}r^{*-1.64} \quad (800 \leq Re \leq 40000) \quad (2.47)$$

These two equations are only valid for:

$$0.104 \leq e^{*} \leq 0.384; 0.383 \leq p^{*} \leq 6.714; 0.279 \leq \theta^{*} \leq 0.652; 0.216 \leq r^{*} \leq 0.604$$

where, the terms Re, Nu, Pr, and f have their usual meaning, and the other parameters are defined below:

$$e^{*} = \frac{e}{D_{vi}};\ p^{*} = \frac{p}{D_{vi}};\ \theta^{*} = \frac{\theta}{90};\ r^{*} = \frac{D_{vo}}{D_{vi}} \qquad (2.48)$$

$D_b = bore\ diameter;\ D_e = envelope\ diameter;\ D_v = volume - based\ diameter; e = fluted\ depth; p = fluted\ pitch;\ \theta = flute\ helix\ angle.$

The geometry of the Twisted Tube Heat Exchanger is shown below in Table 2.17.

Table 6. Twisted Tube Geometry

Parameters	Value
Inner bore diameter [mm]	9.3
Outside envelope diameter [mm]	16.2
Wall thickness [mm]	1
Fluted pitch [mm]	6.6
Number of fluted starts	4
Sum of Trough Length [mm]	18.4
Nominal IHX diameter [m]	1.448

The TTHE design is shown below in Table 2.18.

Table 2.18. Twisted Tube Design Full-Scale Design Results

Parameters	Twisted-Tube Tubes	Twisted-Tube Shell
Duty [MW]	225.00	
ΔT_{LMTD} [°C]	30	
A_h [m^2]		
Reynolds number	2458	3106
ΔP [kPa]	75.1	116.3
Nusselt number	52.6	128.9
h [W/m^2-K]	5566	7227
U [W/m^2-K]	2791	
Tube Length [m]	11.2	
Total Number of Twisted Tubes	6768	
Hydraulic Diameter of Twisted Tube [m]	0.0103	
Hydraulic Diameter of Shell [m]	0.0157	

From the preliminary results, the shell side diameter is selected to be 1.448 m, the tube length is about 11.2 m. Pressure drops at both primary and secondary sides are 75.1 and 116.3 kPa, respectively.

2.5 Summary

Several heat exchangers alternatives are available for consideration as the intermediate heat exchanger in the advanced reactor-IHX-process heat/power generation system. Steady state designs of four of these candidate IHXs were developed and have been presented above.

3. Modeling of Advanced Reactor-IHX System Transients

The heat transfer system coupled to the advanced nuclear reactor should operate at high efficiency, and be robust enough to deal with any departures from the normal design conditions arising from either the fluctuating power demand, variations in process demand or any other off-normal condition. An effective control system is needed to maintain the system operation at the desired design conditions, and this necessitates understanding the dynamic behavior of the system in response to system perturbances such as variations in flow rates or fluid temperatures (Guomin et al, 2011). Several investigators have studied the transient behavior of heat exchanger in recent years (Al-Dawery et al., 2012, Silaipillayarputhur et al., 2011). However, investigations focusing upon the transient analysis of systems containing more than one heat exchanger as well as other compononents (nuclear reactor, for example) are not common. Further, as the system involves interacting loops, the dynamic behavior of the entire system exhibits a much higher level of complexity than a single heat exchanger system. Modeling and simulation of the dynamic behavior of such a system becomes a challenging task. User-developed computer codes can reach a high level of complexity, and the computational effort can increase significantly. At the same time, several commercial process simulation software packages are available for steady state and dynamic simulation of highly complex processes, and are routinely used in the chemical industry. These softwares have the potential to decrease significantly the modeling/simulation effort and times for the complex interacting systems. Results from the use of one such software are described in this report. One of the limitations of such softwares is the non-availability of a nuclear reactor as a process unit. The report desribes an innovative technique to simulate a nuclear reactor using a chemical reactor. A user-developed code using any of the programming languages does not suffer from such limitation (inability to simulate a nuclear reactor completely, including reactor neutronics), and hence the transient behavior was also simulated using user developed codes.

Section 3.1 describes the application of process simulation softwares to the system and the system response to temperature and flow disturbances. A novel technique for simulating the thermal response of a nuclear reactor is also presented. Section 3.2 describes the development of user-developed MATLAB codes for simulating the steady state and transient behaviors of straight-channel and zig-zag channel PCHEs. The results obtained using the user-developed code were verified by comparison with those obtained using the process simulation software.

3.1 System Analysis with Simulation Software.

Transient behavior of the reactor-intermediate heat exchanger-process application system was simulated using commercially available process simulation softwares PRO/II and Dynsim (Schneider Electric, Invensys Software, Lake Forest, CA). The basic technique involves developing a steady state system model using PRO/II, and exporting the steady state model to Dynsim, for the analysis of the dynamic behavior of the system.

3.1.1 PRO/II Model

A Steady-State Model of the system was created in PRO/II 9.2. Figure 3.1 shows the process flow diagram consisting of a primary loop carrying the heat from the reactor, the secondary loop which receives the thermal energy from the primary loop in the intermediate heat exchanger, and the process loop that receives the thermal energy from the secondary loop via the secondary heat exchanger. The significant components in the system are as follows:

E1- This heat exchanger is used to model the effects of the nuclear reactor. All heat exchangers were modeled for a 10MW design. This heat exchanger had a constant duty of 10MW.

E2: This is the IHX. Tube dimensions were taken from previous data for fluted tube. A heat transfer area of 601.9 m^2. The overall heat transfer coefficient used was 775 W/(m^2*K).

E3: This is the SHX for the system. The heat transfer properties for an offset strip-fin heat exchanger was used. The heat transfer area used was 212.6 m^2. The overall heat transfer coefficient used was 2181 W/(m^2*K).

E4: This heat exchanger was used to cool down helium to original inlet temperature in process loop. A constant overall duty of 10MW was also used for the heat exchanger.

P(1-3): These are the pumps for each loop. They have a pressure rise across them equal to all of the pressure drops across the heat exchangers in any given loop.

SP(1-3) and M(1-3): The SP and M units are splitter and mixers, respectively. These have no functionality in PRO/II but are essential for the simulations by Dynsim.

Initially, helium was used as the heat transfer medium in all three loops to obtain dynamic behavior for various disturbances in different loops. Similar simulations were subsequently also conducted with both FLiNaK and FLiBe. The values of temperatures and flow rates for various streams are shown in Table 3.1 for a system having a nominal duty of 10 MW.

Table 3.2 shows the steady state design values for various components.

Table 3.2: Initial Steady State Conditions

		IHX		**SHX**	
	Units	**cold**	**hot**	**cold**	**hot**
Tin	**K**	798.2	1074.6	779.5	1052.8
Tout	**K**	1051.3	821.5	1034.1	798.2
ΔT	**K**	253.1	253.1	254.6	254.6
Pin	**kPa**	6985.7	6999.5	6994.4	6999.5
Pout	**kPa**	6979.1	6996.9	6976	6985.7
ΔP	**kPa**	6.6	2.6	18.4	13.8
m_dot	**kg/s**	7.499	7.499	7.499	7.499
ΔP_pump	**kPa**	21.5	13.2	24.6	21.5
RPM	**RPM**	3609	3602	3615	3609
Q	**kW**	9860		9920	
LMTD	**K**	23.3		18.7	
U	**kW/(m^2*K)**	0.707		2.296	

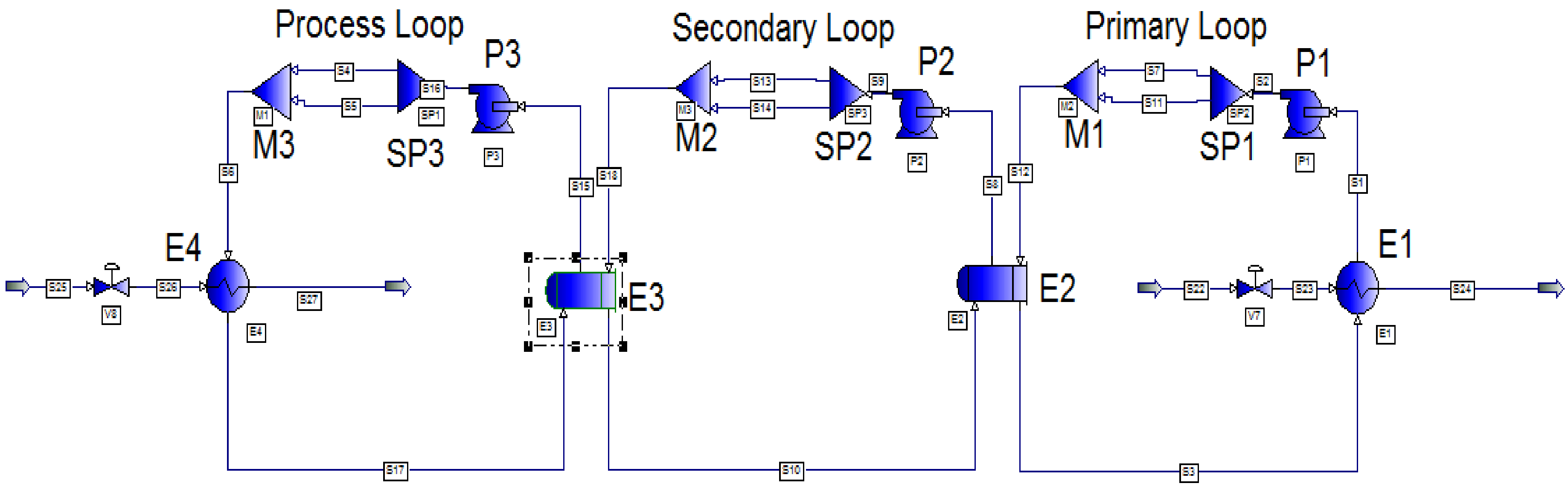

Figure 3.1: Pro/II process flow diagram.

Table 3.1: Stream Properties – Helium Loop

E1	Reactor	Steam(52.5 kg/s) (1080K-1000K)	Helium (819.9K-1073.4K)	Hot side Cold side	**P1**	Primary	Helium (7.499 kg/s)	ΔP=13.2 kPa
E2	IHX	Helium (1073.4K-819.9K)	Helium (796.3K-1049.7K)	Tube side Shell side	**P2**	Secondary	Helium (7.499 kg/s)	ΔP=21.5 kPa
E3	SHX	Helium (1049.7K-796.3K)	Helium (777.4K-1030.9K)	Hot side Cold side	**P3**	Process	Helium (7.499 kg/s)	ΔP= 24.6 kPa
E4	Process	Helium (1030.9K-777.4K)	Steam(35 kg/s) (600K-700K)	Hot side Cold side				

3.1.2 Dynsim Flowsheet and Modeling

The PRO/II flowsheet was then exported to Dynsim for dynamic simulation. The resulting flowsheet is shown in Figure 3.2. The translation to Dynsim results in the addition of several components to the flow sheet:

SS(1-2): These are the new elements called stream sets, that serve to specify the mass flow rate in each loop. These are added for E1 and E2 only. The other streams flow rates are determined by pump head.

Tl_SRC(1-4): These are automatically added into Dynsim when imported from Pro II. They are called sources and are only used to specify inlet conditions such as temperature, pressure, and molar composition.

XV(1-3): These valves were added into the system for controlling flow. A small pressure drop occurs across these.

The overall heat transfer coefficient on flow rates was specified according the following equation:

$$U = U_o * F^n \tag{3.1}$$

Where U is the new heat transfer coefficient, U_o is the heat transfer coefficient at reference flow, F is the ratio of flow rates and n is the exponent for the heat transfer coefficient and determines how it changes with flow rate. The values of the exponent for various streams are as shown in Table 3.3.

Table 3.3: Exponent Values for Heat Transfer Coefficients

	Tube Side	**Shell Side**
IHX	0.842	0.8
SHX	0.5937	0.5937

These values were based on the design equations for the respective heat exchangers.

The flow rate variation was simulated in the Dynsim flowsheet by varying the pump RPM. A pump malfunction could cause the RPMs to increase or decrease causing a sudden change in flow rate. The RPMs were varied to introduce step changes in the flow rates. The system responds to these step changes to reach a new steady state. The results of these step changes ranging from -30% to +30% change from the reference conditions are presented below.

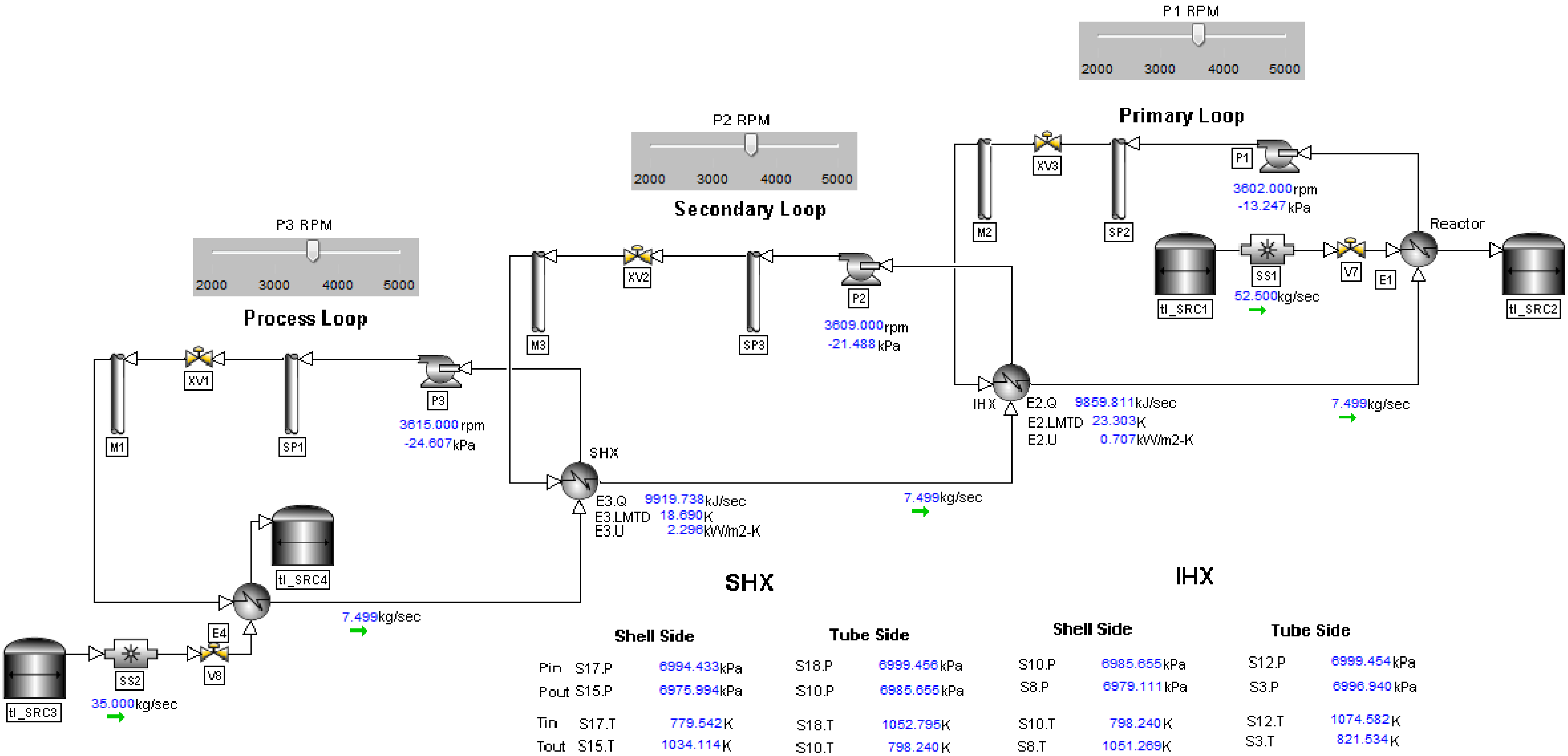

Figure 3.2: Process flow diagram of all helium process in Dynsim.

3.1.3 Simulation of System Behavior for Flow Rate Disturbances

Several different attributes were looked at after each step change. These include overall heat transfer coefficient, log mean temperature difference, heat duty, temperature change, and the pressure drop. It was found that a new steady state was reached for each stimulus (step change). Figure 3.3 shows the changes in the temperatures of various streams in response to the change in the flow rate of secondary stream for molten salt loop. Figure 3.4 show similar results for the helium loop.

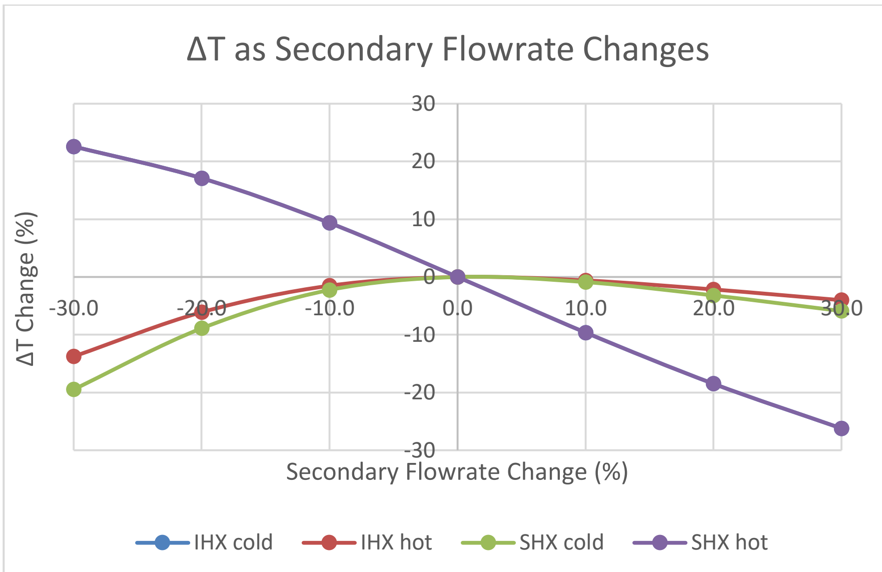

Figure 3.3: Change in temperature difference with changes in secondary loop. (Molten Salt)

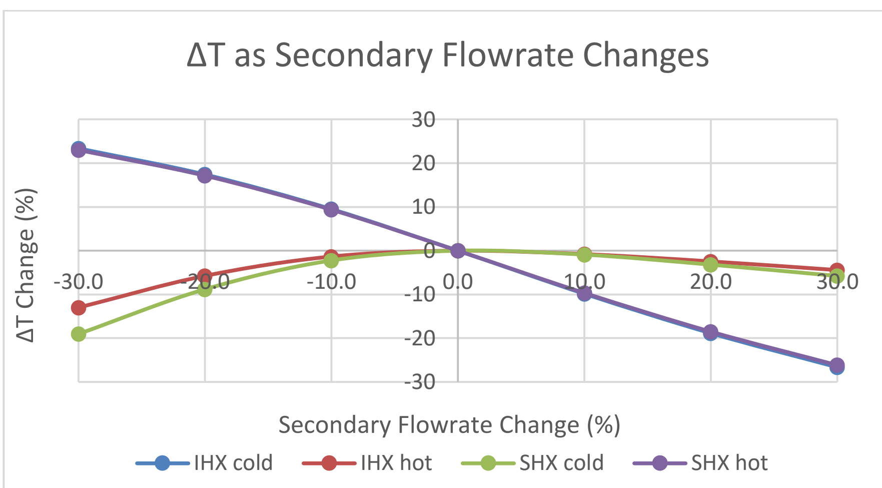

Figure 3.4: Change in temperature difference with changes in secondary loop. (Helium Only)

As seen from the figures, the responses of the systems are nearly identical. The same trend is observed when the stimulus is a step change in the flow rate in the primary loop or the process loop. As expected, an increase in flow rate for a certain stream results in a lower temperature change for that stream, and a decrease in the flow rate will result in a higher temperature change. In most cases, the net heat transferred (heat duty of the heat exchanger described later) decreases, and most streams a decrease in temperature is observed as seen from the figures.

As the temperatures of the streams change, so does the log-mean temperature difference (LMTD) for the heat exchangers. The LMTD response is shown in Figures 3.5 and 3.6 for molten salt and helium, respectively. These responses are also nearly identical to each other. The figures show both the % changes in the LMTD, as well the absolute value of LMTD.

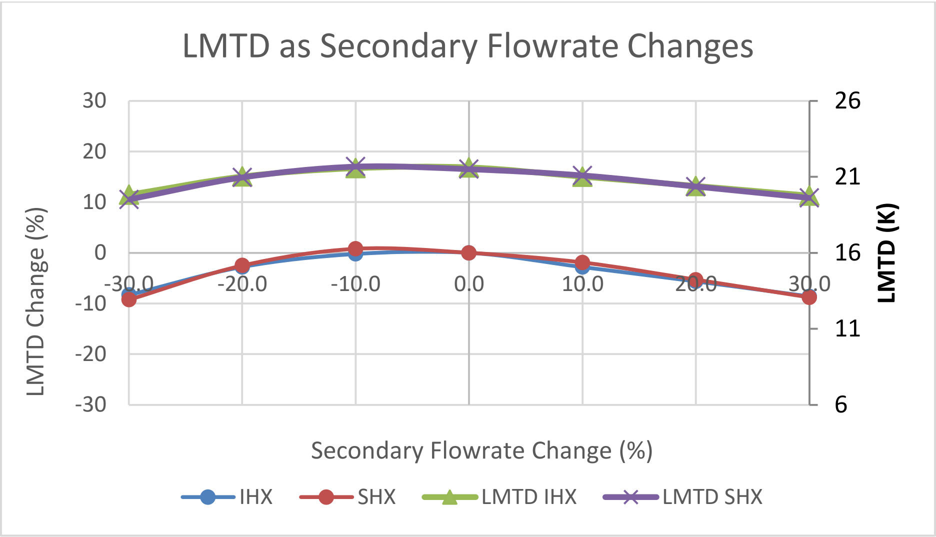

Figure 3.5: LMTD for change in secondary flow rate. (Molten Salt)

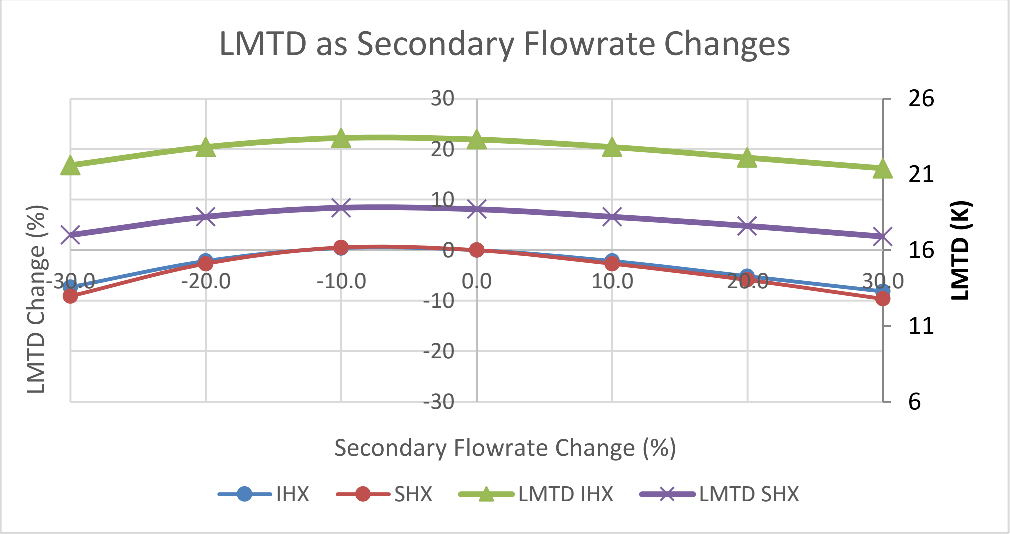

Figure 3.6: LMTD for change in secondary flow rate. (Helium Only)

As seen from the figures, the LMTD decreases upon a departure from the reference flow rate. Figures 3.7 and 3.8 show the overall heat transfer coefficients with the molten salt process and helium loops, respectively. The heat transfer coefficient is a function of Reynolds number, and hence the flow rate. It can be seen that the heat transfer coefficients increase and decrease with an increase and decrease in the flow rate, respectively.

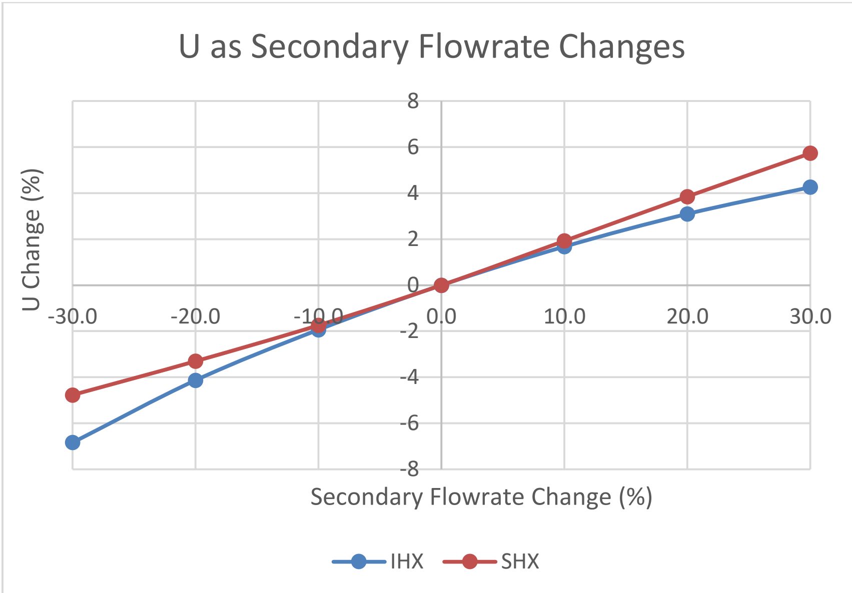

Figure 3.7: Overall heat transfer coefficient as secondary flow rate changes. (Molten Salts)

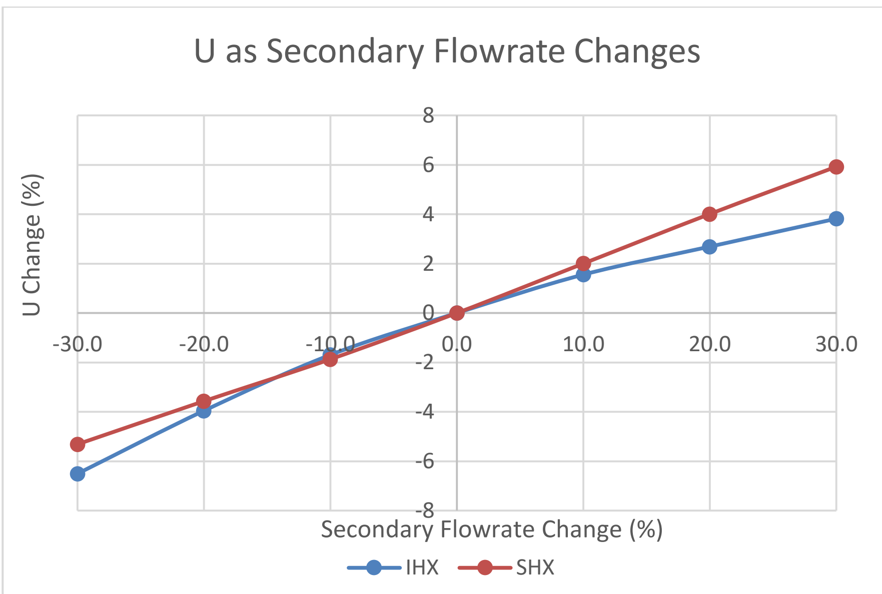

Figure 3.8: Overall heat transfer coefficient as secondary flow rate changes. (Helium Only)

Figures 3.9 and 3.10 show the change in heat duty with the change in flow rate for all 3 of the loops. The heat duty is dependent upon both the heat transfer coefficient, and the LMTD for a heat exchanger of constant area. The heat transfer coefficients increase or decrease, depending upon whether the flow rate has increased or decreased. In combination with the LMTD variation, this leads to a net decrease in the heat duty in all cases, except for the case of increase in the primary flow rate.

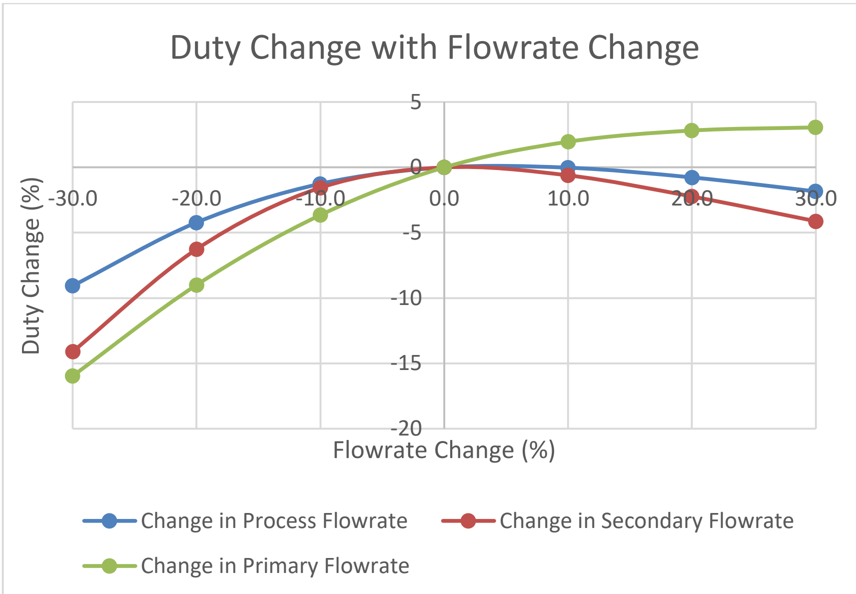

Figure 3.9: Changes in duty with changes in the flow rate of each loop. (Molten Salt)

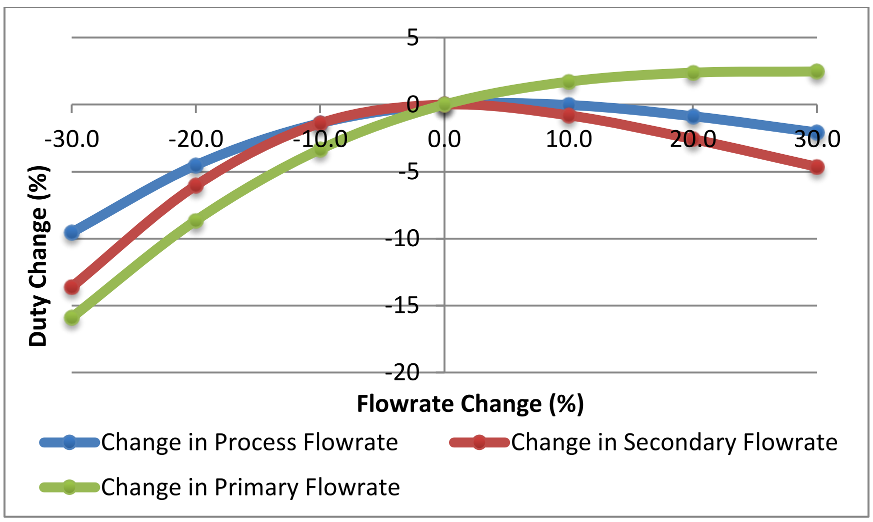

Figure 3.10: Changes in duty with changes in the flow rate of each loop. (Helium only)

It is also found that the flow rate change of a stream causes a change in flow rates of other streams. For example, a change in the flow rate of the secondary loop causes a change in the flow rates in the process and primary loops. This is due to the fact that the resultant temperature changes affect the stream properties. The effect is complex and a quantitative description is not yet developed. The flow rate changes are more pronounced for helium streams than the molten salt streams, as can be seen from figures 3.11 and 3.12.

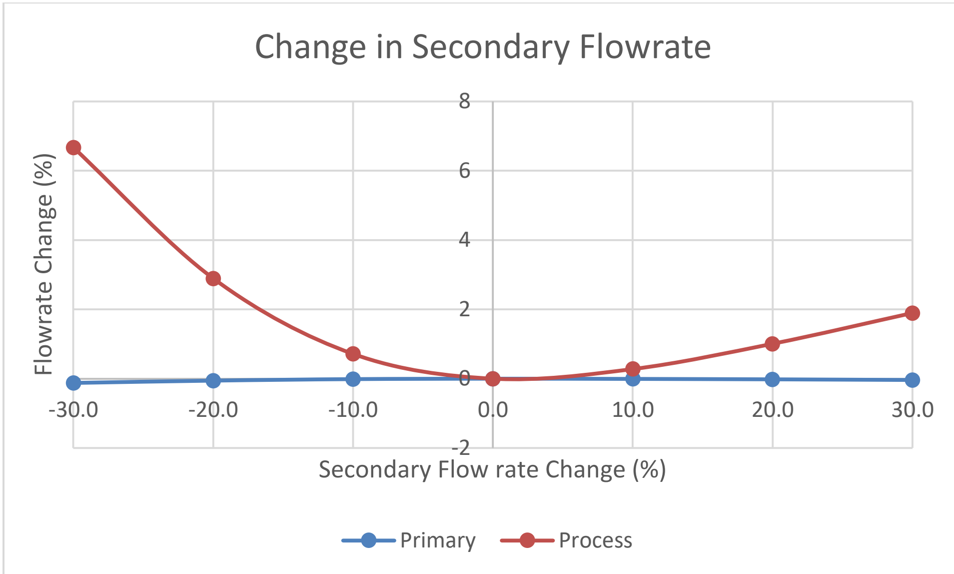

Figure 3.11: Change in flow rates with the secondary flow rate variation. (Molten Salt)

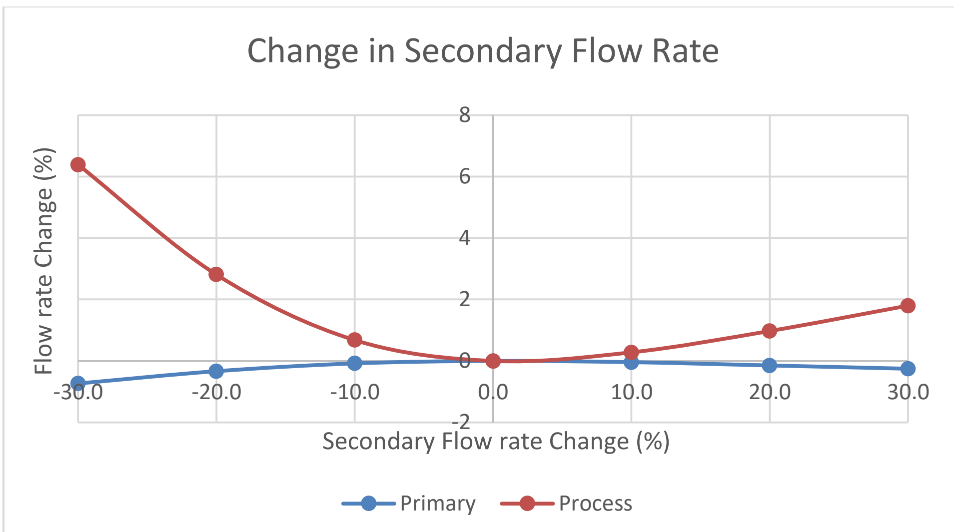

Figure 3.12: Change in flow rates with the secondary flow rate variation. (Helium Only)

The flow rate change is the only aspect that is significantly different when going from an all helium process to a molten salt process. This is because helium is in the gas phase and thus is more affected by temperature. Further, the changes in the primary loop flow rate have larger impacts than secondary or process loop changes. The secondary flow rate can increase by as much as 7% in the all helium system, whereas the increase is barely 2% in the molten salt system. In both the helium only and molten salt processes the process loop has virtually no effect on the flow rates of the other loops.

Figures 3.13 and 3.14 show the change in pressure drop as the secondary flow rate changes. The pressure drop changes correlate well with the flow rate changes shown above.

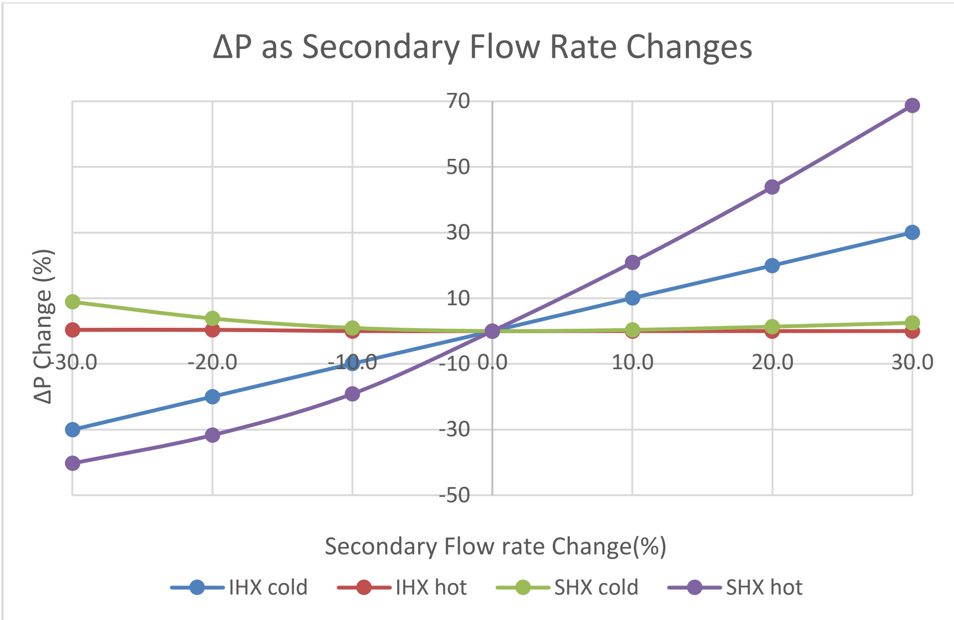

Figure 3.13: Changes in pressure drop with change in secondary flow rate. (Molten Salt)

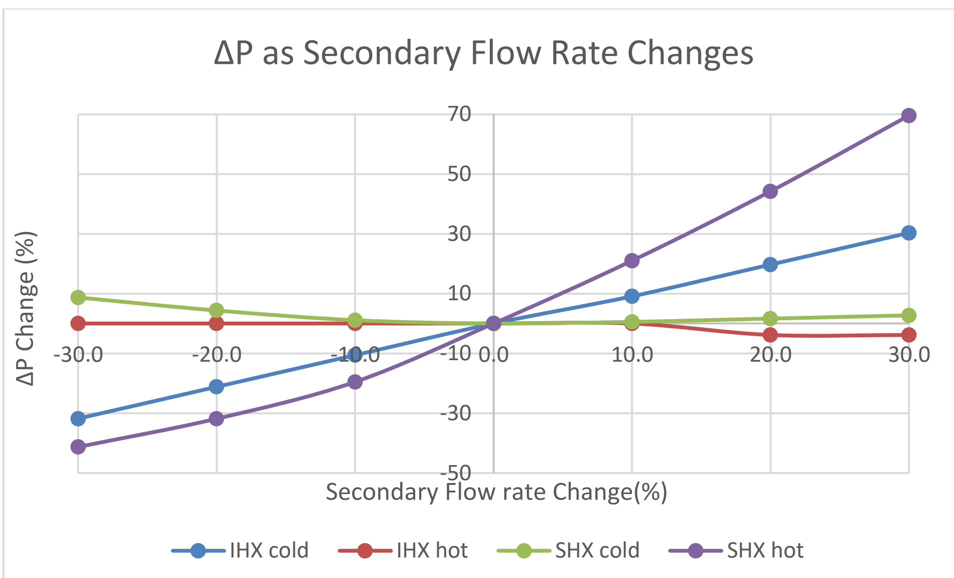

Figure 3.14: Changes in pressure drop with change in secondary flow rate. (Helium Only)

As seen from figures 3.13 and 3.14, the two plots – for helium and molten salt system - are nearly identical. The same phenomena are observed when the stimulus (or forcing function) is a change in the flow rate in the process or primary loop.

Figure 3.15 shows the temperature changes when the flow rate in the process loop increases by 20%. The disturbance is induced at 2 minutes. It can be seen that the temperature of the helium stream exiting the SHX (stream SHX cold out) decreases immediately. The increase in the flow rate causes the heat transfer coefficient to increase. This, coupled with the higher driving force (increased log mean temperature difference (LMTD) between the hot and cold fluids in the SHX), causes the thermal duty of the SHX to increase sharply, as shown in Figure 3.16. This disturbance then propagates through the system, causing the IHX duty to increase slightly, as also seen from Figure 3.16. The thermal duties of both IHX and SHX decrease and approach each other, stabilizing at approximately within 1% of the original duty. The temperature change in the process stream decreases to compensate for the increased flow, as seen from the streams labelled SHX Cold in figure 3.15. However, the temperatures of the rest of the streams do not show significant difference and the eventually new steady state temperatures are reached. The response is rapid, with the temperatures approaching the new steady state in two minutes.

Figures 3.17 and 3.18 show the temperatures of various streams and the thermal duties of the two heat exchangers, respectively, following a 20% increase in the flow rate of the secondary loop fluid. As this fluid flow through both IHX and SHX, the heat transfer coefficients increase in both the heat exchangers, and the thermal duties show spikes for both IHX and SHX. The outlet temperature of the secondary fluid (cold-side fluid in IHX) decreases as its flow rate increases. The outlet temperature of the cold side fluid in SHX, however, increases as the SHX thermal duty has increased. This, in turn, causes the driving force (LMTD in SHX) to decrease which tends to reduce the thermal duty. The interplay of these factors ultimately results in a decrease in thermal duties and stabilization of various stream temperatures at new values as seen from Figures 3.17 and 3.18. The overall response of the system is slightly slower than in the first case, where the disturbance was introduced in the process stream.

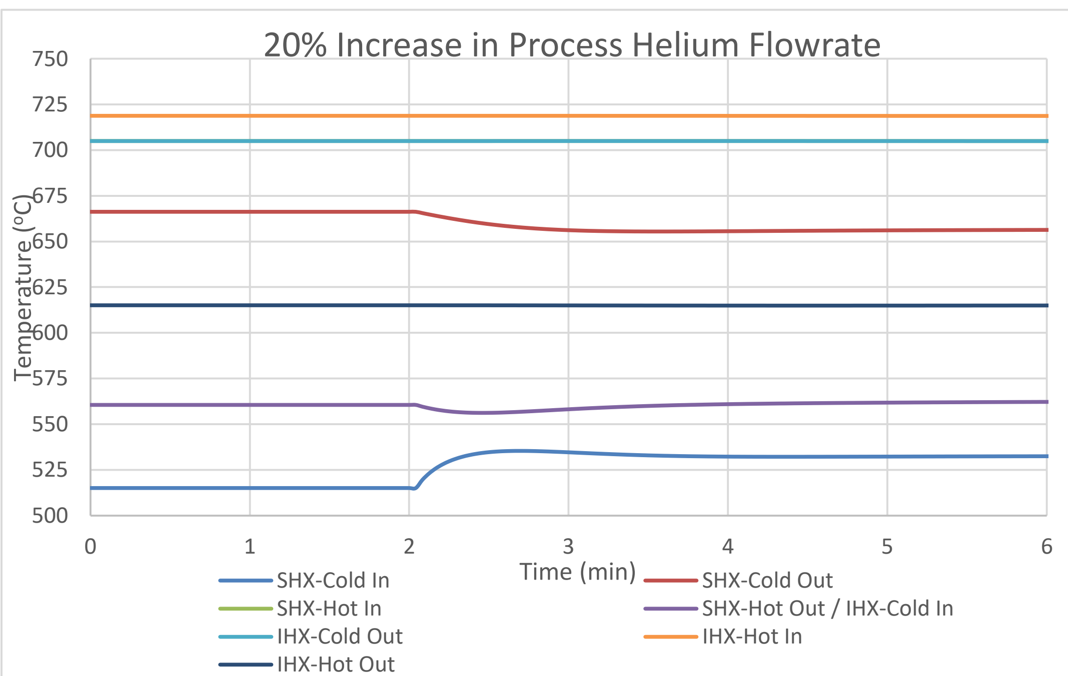

Figure 3.15: Temperatures after Step Change in Flow Rate in Process Loop.

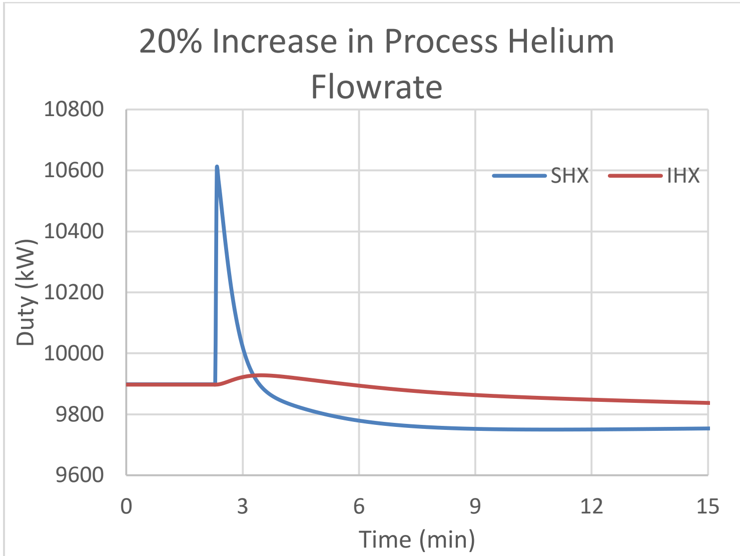

Figure 3.16: Heat Exchanger Duties after Step Change in Process Loop.

Figures 3.19 and 3.20 show the temperature and thermal duty response when the flow rate of the coolant in the primary loop increases by 20%.

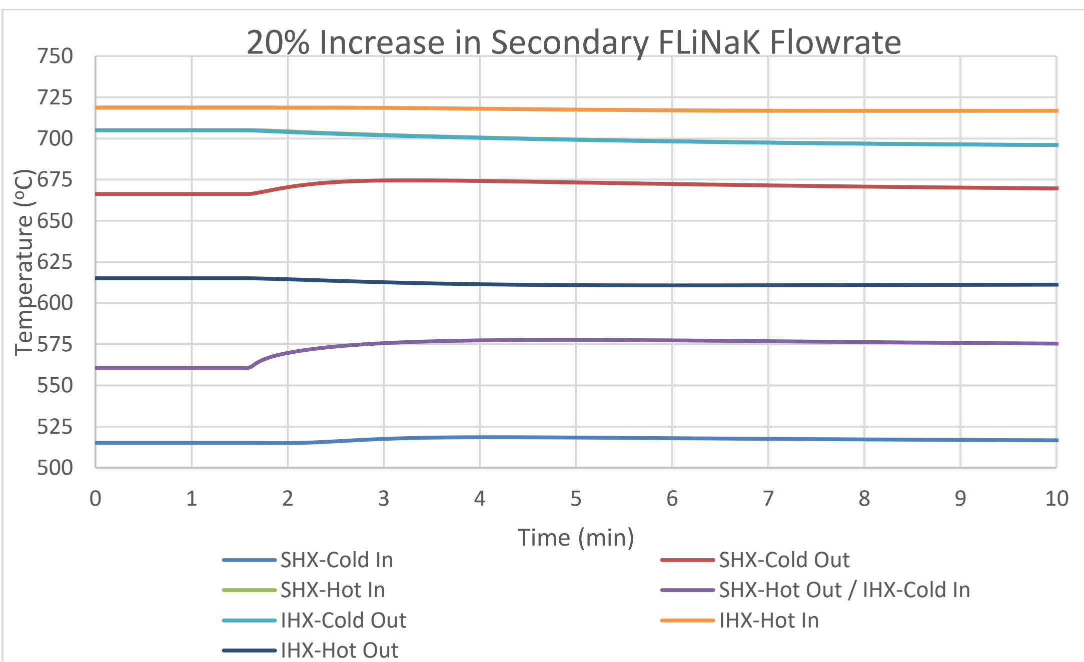

Figure 3.17: Temperatures after Step Change in Secondary Loop.

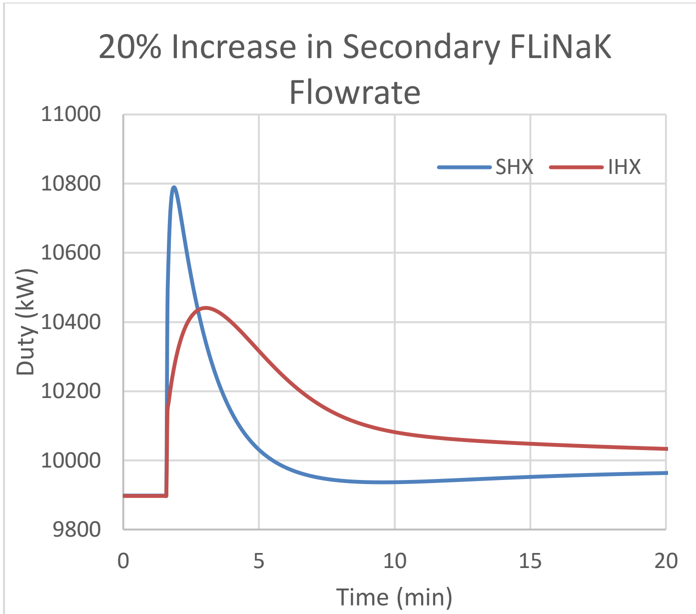

Figure 3.18: Heat Exchanger Duties after Step Change in Secondary Loop.

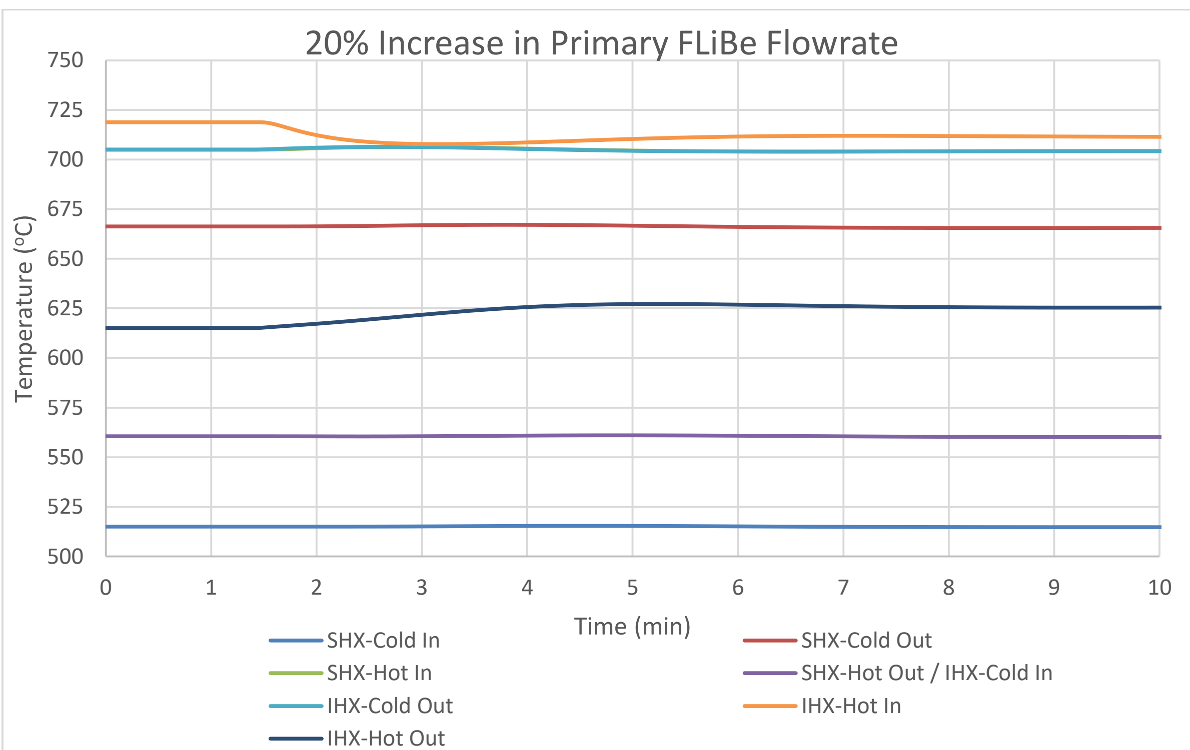

Figure 3.19: Temperatures after Ctep Change in Primary Loop.

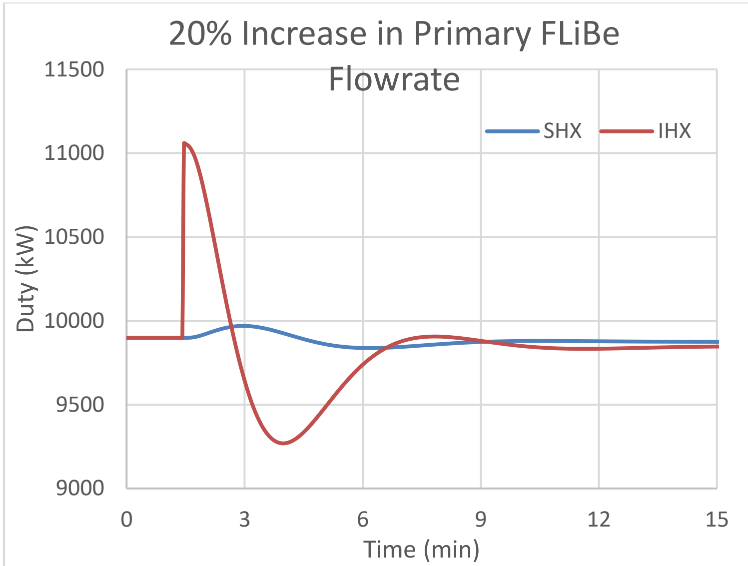

Figure 3.20: Heat Exchanger Duties after Step Change in Primary Loop.

Increase in the flow rate of the primary coolant (FLiBe) results in lowering of its temperature (as it is carrying the reactor power). The interplay between increased heat transfer coefficient and decreased driving force as described above results in the temperature and thermal duty transients as shown the figures. The response of the system is faster than that for the disturbance in the secondary loop, but slower than that in the process loop.

3.1.4 Incorporation of Nuclear Reactor in Dynsim

None of the chemical process simulation softwares include a nuclear reactor as a process unit. The thermal aspects of the reactor transients can, however, be simulated through a creative arrangement of heat exchangers. This arrangement is shown in figure 3.21. The components of this system (S: stream, E: heat exchanger, R: reactor) are as follows:

S2: Inlet of FLiBe into the "nuclear reactor"

S5: Outlet of FLiBe from the "nuclear reactor"

E1/E2: heat exchangers used to help simulate reactor.

R1: Chemical reactor where heat is created from the reaction that occurs.

S22/S24/S3/S4: These streams are all in the "nuclear reactor" and have compounds that react to generate heat.

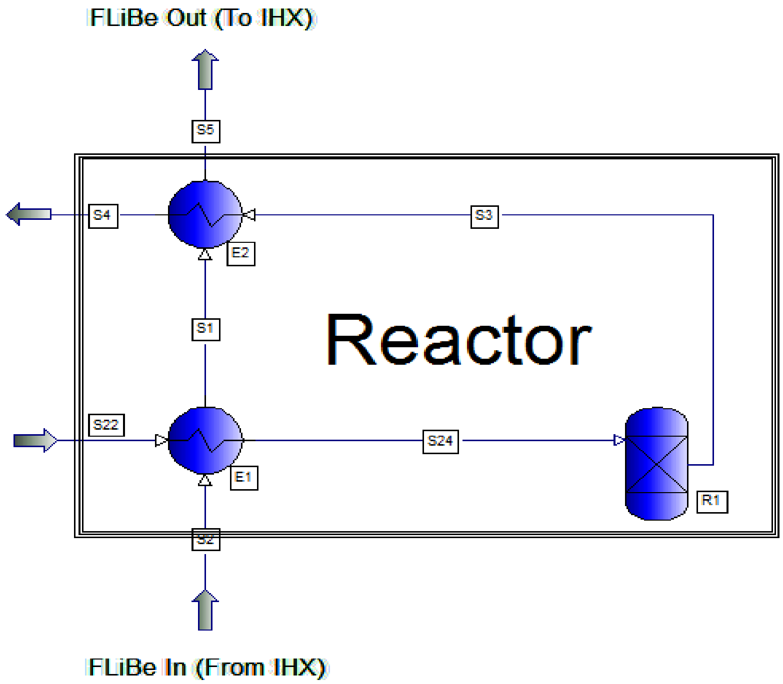

Figure 3.21: Flow loop for simulating nuclear reactor.

<u>Explanation of process:</u>

S2 (FLiBe) enters **E1** and heats up **S22.** The exiting stress, **S24,** enters **R1,** which is a chemical reactor where a reaction occurs. The reaction is exothermic and thus as the compounds react the temperature rises. The extent of reaction is controlled by inlet conditions represented by the following equation.

Extent of reaction = A + B*T + C*T^2

By adjusting the flowrate and these constants one can get the desired inlet and outlet temperatures. The exit temperature for **S3** is determined by inlet conditions and the equation above and this then stream enters **E2** to heat up the FLiBe stream to a certain desired temperature and exits as stream **S5.** This stream then goes on to enter the hot side of the IHX.

Figure 3.22 shows the reactor power after an increase in the inlet temperature, as obtained from above scheme. Figure 3.23 shows a plot of the reactor power found by a Matlab code.

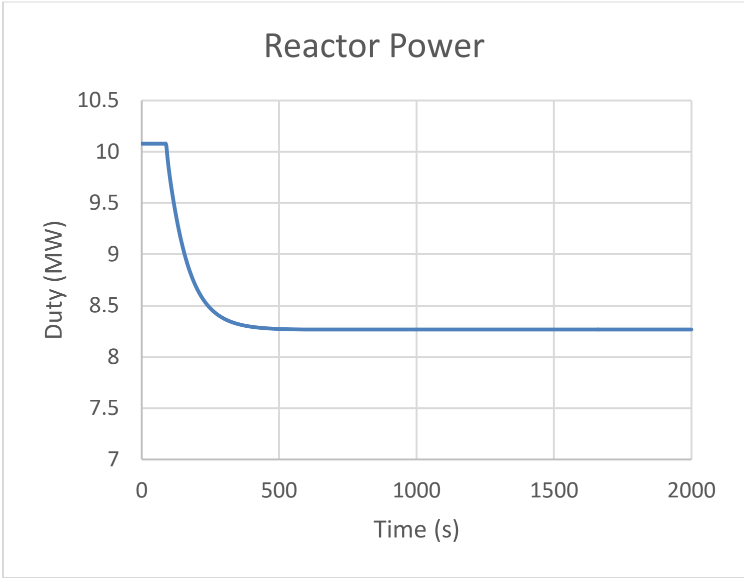

Figure 3.22: Reactor power found in Dynsim after 20 ^{O}C increase in inlet of reactor.

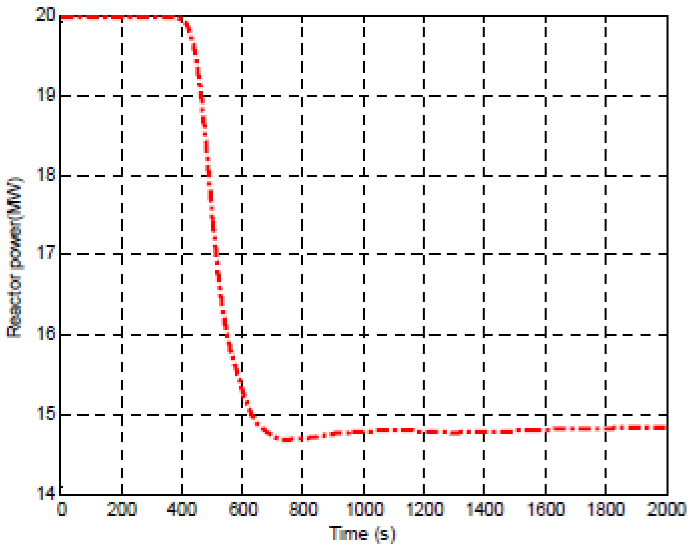

Figure 3.23: Reactor power found using MATLAB.

The reactor power decreases with an increase in the primary coolant temperature, as expected. Both figure 3.22 and 3.23 indicate that a new equilibrium is reached within approximately 400 seconds. Thus this technique appears to hold promise, and further refinements are being made to confirm that it is able to simulate the thermal response of the nuclear reactor under various scenarios both qualitatively and quantitatively.

3.1.5 Transients after Temperature Disturbances

A temperature disturbance is introduced in the primary loop through the tank SRC1 (figure 3.1). A step change can be introduced by specifying the outlet temperature of the tank. Transient temperatures for a 30ºC increase in the temperature of the primary coolant (FLiBe) are shown in figure 3.24. The disturbance is introduced after about 90 minutes of operation at the initial steady state.

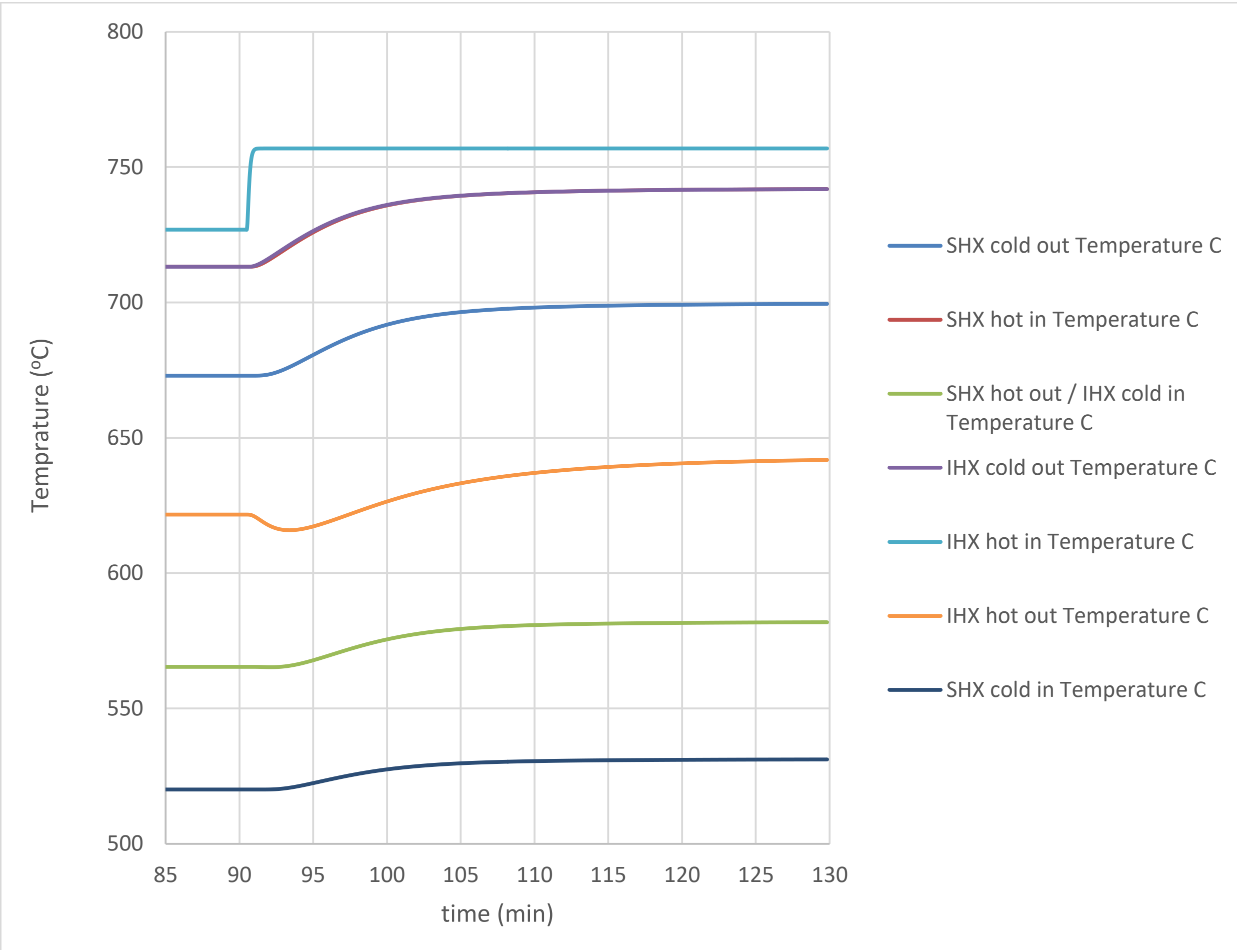

Figure 3.24: Temperature step of 30^{O}C in primary loop.

As the temperature of the primary coolant entering the IHX increases, the temperature of the rest of the streams increase as well, reaching new steady states. If the disturbance is in the opposite direction (decrease in the primary coolant temperature), then the new steady state temperatures are lower than the initial temperatures. Figure 3.25 shows the resultant thermal duties of the IHX and SHX for the 30ºC increase in the primary loop. The thermal duty increases with the higher primary coolant temperature, as expected.

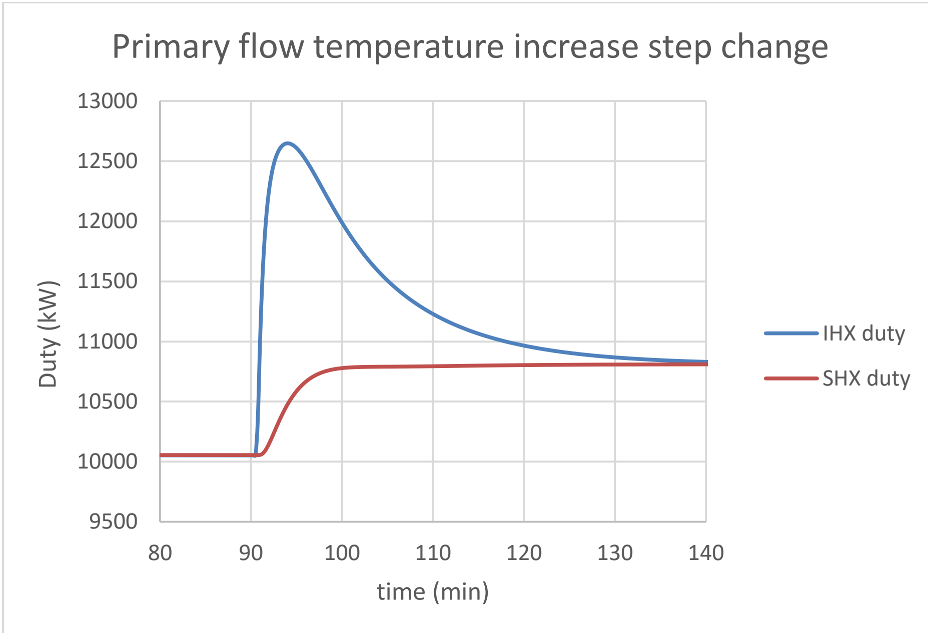

Figure 3.25: Heat Exchanger Duties after Temperature Step Change in Primary Loop.

Figure 3.26 shows the effect of a 30°C increase in the temperature of the process stream.

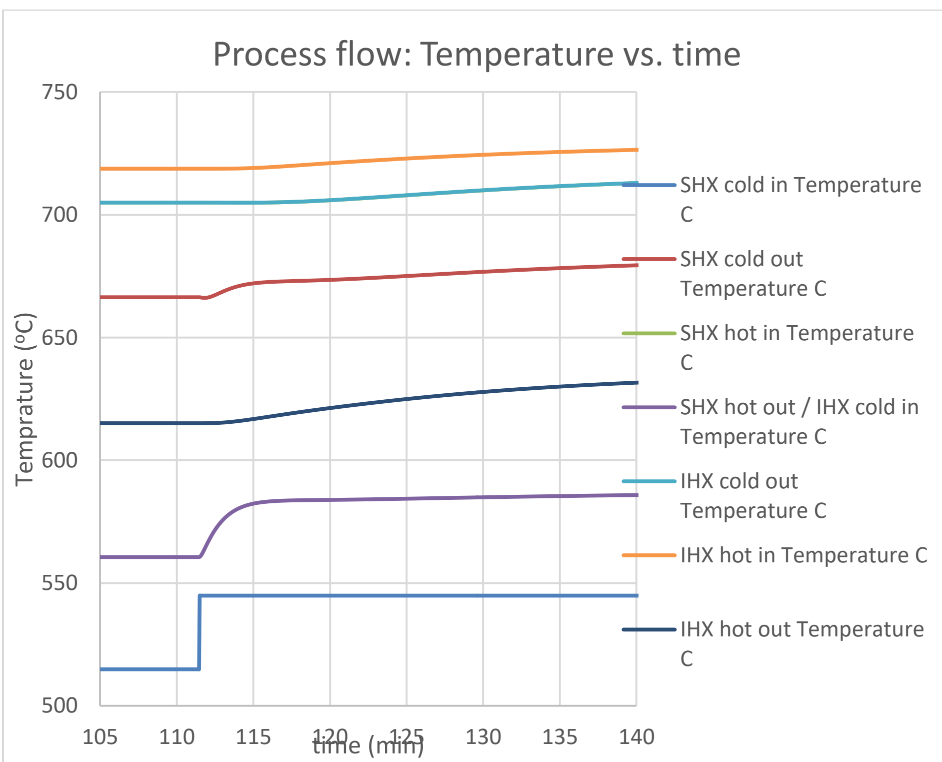

Figure 3.26: Temperature Step of $30^{O}C$ in Process Loop.

As expected, the temperatures of the rest of the streams increase as well. The thermal duties are as shown in Figure 3.27. Both IHX and SHX thermal duties approach new steady state values that are lower than the initial steady state value. This is expected, as an increased temperature in the process loop results in a lower driving force (LMTD) in SHX. The disturbance propagates through the system, lowering the duties.

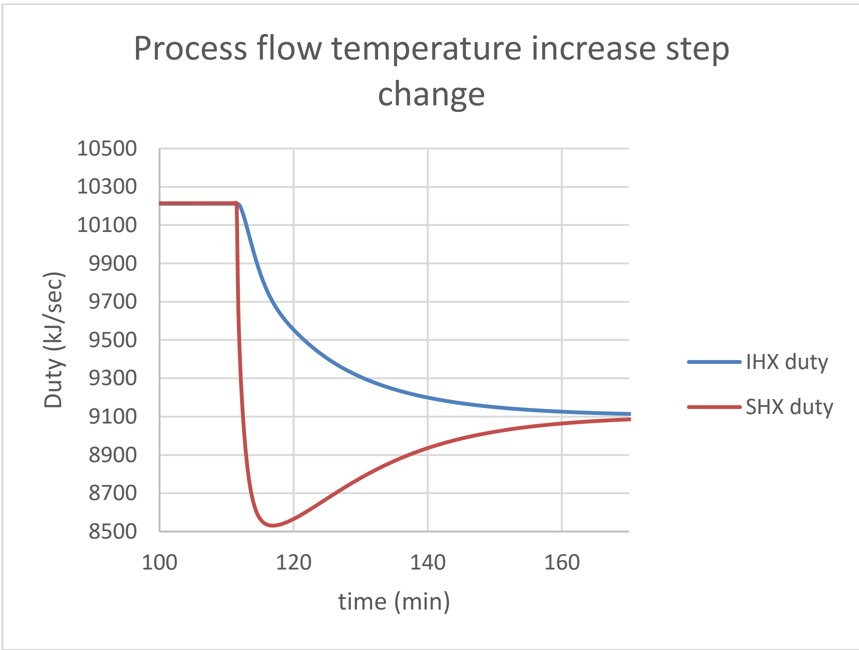

Figure 3.27: Heat Exchanger Duties after Temperature Step Change in Process Loop.

The temperature transients have the following features are noted regarding the temperature transients:

1. The system response for temperature disturbances are much slower than those for flow rate changes.
2. The magnitude of offset (difference between initial and new steady temperatures) is greater in the loop where the disturbance occurs, the loop farthest away showing smaller deviation. For example, the IHX outlet temperature change by nearly the same amount as the disturbance (30ºC) in primary loop, while the process loop temperature changes by only ~11ºC. Similarly for disturbance in the process loop, the SHX temperatures change by ~26ºC (for a 30ºC disturbance) while the primary loop temperature changes only by 7ºC.
3. The system response is faster for the disturbance in the primary loop as compared to that in the process loop.

3.1.6 Process Simulation Results Summary

The process simulation softwares have been applied to obtain transient system response for flow rate and temperature changes. The thermal response of the nuclear reactor has also been simulated using a combination of heat exchangers and a chemical reactor. The combination of PRO/II and Dynsim allows us to simulate the transient conditions possible in the advanced reactor-heat exchanger-process application system. The resultant conditions after the step changes show a trend that is consistent with the heat transfer theory.

3.2. Mathematical Modeling using User-Developed Programs

The dynamic model to evaluate the performance of the PCHE was developed based on the energy balance equations of a two-stream countercurrent heat exchanger with the following assumptions:

1. Helium low distribution into channels was assumed uniform;
2. Heat conduction in the solid plates and working fluids in the flow directions was assumed negligible;
3. Heat loss to the surroundings via the heat exchanger surfaces was neglected;
4. Constant specific heat was used for helium; and
5. Heat conduction resistance in the plate between the hot channels and cold channels was neglected because of the thin plate and large thermal conductivity of the plate material (i.e., Alloy 617).

Two control volumes for the fluids inside two flow channels and a control volume in one of the non-etched portion on plate are illustrated in Fig. . Based on the aforementioned assumptions, integrating the energy balance equations over the PCHE, one is able to derive the following equations:

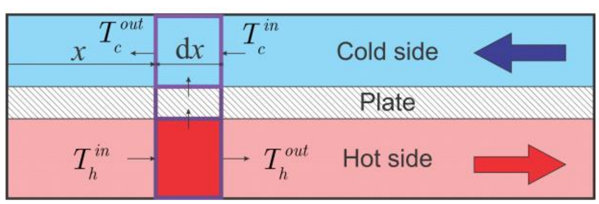

Fig. 3.29. Control volumes for two fluids and solid plate.

For the hot-side fluid:

$$m_h c_{p,h} \frac{\mathrm{d}T_h}{\mathrm{d}t} + \dot{m}_h c_{p,h} \left(T_h^{out} - T_h^{in}\right) = \left(hA\right)_h \left(T_P - T_h\right) \tag{3.2}$$

For the cold-side fluid:

$$m_c c_{p,c} \frac{\mathrm{d}T_c}{\mathrm{d}t} + \dot{m}_c c_{p,c} \left(T_c^{out} - T_c^{in}\right) = \left(hA\right)_c \left(T_P - T_c\right) \tag{3.3}$$

For the solid plate:

$$m_P c_{p,P} \frac{\mathrm{d}T_P}{\mathrm{d}t} = \left(hA\right)_h \left(T_h - T_P\right) - \left(hA\right)_c \left(T_P - T_c\right) \tag{3.4}$$

Here, the subscripts *h*, *c*, and *P* denote the PCHE hot-side fluid, cold-side fluid, and solid plate, respectively. A is the total heat transfer area in one segment of the PCHE. Superscripts *in* and *out* denote the inlet and outlet temperatures for a specific volume, respectively.

3.2.1 Steady-state simulations

Figure 3.30 presents the PCHE system nodal structure. A preliminary nodalization sensitivity study was performed to determine the effective number of segments used in the transient simulations based on one of the experimental steady-state conditions. Five different numbers of segments were used in the nodalization sensitivity study. The temperatures at the hot-side and cold-side outlets were recorded after the system reached a steady state in the calculation using the numerical model. These two outlet temperatures were compared to the parameters that were obtained from the heat exchanger rating process using $e-\mathrm{NTU}$ method. It can be seen from Table 3.4 that five cases presented similar results without significant deviations. The hot-side and cold-side temperature differences between the values using $e-\mathrm{NTU}$ method and the results obtained from the simulations for five cases with different number of segments were mainly attributed to the fluid thermophysical properties. The fluid thermophysical properties were kept same for each helium stream in the heat exchanger rating process, while the temperature-dependent properties were evaluated in each segment in the numerical simulations. Note that increasing the number of segments would considerably increase the computational time. It is observed from Table 3.4 that the outlet temperature differences on both sides tended to diminish when the total number of segments was greater than 500. Therefore, a total of 500 segments of the PCHE were selected to simulate the transient scenarios in this study.

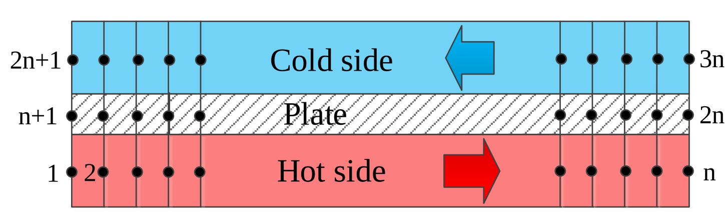

Fig. 3.30. PCHE nodal structure.

Table 3.4. Results of nodalization sensitivity study

	PCHE e - NTU rating value	Number of segments				
		50	100	300	500	1000
Hot-side outlet temperature (ºC)	294	294	293.7	293.6	293.6	293.5
Cold-side outlet temperature (ºC)	379.2	379.5	379.2	379.0	379.0	379.0

To predict the dynamic behavior of the straight-channel PCHE, steady-state operating parameters were calculated initially by assuming the helium fluid properties were constant. The input parameters for the calculation were inlet temperatures on both the hot and cold sides. The temperature distributions inside the PCHE, as shown in Figure 3.31, were obtained by dividing one hot helium stream, one cold helium stream, and one plate into 500 segments along the helium flow direction. The steady-state temperatures inside the PCHE and helium mass flow rates can serve as the initial condition for the transient simulations.

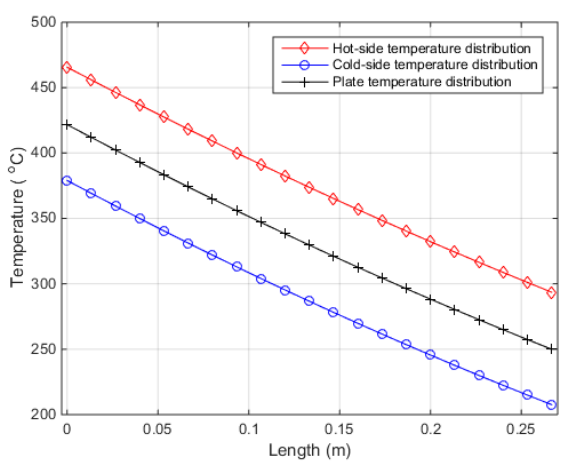

Fig. 3.31. Temperature distributions inside the reduced-scale straight-channel PCHE.

3.2.2 Transient simulations for Straight-Channel PCHE

A series of transient scenarios were performed to study the dynamic behavior of the PCHE and also to assess the applicability of the dynamic model for use in the straight-channel PCHE under high-temperature helium-helium conditions. For inlet temperature variations and helium mass flow rate variations, the combinations of step change on one side and linear ramp change on the other side were performed separately. For the PCHE subject to combinations of the inlet temperature and helium mass flow rate variations, four cases that the PCHE would experience the highest and the lowest temperature among the variation combinations were conducted. The detailed numerical simulation matrix is listed in Table 3.5.

Table 3.5. Numerical simulation matrix

Case	Hot-side inlet	Cold-side inlet
	Temperature variations	
HSICRD	50°C step increase	50°C linear ramp decrease within 10 seconds
HSDCRI	50°C step decrease	50°C linear ramp increase within 10 seconds
HRICSD	50°C linear ramp increase within 10 seconds	50°C step decrease
HRDCSI	50°C linear ramp decrease within 10 seconds	50°C step increase
	Helium mass flow rate variations	
HSICRI	20% step increase	20% linear ramp increase within 10 seconds
HSDCRD	20% step decrease	20% linear ramp decrease within 10 seconds
HRICSI	20% linear ramp increase within 10 seconds	20% step increase
HRDCSD	20% linear ramp decrease within 10 seconds	20% step decrease
	Inlet temperature combined with helium mass flow rate variations	
TSI-HSICSD	50°C step increase	50°C step increase
	20% flow rate step increase	20% flow rate step decrease
TRI-HRICRD	50°C linear ramp increase within 10 seconds	50°C linear ramp increase within 10 seconds
	20% flow rate linear ramp increase within 10 seconds	20% flow rate linear ramp decrease within 10 seconds
TSD-HSDCSI	50°C step decrease	50°C step decrease
	20% flow rate step decrease	20% flow ratestep increase
TRD-HRDCRI	50°C linear ramp decrease within 10 seconds	50°C linear ramp decrease within 10 seconds
	20% flow rate linear ramp decrease within 10 seconds	20% flow rate linear ramp increase within 10 seconds

3.2.2.1. Inlet temperature variations

The dynamic behavior of the PCHE subject to inlet temperature variations when the helium mass flow rates on both sides were maintained at constant was studied. The velocities were kept at 26.6 and 23.2 m/s on the hot side and cold side, respectively. Figure 3.32 shows the hot-side and cold-side outlet temperature dynamic response due to four kinds of inlet temperature variation combinations at 10 seconds. For both the HSICRD and HRDCSI cases, the cold-side and hot-side outlet temperatures had an overshoot at the beginning of transients. Conversely, undershoots were observed at outlets on both sides for both the HRICSD and HSDCRI cases. This can be explained by step changes dominating transient scenarios during the initial stage. It took approximately 15 seconds for temperatures to stabilize on both the hot and cold sides for all these temperature variations. It also can be seen from Figure 3.32 that outlet temperatures for both the HSICRD and HRICSD transient cases were the same after the final steady states were reached in the calculation. Similar behavior was presented for the other two temperature variation transients. These results indicate that the final steady state is only determined by the amount of temperature change at the beginning and is not sensitive to the way of temperature change (ramp or step).

For the HSICRD and HRICSD cases, the hot-side outlet temperatures decreased from 293.6 to 271.2°C and the cold-side outlet temperatures increased from 379 to 387 °C. The effectiveness of the reduced-scale PCHE under the initial steady state was 67%. The heat exchanger effectiveness reduced to 64% after temperature variations. However, the hot-side temperature increase combined with the cold-side temperature decrease resulted in 38% more thermal energy transferring from the hot side to the cold side. The energy rate balance deviations were about 6.14% between the hot side and the cold side in the final steady-state condition. For the HSDCRI and HRDCSI transient cases, the hot-side outlet temperature increased to 313°C and the cold-side outlet temperature decreased to 365.8°C. The combination of the hot-side temperature decrease and the cold-side temperature increase reduced 38.6% of the thermal energy transferring from the hot side to the cold side. The hot-side and cold-side energy rate balances were within a deviation of 5.5%. Compared to the initial operation parameters, the heat exchanger effectiveness slightly increased to 68%.

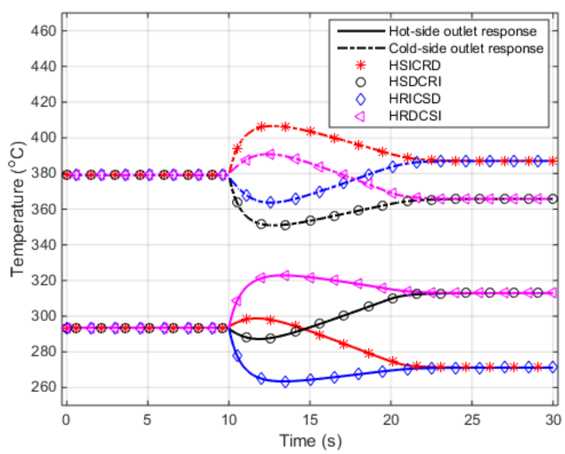

Fig. 3.32. PCHE dynamic response for inlet temperature variations.

3.2.2.2 Helium mass flow rate variations

In this section, dynamic response of the simulated PCHE subject to four kinds of helium mass flow rate variation combinations was analyzed. The four helium mass flow rate transient scenarios are listed in Table 3.4. Only helium mass flow rate was treated for each instance. That is, inlet temperatures were kept constant on both sides for those simulations. Figure 3.33 shows the dynamic temperature response when the helium mass flow rates on both sides were changed at 10 seconds into the transient. It can be seen that outlet temperatures on both sides increased for the helium mass flow rates step increase on the hot side or step decrease on the cold side at the beginning of the transients. The same final steady-state conditions were reached for either the helium mass flow rates increase on both sides or decrease in the calculation. The hot-side outlet temperatures decreased from 293.6 to 290.9°C and the cold-side outlet temperatures increased from 379 to 382.2°C for the helium mass flow rates increase combination and decrease combination, respectively. More thermal energy carried by fluid would go into the heat exchanger due to the increase of the helium mass flow rate on the hot side while more thermal energy would be removed from the heat exchanger due to the increase of the cold-side helium mass flow rate. The hot-side heat transfer coefficients increased by 26.8% (i.e., from 1,167 to 1,480 W/(m^2-ºC)) and decreased by 13.2% (i.e., from 1,167 to 1,013 W/(m^2-ºC)) due to the hot-side helium mass flow rate increase and decrease, respectively. The cold-side heat transfer coefficients for the helium mass flow rate step increase and step decrease rose by 26.3% (i.e., from 1,201 to 1,517 W/(m^2·ºC)) and reduced by 18.7% (i.e., from 1,201 to 976 W/(m^2·ºC)), respectively. The increasing helium mass flow rates on both sides resulted in 1.8% more thermal energy transferring from the heat exchanger's hot side to the cold side. It also can be calculated that 1.7% more thermal energy was exchanged for the decreasing helium mass flow rate combinations. The energy rate balance deviations were approximately 0.11% and 0.06% after the steady states were reached for the helium mass flow rate increase and decrease combinations, respectively.

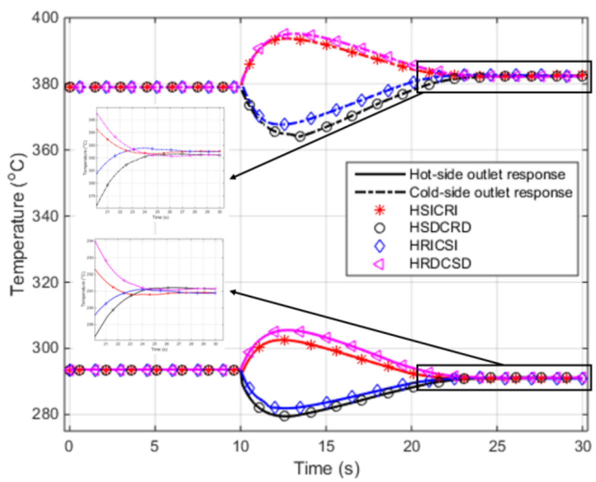

Fig. 3.33. PCHE dynamic response for helium mass flow rate variations.

3.2.2.3. Inlet temperature and helium mass flow rate variation combinations

The PCHE may experience a condition of the highest temperature when both inlets encounter a temperature increase, helium mass flow rate increases on the hot side and decreases on the cold side. On the contrary, the PCHE would undergo a condition of the lowest temperature. Both conditions were studied in this section with the same amounts of change as the inlet temperature variations and helium mass flow rate variations conducted in previous sections (i.e., 50°C step changes and helium mass flow rate 20%-step changes). The transient test matrix is listed in Table 3.4. Figure 3.34 presents outlet temperature evolutions for these four transient scenarios. The highest outlet temperature on the cold and hot sides were 471.4 and 374.9°C, respectively. The lowest outlet temperature on the cold and hot side were 284.2 and 219.3°C, respectively. The heat exchanger effectiveness increased from 67% to 83% for the inlet temperature increasing transient cases, while decreased to 49% for the inlet temperature decreasing scenarios. Compared to the initial operating condition, the thermal energy transferred from the heat exchanger's hot side to cold side reduced by 10% for the lowest temperature cases. This study provides useful information for operating the PCHE since the temperature variations combined with helium mass flow rate variations would potentially lead to an overheating or overcooling condition for the PCHE.

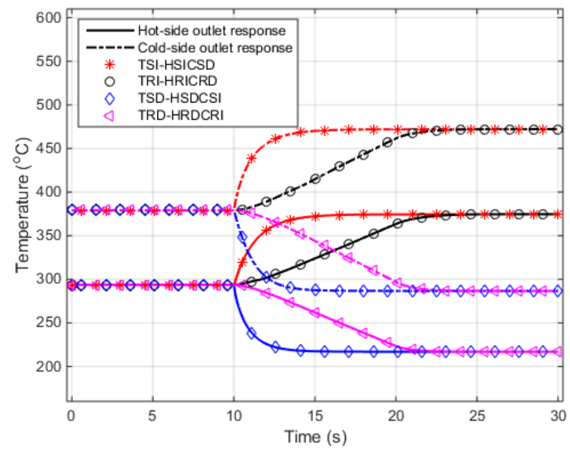

Fig. 3.34. Temperature evolutions for inlet temperature combined with helium mass flow rate variations

In all, for the dynamic response to 50°C variation in temperatures of the tested PCHE, inlet temperature increased on the hot side combined with temperature decreased on the cold side would enhance the heat transfer capability of the heat exchanger while reduce the effectiveness. On the contrary, inlet temperature decreased 50°C on the hot side combined with temperature increased 50°C on the cold side would increase the heat exchanger effectiveness but reduce the heat transfer capability. For the 20% of helium mass flow rate variation combinations, both the heat exchanger effectiveness and heat transfer capability would increase. The dynamic study contributes meaningful instruction to improve the heat exchanger efficiency when operating the PCHE under dynamic conditions. It also provides some basis for designing control strategies to effectively control the PCHE.

3.2.3 Transient simulations for Zig-Zag Channel PCHE

The dynamic system model was tested using the following transient scenarios: 1. 50°C-step increase separately in the helium inlet temperatures on the PCHE hot side and cold side, 2. 50°C-step decrease separately in the helium inlet temperatures on the PCHE hot side and cold side, 3. 20%-step increase separately in the helium mass flow rates on the PCHE hot side and cold side, and 4. 20%-step decrease separately in the helium mass flow rates on the PCHE hot side and cold side. It is assumed that only one transient is manipulated at each time. For example, mass flow rates are kept constant on both sides when performing simulations of temperature variations and the inlet temperatures on both sides are kept constant when conducting simulations of mass flow rate variations.

3.2.3.1 Response to temperature variations

Figures 3.35 and 3.36 show PCHE dynamic responses to inlet temperature step changes. As noted before, the mass flow rates in both sides were kept constant (26.45 kg/h) when simulating the temperature step-increase transient scenarios. Hence the fluid velocities were 53.7 and 47.1 m/s on the hot side and cold side, respectively. Figure 3.35 shows the hot-side and cold-side outlet temperature dynamic responses due to the 50ºC-step increase at the hot-side inlet at 10 seconds. The cold-side outlet temperature increases from 685.9 to 724ºC after the temperature step increase at the hot-side inlet and the hot-side outlet temperature increases from 462.6 to 471.1ºC. It takes approximate five seconds for temperatures to be stabilized on both the hot and cold sides. The hot-side temperature step increase results in 11.82% more energy transferring from the hot side to the cold side. After the steady-state operation is reached, the energy balance deviation is about 1.3% between the hot side and the cold side. The effectiveness of the reduced-scale PCHE under nominal operation condition is 75%. After the hot-side inlet temperature step increase, the heat exchanger effectiveness slightly increases to 75.8%. Figure 2.35 also shows the hot-side and cold-side outlet temperature variations due to the 50ºC-step decrease at the hot-side inlet at 10 seconds. The cold-side outlet temperature decreases from 685.9 to 648ºC after the temperature step decrease at the hot-side inlet and the hot-side outlet temperature decreases to 453.5ºC. It also takes approximate five seconds for temperatures to be stabilized on both the hot and cold sides. The hot-side inlet temperature step decrease results in 11.8% less energy transferring from the hot side to the cold side. After the steady-state operation is reached, the hot-side and cold-side energy balances are within 0.5% deviation. Compared to the nominal operation parameters, the heat exchanger effectiveness decreases to 74.1%.

Similarly, the hot-side and cold-side outlet temperature variations due to the 50ºC-step increase and decrease at the cold-side inlet at 10 seconds are shown in Fig. 3.36. The lowest temperature position in the heat exchanger is located at the cold-side inlet. Temperature step increase or decrease at cold-side inlet would lead to an average temperature increase or decrease for the entire heat exchanger. For the temperature step increase at the cold-side inlet, hot-side and cold-side outlet temperatures rise from 462.6 and 685.9 to 500.8ºC and 704.6ºC, respectively. Contrary to the temperature step increase at the hot-side inlet, 50ºC-step increase at cold-side inlet reduces the heat transfer capacity of the PCHE by approximate 10.3%. While the heat exchanger effectiveness decreases only 0.2%. For the temperature step decrease at the cold-side inlet, hot-side and cold-side outlet temperatures decrease from 462.6 and 685.9 to 424.2ºC and 664.8ºC, respectively. An additional 9.99% more energy is transferred from the hot side to the cold side in this case. As can be observed from Fig. 3.36, it takes about five seconds for both the hot-side and cold-side temperatures to be stabilized. The heat exchanger effectiveness increases by 0.2% due to the cold-side inlet temperature step decrease. After the steady-state operations are reached, the energy balances are checked to be within 1.8% and 2.9% deviations for the cold-side inlet temperature step increase and step decrease, respectively.

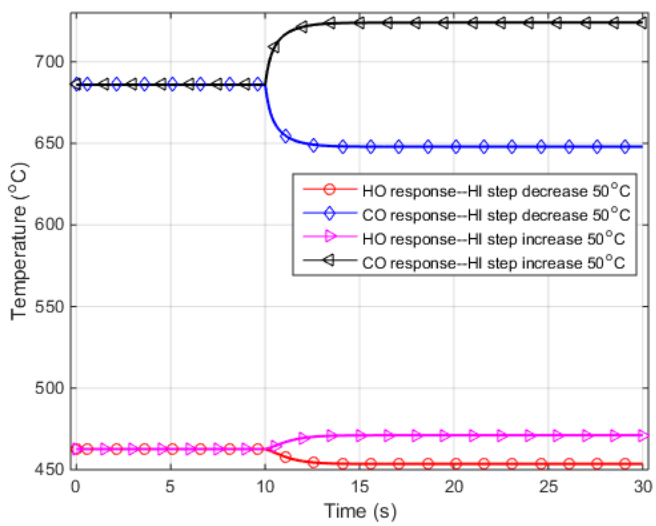

Fig. 3.35. PCHE dynamic responses to hot-side inlet temperature 50ºC-step changes.

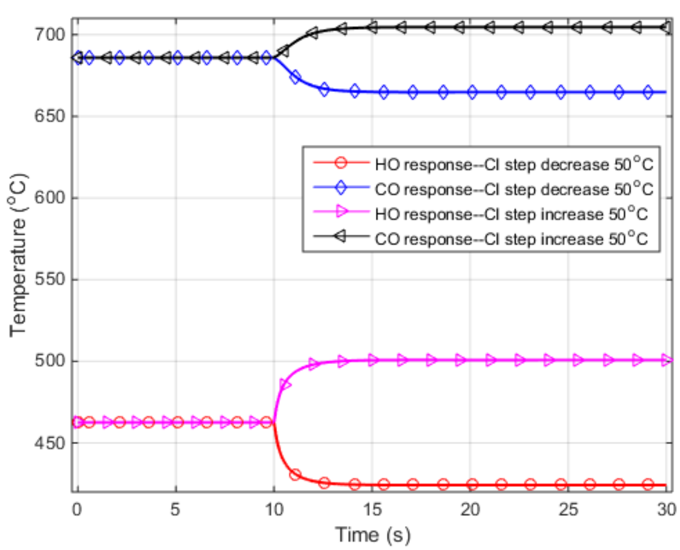

Fig. 3.36. PCHE dynamic responses to cold-side inlet temperature 50ºC-step changes.

3.2.3.2 Response to flow rates variations

Figures 3.37 and 3.38 show PCHE dynamic responses to flow rate variations. The temperatures are kept constant at the inlets of both the hot and cold sides when simulating the flow rate variations. Figure 3.37 shows the dynamic temperature responses when the hot-side mass flow rate increases by 20% (i.e., from 26.45 to 31.74 kg/h) at 10 seconds into the transient. The cold-side inlet mass flow rate is maintained at 26.45 kg/h during the transient. It can be clearly seen that a transient starts at 10 seconds and temperatures for both sides increase until a new steady state is reached. More thermal energy carried by the hot-side fluid goes into the heat exchanger due to the flow rate increase on the hot side. Cold-side and hot-side outlet temperatures increase from 685.9 to 716.2ºC and from 462.6 to 492.6ºC within five seconds. The energy deviation between the hot side and cold side is approximate 1.3% after the flow rate step change. Compared to the nominal operation conditions, the temperature difference on the hot side decreases by 8.9% while it increases by 9.0% on the cold side. The overall heat exchanger effectiveness increases from 75% to 81%. The hot-side mass flow increase results in 9.2% more energy being transferred from the hot side to the cold side. Figure 3.37 also shows the temperature response when the hot-side mass flow rate is decreased by 20% (i.e., from 26.45 to 21.16 kg/h) and the cold-side mass flow rate is fixed at 26.45 kg/h. It is observed that hot-side and cold-side outlet temperatures decrease from 462.6 and 685.9 to 430.8ºC and 643.5ºC, respectively. The effectiveness of the heat exchanger decreases from 75% to 65%. The energy balance deviation is approximately 0.5% after the steady state is reached. The temperature difference on the hot side increase by 9.4% while it reduces by 12.6% on the cold side. The heat transfer capacity is reduced by 12.5% due to the mass flow rate step decrease on the hot side. In addition, the hot-side heat transfer coefficients increase from 2,511 to 2,849 W/(m^2·ºC) and decrease from 2,511 to 2,152 W/(m^2·ºC) due to the hot-side flow rate step increase and step decrease, respectively. Similar transient response analyses are also applied to the situations where the mass flow rate on the cold side is step increased and step decreased. Figure 3.38 shows temperature response when the cold-side mass flow rate is increased by 20% at 10 seconds. More energy will be removed from the hot side than the initial steady state due to the increase of the cold-side flow rate, resulting in temperatures decreasing at the outlets of both sides. Figure 3.38 also depicts temperature response when the cold-side mass flow rate decreases by 20% at 10 seconds. Less energy could be removed from the hot side than the initial condition, which leads to a temperature increase at the outlets of both sides. The heat exchanger effectiveness increases by 9% due to the cold-side mass flow rate step decrease while it decreases by 9% for the step increase. The cold-side heat transfer coefficients for the flow rate step increase and step decrease rise from 2,437 to 2,765 W/(m^2·ºC) and reduce from 2,437 to 2,088 W/(m^2·ºC), respectively.

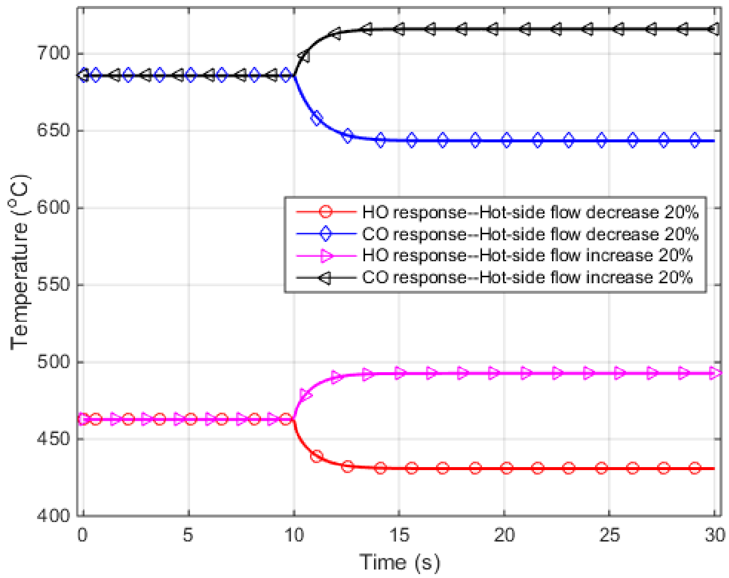

Fig. 3.37. Temperature evolutions following hot-side helium mass flow rate 20%-step changes.

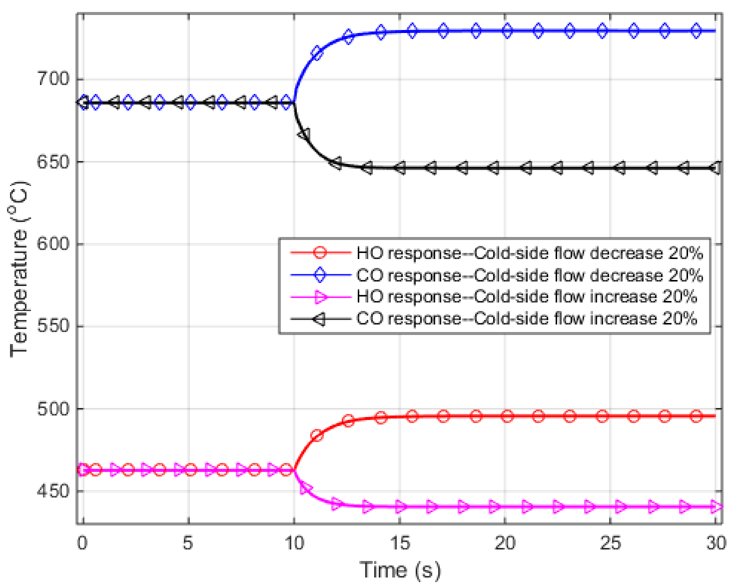

Fig. 3.38. Temperature evolutions following cold-side helium mass flow rate 20%-step changes.

For the dynamic responses to temperature variations, inlet temperature step increase on the hot side or step decrease on the cold side would increase both the heat exchanger effectiveness and heat transfer capacity. On the contrary, inlet temperature step decrease on the hot side or step increase on the cold side would reduce both the heat exchanger effectiveness and heat transfer capacity. For the dynamic responses to the flow rate variations, mass flow rate increases on either side would enhance the heat exchanger capacity while mass flow rate increase on the cold side or decrease on the hot side would lead to a heat exchanger effectiveness decrease.

3.3 Verification

The dynamic model described above was verified by comparing the numerical solution with the results obtained from a commercial software DYNSIM. A general countercurrent two-stream heat exchanger was adopted and the parameters obtained from the design of the heat exchanger under a steady-state condition were fed into DYNSIM to simulate the dynamic behavior of the heat exchanger. Comparison of the results obtained from the dynamic model and DYNSIM is shown in Fig. 3.39. It is evident that the results obtained from the dynamic model and the commercial software DYNSIM present excellent agreement in depicting the dynamic behavior for a 10%-step increase at the cold-side inlet mass flow rate starting at 100 seconds.

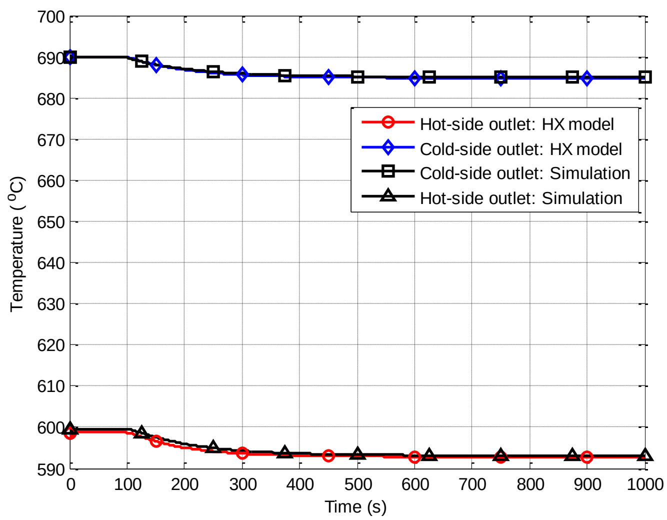

Fig. 3.39. Heat exchanger model verification under flow step change condition.

3.4 Summary

Following conclusions are drawn based on the work conducted on modeling and simulation of transient and off-normal operation of the reactor-heat exchanger system:

1. The process simulation softwares can be successfully applied to simulate the dynamic behavior of the system. Thermal behavior of a nuclear reactor can be mimicked by using a combination of a chemical reactor and heat exchangers.
2. MATLAB codes offer a parallel approach for accomplishing the same purpose.
3. Both techniques yield similar results for flow rate step disturbance.

4. Control System Design and Response

4.1 Advanced Reactor-Heat Exchanger System

The basic schematic of the advanced reactor-intermediate heat exchanger system is shown in Figure 4.1. Steady state system design of the system has been presented earlier by Chen et al. (2015) and Bartel et al. (2015), and used for the development of the control strategy. The nuclear reactor heats up the primary coolant (FLiBe) as it passes through. This coolant travels around the primary loop and enters the intermediate heat exchanger (IHX) where the heat is then transferred to the secondary coolant (FLiNaK). This coolant travels around the secondary loop and enters the secondary heat exchanger (SHX) where it heats up the process coolant (Helium). This coolant is then utilized for either electricity production in the power conversion system (PCS) or for another process (e.g. hydrogen production).

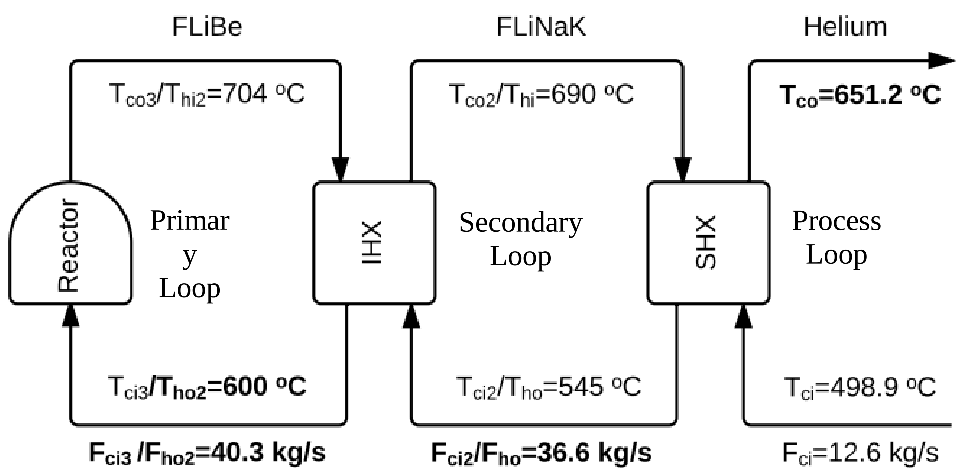

Figure 4.1. Process flow diagram of advanced reactor-heat exchanger system.

Table 4.1 shows the steady state design values that are used for the reactor, IHX and SHX in the system. Further details of the design basis and procedure are available in Chen et al. (2015).

Table 1. Steady state design parameters for AHTR.

		IHX		SHX		Reactor
Variable	**Units**	**cold**	**hot**	**cold**	**Hot**	
T_{in}	K	818	977	772	963	873
T_{out}	K	963	873	924.5	818	977
ΔT	K	145	104	152.3	145	104
F	kg/s	36.6	40.3	12.6	36.6	40.3
Q	kW	10000		10000		10000
ΔT_{lm}	K	30		42.3		-
U	W/(m^2 K)	775		2181		9309
A	m^2	430.1		108.4		

4.2 Helium Brayton Cycle Power Conversion System (PCS)

The generalized schematic shown above assumes that the heat transferred out of the SHX into the process loop can be utilized for either direct application in a process or converted to electricity via a power generation cycle. It is assumed that, for the advanced reactor-heat exchanger system described above, the power conversion system (PCS) involves a helium Brayton cycle shown below in Figure 4.2.

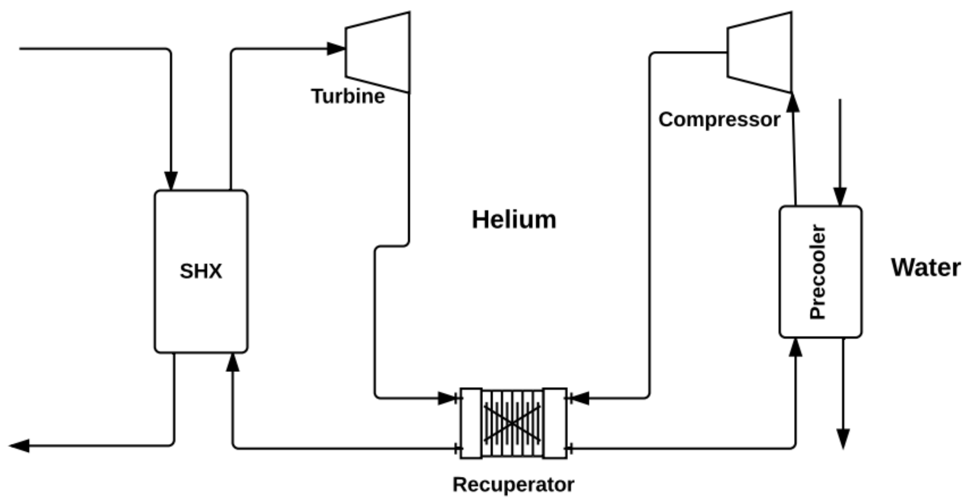

Figure 4.2. Helium Brayton cycle schematic.

The coolant, helium, exits the SHX at a high temperature and enters the turbine. The energy from the turbine spins a generator in which electricity is produced. The pressure drops as the coolant travels through the turbine. The helium enters a recuperator in which the cold side stream exiting the compressor is heated up. Helium then travels through a precooler where water is used to cool down the helium before entering the compressor. Helium enters the compressor where the temperature and pressure of the coolant increase. Compressed helium travels through the recuperator heating up to the desired temperature before entering the SHX again. Control of the helium temperature exiting the SHX is of upmost importance because it has an effect on the overall efficiency of the Brayton cycle.

4.3 Control System Architecture

Creating a control strategy to maintain high system efficiencies requires developing and designing a control system architecture for the system. Figure 4.3 shows a possible control system architecture for the system.

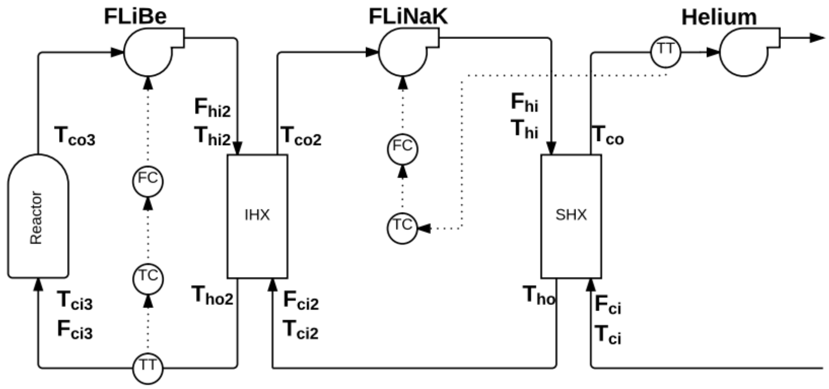

Figure 4.3. Possible design for control of AHTR system.

4.3.1 Control Methodology

The first step in the design of a control system is the identification and selection of the controlled variables (variables maintained at desired set-point values) and manipulated variables (variables changed in order to maintain the controlled variables at their set points). For the SHX, the controlled variable was chosen to be the cold side outlet temperature (T_{co}) of the process coolant. The process coolant travels through the process loop and is used either to generate electricity or provide thermal energy to drive a chemical process. Processes are designed to operate at specified temperatures, and the temperature difference between the process coolant and design temperature provides the necessary driving force for its operation. Controlling the process coolant temperature (T_{co}) will maintain the necessary driving force at the desired value, enabling the process to operate at the optimum efficiency. This control is accomplished by using the hot side flow rate (F_{hi}) or the cold side flow rate (F_{ci}) as the manipulated variable. Other variables, called load variables, represent disturbances that will have an effect on the controlled variable. For the SHX, the load variables include the hot and cold inlet temperatures (T_{hi}, T_{ci}) and the flow rate that is not the manipulated variable (F_{ci} or F_{hi}).

The controlled variable for IHX was the hot side outlet temperature (T_{ho2}). This is the temperature of the primary coolant entering the nuclear reactor. Fluctuations in this temperature will have an effect on the reactivity and thus the power of the reactor, which is undesirable. The hot side flow rate (F_{hi2}) or the cold side flow rate (F_{ci2}) is used as the manipulated variable. The load variables include the hot and cold inlet temperatures (T_{hi2}, T_{ci2}) and the flow rate that is not the manipulated variable (F_{ci2} or F_{hi2}). It is important to note that if F_{ci2} is the manipulated variable of the IHX, F_{ci} must be the manipulated variable for the SHX because F_{ci2} and F_{hi} are the same flow rate.

The controlled variable for the reactor was the neutron density (n) which is proportional to reactor power. The neutron density is controlled by manipulating the reactivity with control rod movement (ρ_{rod}). The load variable of the reactor are the coolant mass flow rate (F_c), the reactor inlet temperature (T_i), the reactor outlet temperature (T_e), and the fuel temperature (T_f). Table 4.2 shows the controlled, manipulated, and load variables for each of the units in the system.

Table 4.2. Summary of controlled, manipulated and load variables.

Process Unit	Controlled Variable	Manipulated Variable	Load Variables
SHX	T_{co}	F_{hi} or F_{ci}	F_{ci} or F_{hi}, T_{ci}, T_{hi}
IHX	T_{ho2}	F_{hi2} or F_{ci2}	F_{ci2} or F_{hi2}, T_{ci2}, T_{hi2}
Reactor	n	ρ_{rod}	F_c, T_i, T_e, T_f

4.3.2 Block Diagrams

Control block diagrams were created to represent the control strategy for each heat exchanger. Figures 4.4 and 4.5 show the block diagrams for the SHX and IHX, respectively. Each block in these figures represents a transfer function which relates the variables entering and leaving the block. Each variable within the block is expressed as the deviation from the steady state values of that particular parameter. For example, the topmost block in Figure 4.4 relates the deviation in the cold stream outlet temperature (ΔT_{co}) from its steady state value to the deviation in the temperature of the hot inlet stream (ΔT_{hi}) from its steady state value. These two deviations are related by the transfer function G_{S4}. The asterisk on a variable (for example, ΔT_{co}*) indicates a set-point value which is 0. Both the block diagrams are structured identically, differing only in the controlled and manipulated variables, and the transfer functions. For each diagram G_c is the controller transfer function, G_v is the valve or pump transfer function and G_S/G_I are the process transfer functions for the SHX and IHX, respectively.

The process transfer functions (G_S/G_I) represent the mathematical relationships between the controlled variables and the manipulated variable or load variables. Referring to Figure 4.4, the transfer functions G_{S2}, G_{S3} and G_{S4} represent the transfer functions which effectively convert the deviations (or disturbances) in the load variables F_{ci}, T_{ci} and T_{hi}, respectively, to the deviation in the controlled variable T_{co}. G_{S1} is the transfer function between the controlled (T_{co}) and the manipulated variable (F_{hi}). All the deviations are summed up at the summation point at the right end of the figure, and total deviation is compared to the set-point at the summation junction at the left end of the figure. The error signal (E1) generated is sent to the controller (G_{cS}). Depending on the error and the controller algorithm, the controller sends an output signal (P1) to the valve transfer function block. The manipulated variable F_{hi} is changed based on the valve transfer function (G_{vS}), to keep the controlled variable at its desired value.

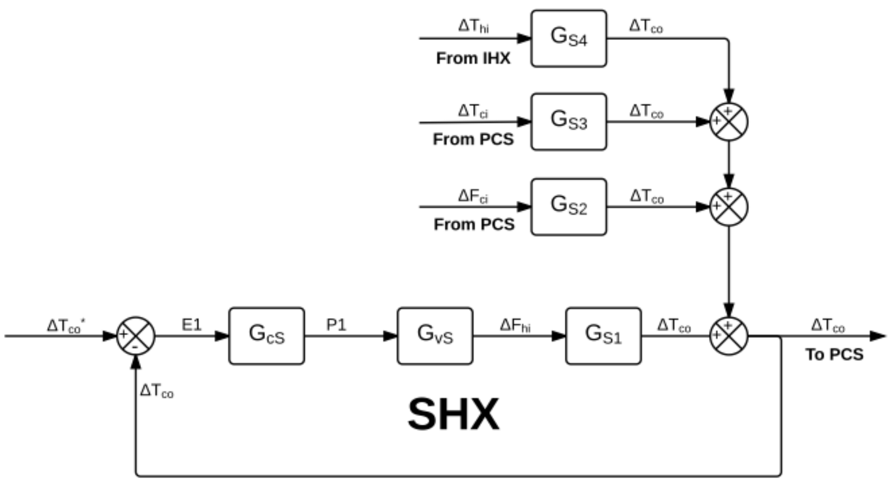

Figure 4.4. Block diagram for SHX control.

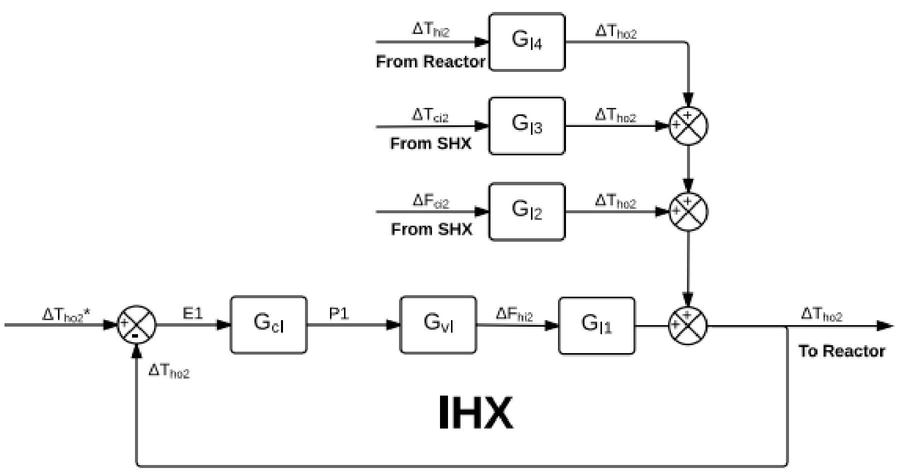

Figure 4.5. Block diagram for IHX control.

The transfer function for the controller is shown in Eq. 4.1. It is the characteristic equation for a PID controller, with a proportional, integral, and derivative gain value to control precisely the system based on a given error value.

$$G_c = K_P + K_I \frac{1}{s} + K_D s \qquad (4.1)$$

The transfer function for the valve or pump is shown in Eq. 4.2. This function has a gain value (K_v), which is just set to 1, and a time constant (τ_v) which determines the time it takes the pump to adjust. This is taken to be 0.05 seconds, which is a near instantaneous response.

$$G_v = \frac{F(s)}{P(s)} = \frac{K_v}{\tau_v s + 1} \qquad (4.2)$$

Eqs. 4.3-4.6 show transfer functions for the SHX relating to changes in the cold outlet temperatures based on changes of the other variables. The gain value (K) relates how outlet temperature, in this case the cold side, changes from the initial steady state value with changes in either the manipulated variable or load variables. For example, K_{cFh} is ~1.5 °C/(kg/s) meaning that if the hot side flow rate changes by 1 kg/s the cold side outlet temperature will change by 1.5 °C. The time constant (*T*) determines the time it takes for the heat transfer. In Eq. 4.4 there is an extra variable, τ_c, which is a time delay term for the cold side of the SHX. This exists because changes in the cold inlet temperature will not immediately effect the cold outlet temperature. There is a certain amount of time it takes for the coolant to travel through the heat exchanger. Until this occurs effects from changes in the cold inlet temperature will not be seen. Equations for the IHX are identical to those for SHX. The only difference are different gain values and time constants.

$$G_{S1} = \frac{\Delta T_{co}}{\Delta F_{hi}} = \frac{K_{cFh}}{T_c s+1} \tag{4.3}$$

$$G_{S2} = \frac{\Delta T_{co}}{\Delta F_{ci}} = \frac{K_{cFc}}{T_c s+1} \tag{4.4}$$

$$G_{S3} = \frac{\Delta T_{co}}{\Delta T_{ci}} = \frac{K_{ctc} e^{-\tau_c s}}{T_c s+1} \tag{4.5}$$

$$G_{S4} = \frac{\Delta T_{co}}{\Delta T_{hi}} = \frac{K_{cth}}{T_c s+1} \tag{4.6}$$

4.3.3 Controller Development

The gain, time constant and time delay values in the transfer functions described above were determined by coolant properties and the system geometry. A built-in MATLAB function called *pidtool* was used for specifying the gain and time constants in the characteristic equation for the controller order to do this. This function opens a PID tuner graphical user interface (GUI) and chooses proportional, integral, and derivative gain values for the system. The equation used for tuning must first be determined. In this case for each exchanger this will be the valve transfer function (G_v) multiplied by the transfer function that relates how the controlled variable changes with variation of the manipulated variable (G_{S1}/G_{I1}). Eq. 4.7 and 4.8 shows the transfer functions used to tune the controllers for the SHX and IHX, respectively. Tables 4.3 and 4.4 show the tuned controller for P, PI, and PID options. These are tuned parameters when both hot side flow rates are being used as the manipulated variables. If the cold side flow rates are used as manipulated variables, two different controller settings must be used. Eq. 4.9 and 4.10 are used for tuning in that case and the resulting controller parameters are shown in Table 4.5, which also shows the controller parameters for controlling the neutron density (n) by manipulating the control rods (ρ_{rod}).

$$G_{vS} G_{S1} = \frac{1}{0.05s+1} * \frac{K_{cFh}}{T_c s+1} \tag{4.7}$$

$$G_{vI}G_{I1} = \frac{1}{0.05s+1} * \frac{K_{hFh2}}{T_{h2}s+1} \tag{4.8}$$

Table 4.3. **SHX controller tuned parameters (Hot side flow rate).**

Controller	K_P (ºC*s/kg)	K_I (ºC*s/kg)	K_D (ºC*s/kg)
P	10.712		
PI	0.7994	0.7680	
PID	0.7976	0.9683	0.1643

Table 4.4. **IHX controller tuned parameters (Hot side flow rate).**

Controller	K_P (ºC*s/kg)	K_I (ºC*s/kg)	K_D (ºC*s/kg)
P	14.236		
PI	0.4296	0.2054	
PID	0.6163	0.3821	0.2353

$$G_{vS}G_{S2} = \frac{1}{0.05s+1} * \frac{K_{cFc}}{T_c s+1} \tag{4.9}$$

$$G_{vI}G_{I2} = \frac{1}{0.05s+1} * \frac{K_{hFc2}}{T_{h2}s+1} \tag{4.10}$$

Table 4.5. **PID controller parameters for IHX, SHX (Cold side flow rates) and reactor.**

HX	K_P (ºC*s/kg)	K_I (ºC*s/kg)	K_D (ºC*s/kg)
SHX	-0.1695	-0.2057	-0.0349
IHX	-0.6985	-0.4331	-0.2666
Reactor	0.461	0.621	0.0329

4.3.4 System Disturbances

Table 4.6 shows a list of possible disturbances that could occur in the system. These include small or large loss of coolant accidents (LOCA), pump malfunction, process problems causing changes in heat removal, or control rod malfunctions in the nuclear reactor. A small LOCA is defined as a pipe break in which the reactor remains pressurized. This is considered to be a break of up to 12 cm in the primary loop but can vary depending on the system. A large LOCA can be a rupture of a pipe connected to the circulating pump with the reactor vessel. The effect of the large LOCA will depend on the system as well (Ragheb, 2013). Each has an effect on the system parameters and can be small or large depending on the severity. Table 6 shows how each disturbance would affect each loop in the AHTR system as well as the reactor. For example, a small LOCA in the process loop, seen as the top example of Table 4.6, would cause the helium flow rate to decrease slightly. That would cause an increase in the temperatures of FLiNaK and FLiBe in the secondary and primary loops, respectively. Due to negative reactivity effects an increase in FLiBe temperature entering the reactor would cause a decrease in the power output of the reactor.

Table 4.6. Possible disturbances and their effects on the system.

Disturbance	Process Effect	Secondary Effect	Primary Effect	Reactor Effect
1. Small LOCA in process loop	Lower helium flowrate (T ↑)	Higher FLiNaK temperature	Higher FLiBe temperature	Lower reactor duty
2. Large LOCA in process loop	Much Lower helium flowrate (T ↑)	Much Higher FLiNaK temperature	Much Higher FLiBe temperature	Much Lower reactor duty
3. Small LOCA in secondary loop	Lower helium temperature	Lower secondary flowrate	Higher FLiBe temperature	Lower reactor duty
4. Large LOCA in secondary loop	Much Lower helium temperature	Much Lower secondary flowrate	Much Higher FLiBe temperature	Much Lower reactor duty
5. Small LOCA in primary loop	Lower helium temperature	Lower FLiNaK temperature	Lower primary flowrate	Lower/higher reactor duty
6. Large LOCA in primary loop	Much Lower helium temperature	Much Lower FLiNaK temperature	Much Lower primary flowrate	Much Lower reactor duty
7. Process pump malfunction(2)	Higher helium flowrate (T ↓)	Lower FLiNaK temperature	Lower FLiBe temperature	Higher reactor duty
8. Secondary pump malfunction(2)	Higher helium temperature	Higher secondary flowrate	Lower FLiBe temperature	Higher reactor duty
9. Primary pump malfunction(2)	Higher helium temperature	Higher FLiNaK temperature	Higher primary flowrate	Lower/higher reactor duty
10. Lower process heat removal	Higher helium temperature	Higher FLiNaK temperature	Higher FLiBe temperature	Lower reactor duty
11. Higher process heat removal	Lower helium temperature	Lower FLiNaK temperature	Lower FLiBe temperature	Lower reactor duty
12. Control rod malfunction(ρ_{rod} ↑)	Higher helium temperature	Higher FLiNaK temperature	Higher FLiBe temperature	Initial higher reactor duty.
13. Control rod malfunction(ρ_{rod} ↓)	Lower helium temperature	Lower FLiNaK temperature	Lower FLiBe temperature	Initial lower reactor duty

4.4 System Models and Simulation Technique

4.4.1 Governing Equations for Heat Exchangers

The representative governing equations for a heat exchanger were obtained by the energy balance and are shown Eqs. 4.11-4.13. Eq. 4.11 is the energy balance for the hot stream, Eq. 4.12 is the energy balance for the cold stream, and Eq. 4.13 represents the energy balance for the wall separating the two streams, written for a differential element of the heat exchanger.

$$m_h C_{ph} \frac{dT_h}{dt} + F_h C_{ph}(T_{ho} - T_{hi}) = (hA)_h (T_w - T_h) \tag{4.11}$$

$$m_c C_{pc} \frac{dT_c}{dt} + F_c C_{pc}(T_{co} - T_{ci}) = (hA)_c (T_w - T_c) \tag{4.12}$$

$$m_w C_{pw} \frac{dT_w}{dt} = (hA)_h(T_h - T_w) - (hA)_c(T_w - T_c) \tag{4.13}$$

Where *m* is the mass of the fluid or metal in the element, C_p is the heat capacity of the fluid or metal, $\frac{dT}{dt}$ is the rate of change in temperature over time, *h* is the heat transfer coefficient, *A* is the heat transfer area, and *F* is the flow rate. The subscripts *h, c, w, i,* and *o* stand for hot, cold, wall, inlet, and outlet, respectively. The first term in each of the equations is the energy accumulation term, which would be zero at steady state. The second term in Eqs. 4.11 and 4.12 represents the difference in the energy of the fluid leaving and entering the element by convection. The terms on the right hand side of the equations represent the convective heat transfer between the fluid and the wall. The energy balance for the wall does not involve the convective flow term, but has two heat transfer terms representing convective heat transfer from the hot fluid to the wall and wall to cold fluid. Both IHX and SHX have a similar set of three equations, with the parameter values that correspond to the properties of the respective streams. Each heat exchanger was discretized and a hot temperature, cold temperature, and wall temperature obtained at each node. The node was defined by the uniformity of each temperature at the node (no spatial variation within the node).

4.4.2 Governing Equations for Reactor

The reactor dynamics is described by a series of differential equations that include the neutronics equations with one to six groups of delayed neutrons, as well as energy balances for the fuel, and coolant. In this work the equations based off a paper by Das et al. (2013) were used, and are reproduced below (Eqs. 4.14-4.18).

Eq. 4.14 is for the dynamic neutron density balance,

$$\frac{dn}{dt} = \frac{\rho - \beta}{\Lambda} n + \sum_{i=1}^{G} \lambda_i c_i \tag{4.14}$$

Where *n* is the neutron density, ρ is the reactivity (0 at steady-state), β is the delay neutron fraction, Λ is the prompt neutron lifetime, λ_i is the decay constant for group *i*, and c_i is the precursor concentration for group *i*. There are up to 6 different precursors. These are the groups that do not emit neutrons instantaneously and only account for a small fraction of the fission products.

The precursor balance is shown by Eq. 4.15.

$$\frac{dc_i}{dt} = \frac{\beta_i}{\Lambda} n - \lambda_i c_i \quad \textit{for } i=1,2,\ldots,G \tag{4.15}$$

Where β_i is the delay neutron fraction for delay neutron group *i*, and G is the number of delay groups. The delay fraction, β from Eq. 4.14, is the summation of all delay neutron fractions, β_i, and is equal to 0.006502 in all cases. This is the delay neutron fraction for U-235 which is the fuel used in the

AHTR. There can be 1 to 6 equations for precursor concentrations depending on how many delay groups is chosen to be used. For example, if 3 groups are chosen, 3 differential equations for the precursor concentration would be necessary.

Eq. 4.16 shows the energy balance for the fuel within the reactor.

$$\frac{dT_f}{dt} = \frac{P}{\mu_f} n - \frac{\Omega}{\mu_f} T_f + \frac{\Omega}{2\mu_f} T_i + \frac{\Omega}{2\mu_f} T_e \tag{4.16}$$

T is the temperature where subscripts, f, i, and e are for fuel, inlet, and exit, respectively. P is the power of the reactor, Ω is the product of the heat transfer area, A, and the heat transfer coefficient, h, and μ_f is defined as the mass of fuel in the reactor, m_f, times the heat capacity of the fuel, C_{pf}. The final differential equation is for an energy balance for the coolant, similar in form to the energy balance for the fuel, and is shown below,

$$\frac{dT_e}{dt} = \frac{2\Omega}{\mu_c} T_f - \left(\frac{2M_c+\Omega}{\mu_c}\right) T_e + \left(\frac{2M_c-\Omega}{\mu_c}\right) T_i \tag{4.17}$$

The variables are similar, with the addition of M_c which is the product of the coolant mass flow rate, F_c, and the coolant heat capacity, C_{pc}. μ_c is defined as the mass of coolant in the reactor, m_c, times the heat capacity of the coolant, C_{pc}. These differential equations are solved simultaneously to find the values of the dependent variables at each time interval.

In addition, an equation for the reactivity is used which incorporates temperature feedback due to changes in inlet and outlet temperatures. This equation determines the reactivity that is used in Eq. 4.14.

$$\rho = \rho_{rod} + \alpha_f\left(T_f - T_{f0}\right) + \frac{\alpha_c}{2}(T_i - T_{i0}) + \frac{\alpha_c}{2}(T_e - T_{e0}) \tag{4.18}$$

The reactivity is dependent on ρ_{rod}, which is the reactivity change due to movement of control rods. In addition, the temperatures of the fuel and coolant affect reactivity. The change depends on the reactivity co-efficient for the fuel, α_f, and the coolant, α_c. The values of these reactivity coefficients used in this study were -3.85×10^{-5} $^oC^{-1}$ and -0.34×10^{-5} $^oC^{-1}$, respectively (Galvez, 2011). The significance of the negative reactivity coefficients is that if there is a temperature increase entering the reactor, the power of the reactor will decrease. If the power were to increase, the temperatures of the system would increase until reactor failure.

4.4.3 Numerical Solution Technique

The solution for each set of differential equations required a numerical method. The fourth-order Runge-Kutta method was used in this work to solve each set of differential equations simultaneously. The equations required are shown below (Chapra et al., 2010). There will be one set of the following equations for each dependent variable. For each dependent variable values for *a, b, c,* and *d* are solved for at each time step. h is the time step, $f_j(y_1, y_2, ..., y_j)$ is the function of variable j, $y_{j,i}$ is the current value of variable j, and $y_{j,i+1}$ is the next value for variable j. For the IHX and SHX there are 3 dependent variables each (T_h, T_c, T_w) for a total of 6 sets of the equations below. The reactor has from 4 to 9 dependent variable (n, c_1, c_2, c_3, T_f, T_c) depending on the number of delay groups used. This equals a total of 10 to 15 sets of the equations below. In total, 10 to 15 sets of the equations will be solved for each of the time steps.

$$a_{j,i} = f_j(y_{1,i}, y_{2,i}, \ . \ . \ . \ , \ y_{m,i}) \tag{4.19}$$

$$b_{j,i} = f_j((y_{1,i} + {}^{h}/_{2} * a_{1,i}), (\, y_{2,i} + {}^{h}/_{2} * a_{2,i}), \ . \ . \ . \ , (y_{m,i} + {}^{h}/_{2} * a_{m,i}) \tag{4.20}$$

$$c_{j,i} = f_j((y_{1,i} + {}^{h}/_{2} * b_{1,i}), (\, y_{2,i} + {}^{h}/_{2} * b_{2,i}), \ . \ . \ . \ , (y_{m,i} + {}^{h}/_{2} * b_{m,i}) \tag{4.21}$$

$$d_{j,i} = f_j((y_{1,i} + h * c_{1,i}), (\, y_{2,i} + h * c_{2,i}), \ . \ . \ . \ , (y_{m,i} + h * c_{m,i}) \tag{4.22}$$

$$y_{j,i+1} = y_{j,i} + {}^{h}/_{6} \left(a_{j,i} + 2b_{j,i} + 2c_{j,i} + d_{j,i}\right) \tag{4.23}$$

The results from the Runge-Kutta technique were compared and found to be in good agreement with those obtained using a more computational intense technique. All subsequent simulations were therefore then conducted using the Runge-Kutta method.

4.5 Results and Discussion

4.5.1 Controlled response of coupled heat exchangers system

Control of the coupled IHX and SHX (not accounting for the reactor dynamics) was simulated and the results are presented below. The cold outlet temperature of the SHX (T_{ci}) and the hot outlet temperature of the IHX (T_{ho2}) were the controlled variables in each of the cases shown in this section.

4.5.1.1 Process Loop Disturbances

Figure 4.6 shows the controller system response after a +10 ^oC step change in the temperature of the stream entering the cold side of the SHX (T_{ci}). Figures 4.6a and 4.6d show the time profiles for the controlled variables for the SHX (T_{co}) and IHX (T_{ho2}), respectively. As can be seen these two temperatures are successfully controlled around their set-point values. Figure 4.6e shows the change in the manipulated variables (F_{hi}/F_{hi2}) as a function of time. An increase in the inlet temperature of the cold stream implies a lower heat duty requirement in the heat exchanger when the outlet temperature of that stream is controlled. This lower heat duty is achieved by decreasing the flow rate of the stream on the hot side of the heat exchanger. The hot side flow rates for the IHX (F_{hi2}) and SHX (F_{hi}) shown in Figure 4.6e change by -6.5% and -5.0%, respectively. Figures 4.6b and 4.6c show the increase in the uncontrolled variables for the SHX (T_{ho}) and the IHX (T_{co2}), respectively. The hot side outlet temperature of the SHX (T_{ho}) increases by 3.5 ^oC and the cold side outlet temperature of the IHX (T_{co2}) increases by a little more than 1 ^oC. After the disturbance occurs, it takes the system about 400 seconds to come to a controlled equilibrium at a new steady state. Due to the drop in the flow rates the duty of the heat exchangers drop to about 9350 kW, which is ~6.5% less than the initial duty of 10 MW as shown in Figure 4.6f.

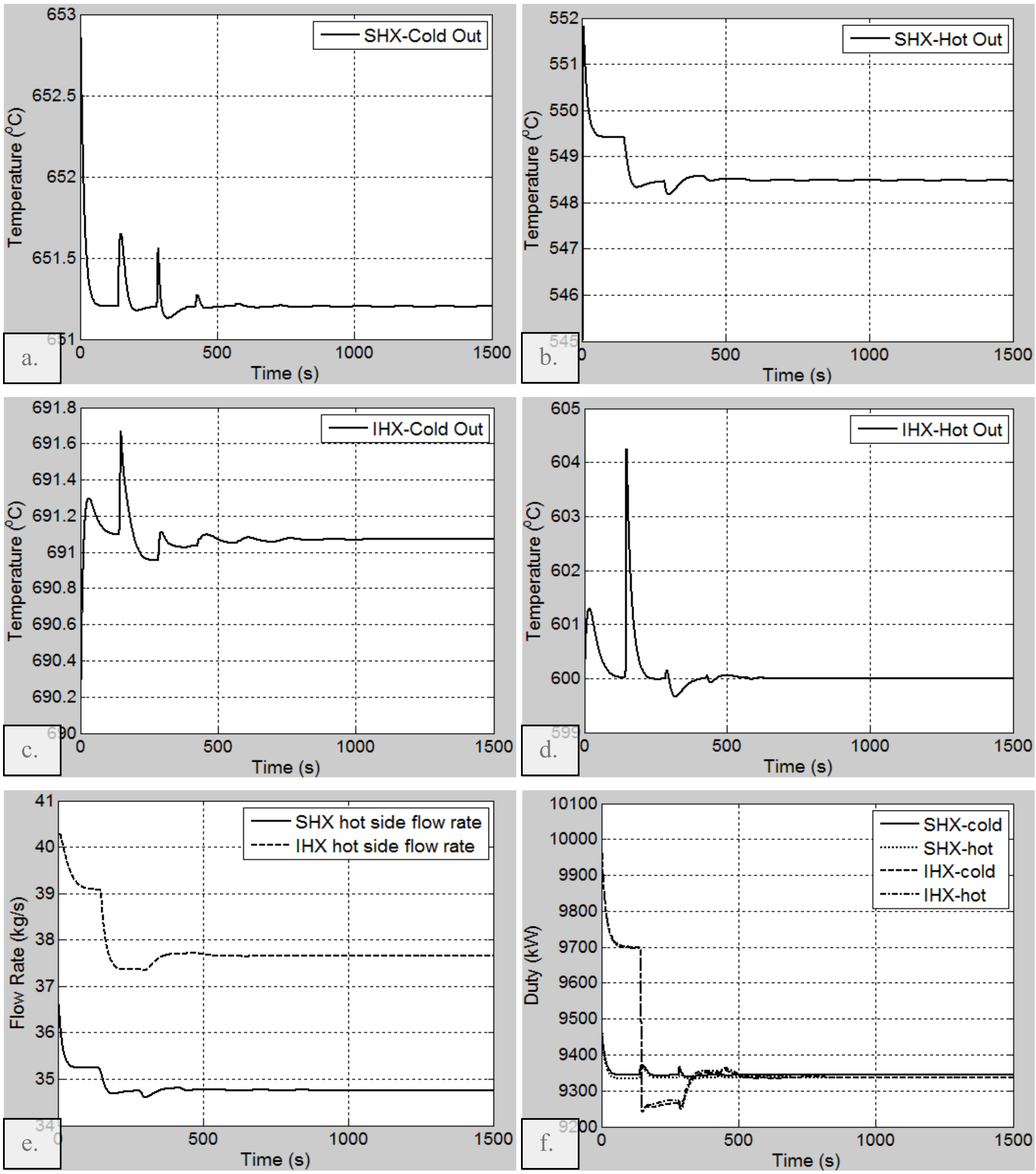

Figure 4.6. Control of IHX and SHX after +10 ºC step change entering the cold side of the SHX. a: SHX cold outlet temperature, b: SHX hot outlet temperature, c: IHX cold outlet temperature, d: IHX hot side outlet temperature, e: hot side flow rates of SHX and IHX, f: Duties of the hot and cold side of SHX and IHX.

Figure 4.7 shows the system response for the control of the IHX and SHX after a -10 ^{o}C step change in the temperature of the stream entering the cold side of the SHX (T_{ci}). Figures 4.7a and 4.7d show the response as a function of time for the controlled variables for the SHX (T_{co}) and IHX (T_{ho2}), respectively. As before, these variables are controlled successfully around their set-point values by manipulating the hot side flow rates. In this case, the increased heat duty requires increasing the flow rates of the streams on the hot side of the heat exchangers. The change in the hot side flow rates for the IHX (F_{hi2}) and SHX (F_{hi}) are 6.7% and 6.8%, respectively as seen in Figure 4.7e. Figures 4.7b and 4.7c show the uncontrolled variables for the SHX (T_{ho}) and IHX (T_{co2}) and they are seen to decrease. The hot side outlet temperature of the SHX (T_{ho}) decreases by ~1.4 ^{o}C and the cold side outlet temperature of the IHX (T_{co2}) decreases by ~1.7 ^{o}C. After the disturbance occurs, it takes the system about 700 seconds to come to a controlled equilibrium. Due to the increase in the flow rates, the duty of the heat exchangers rises to about 10650 kW, which is about 6.5% higher than the initial duty as shown in Figure 4.7f.

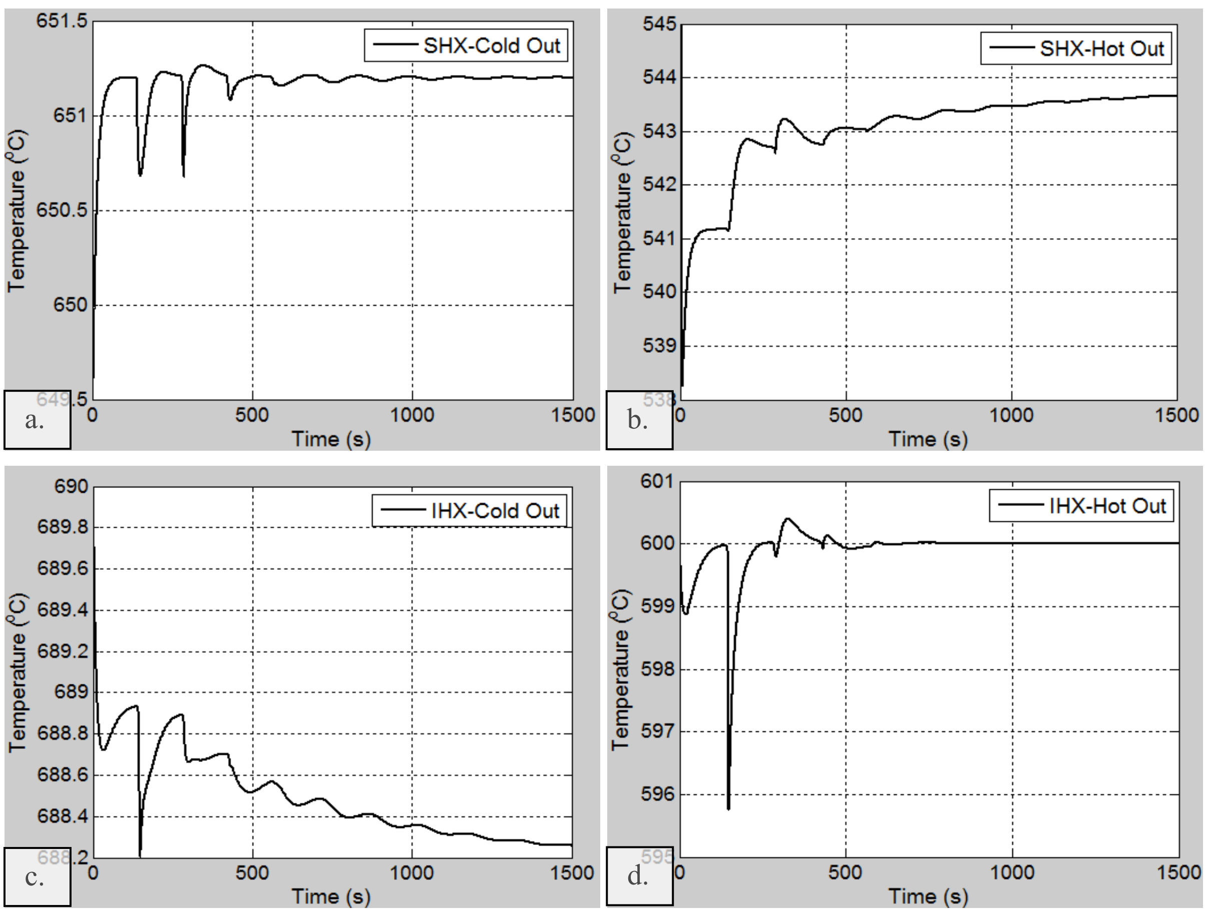

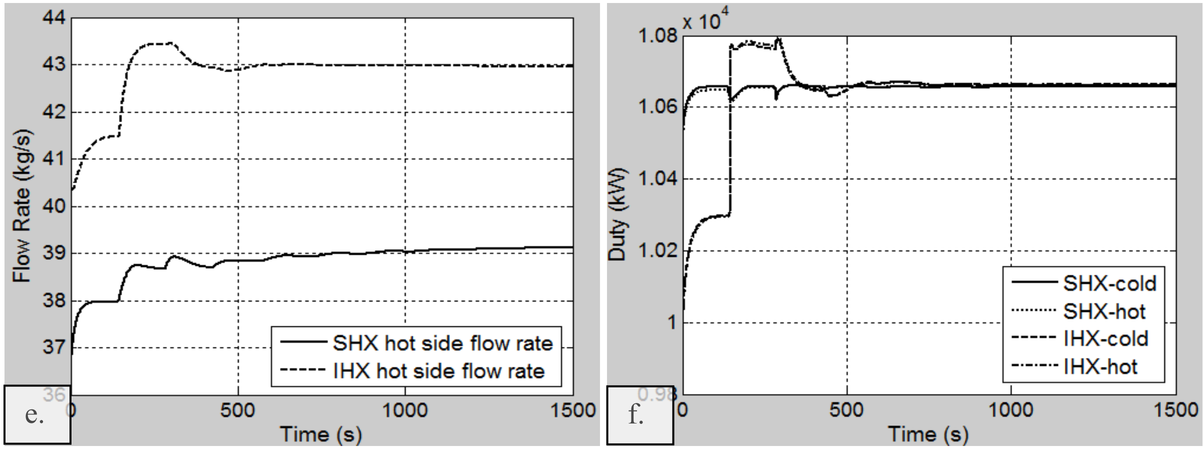

Figure 4.7. Control of IHX and SHX after -10 ºC step change entering the cold side of the SHX. a: SHX cold outlet temperature, b: SHX hot outlet temperature, c: IHX cold outlet temperature, d: IHX hot side outlet temperature, e: hot side flow rates of SHX and IHX, f: Duties of the hot and cold side of SHX and IHX.

4.5.1.2 Primary Loop Disturbances

Figure 4.8 shows the system control after a -10 ºC step change in the temperature of the stream entering the hot side of the IHX (T_{hi2}). To look at other manipulated variable options, the cold side flow rates are used as the manipulated variables rather than the hot side flow rates. The controlled variables for the SHX (T_{co}) and IHX (T_{ho2}) are unchanged, as shown in Figures 4.8a and 4.8d. The decrease in the temperature of the hot stream entering the heat exchanger implies lowering the amount of heat transferred to the cold stream. In order to maintain a constant outlet temperature of the hot stream, the cold side flow rates are decreased. The cold side flow rates of the IHX (F_{ci2}) and SHX (F_{ci}) shown in Figure 4.8e decrease by 6.3% and 9.5%, respectively. Figures 4.8b and 4.8c show the uncontrolled variables for the SHX (T_{ho}) and IHX (T_{co2}), respectively. Both of these temperatures decrease, with the decrease being more severe for the temperature of the cold outlet stream (T_{co2}) of the IHX. It decreases by ~7 ºC and the temperature of the hot outlet stream of the SHX (T_{ho}) decreases by ~1ºC. The system exhibits oscillatory behavior, stabilizing at a new equilibrium in ~1000 seconds. The thermal duty decreases to about 9000 kW, 10% lower than the initial duty as seen in Figure 4.8f.

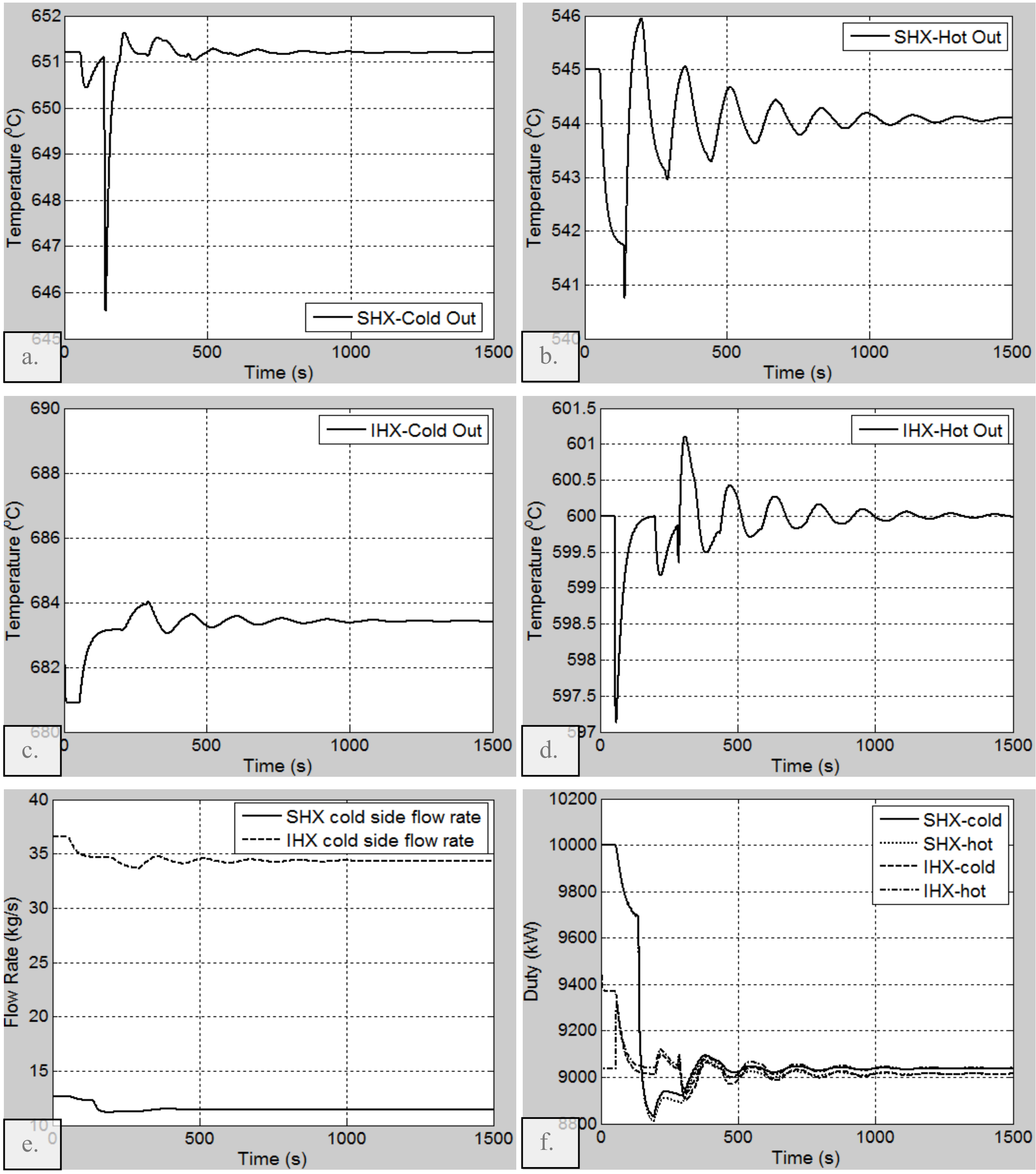

Figure 4.8. Control of IHX and SHX after -10 ºC step change entering the hot side of the IHX. a: SHX cold outlet temperature, b: SHX hot outlet temperature, c: IHX cold outlet temperature, d: IHX hot side outlet temperature, e: cold side flow rates of SHX and IHX, f: Duties of the hot and cold side of SHX and IHX.

Figure 4.9 shows the system control after a +10 ºC step change in the temperature of the stream entering the hot side of the IHX (T_{hi2}). Again, the cold side flow rates are used as the manipulated variables rather than the hot side flow rates. Figures 4.9a and 4.9d show the time profiles of the controlled variables for the SHX (T_{co}) and IHX (T_{ho2}), respectively. After the disturbance, the temperatures are controlled at their desired values by changing the cold side flow rates(F_{ci}/F_{ci2}). The system exhibits oscillatory behavior. The initial drop in the cold outlet temperature is compensated by increasing the flow rate as seen in Figure 4.9e. This causes the temperature rise across the SHX to decrease and thus keeps the temperature at its desired value. The hot outlet temperature of the IHX (T_{ho2}) also rises initially. The cold side flow rate increases in order to make the heat transfer greater and increase the temperature drop across the hot side. The cold side flow rates of the IHX (F_{ci2}) and SHX (F_{ci}) rise by 8.5% and 10.3% respectively. Figures 4.9b and 4.9c show the uncontrolled variables for the SHX (T_{ho}) and IHX (T_{co2}), respectively. Both temperatures increase, with the increase being slightly greater for the cold outlet stream of the IHX. The cold outlet of the IHX (T_{co2}) rises by about 4.5 ºC and the hot outlet of the SHX (T_{ho}) rises by about 3.2ºC. A new equilibrium is established in ~800 seconds and the duty rises to about 11000 kW, 10% higher than the initial value as seen in Figure 4.9f.

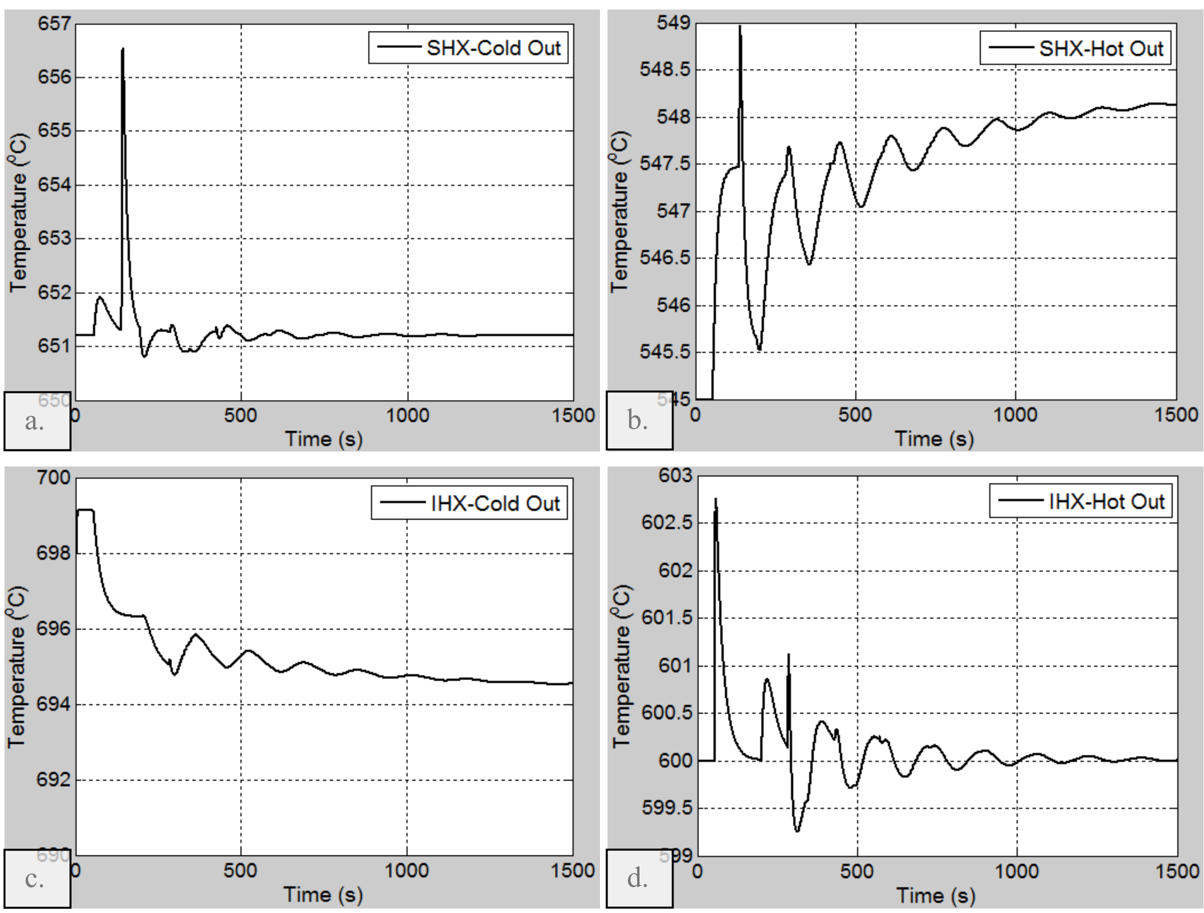

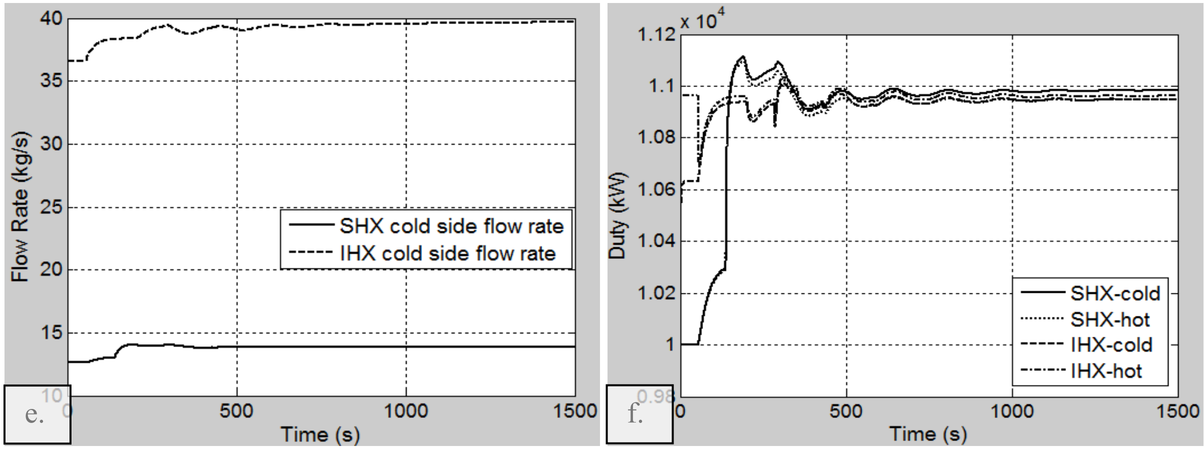

Figure 4.9. Control of IHX and SHX after +10 ºC step change entering the hot side of the IHX. a: SHX cold outlet temperature, b: SHX hot outlet temperature, c: IHX cold outlet temperature, d: IHX hot side outlet temperature, e: cold side flow rates of SHX and IHX, f: Duties of the hot and cold side of SHX and IHX.

4.5.1.3 Alternative Control Method

Larger disturbances in load variables require progressively larger adjustments in the manipulated variables for system control. However, the range of a manipulated variable may be subject to other constraints arising from limitations in other components of the system. For example, the pump capacity may limit the maximum flow rate of a manipulated variable. The flow rate may also be constrained by a limit on the acceptable pressure drop. Conversely, a minimum limit may be specified on the flow rate, arising from the equipment constraints. In such cases where the system disturbances result in reaching limiting condition of a manipulated variable, the control system design must provide for switching to using another combination of manipulated variables for further control. In the present work, the limits of manipulated variables are specified at ±20% of its initial flow rates. Once a manipulated variable reaches its limit, further control requires manipulation of another variable. Figure 4.10 shows the controller system response after a -22 ºC step decrease in the temperature of the stream entering the cold side of the SHX (T_{ci}). Figures 4.10a and 4.10d show the controlled variables for the SHX (T_{co}) and IHX (T_{ho2}), respectively. Both the controlled temperatures show an immediate decrease after the disturbance is introduced. Both the manipulated variables – the SHX the hot side flow rate (F_{hi}) and the hot side flow rate of the IHX (F_{hi2}) – increase in response, causing the controlled temperatures to increase to their set points. Figures 4.10b and 4.10c show the uncontrolled variables for the SHX (T_{ho}) and IHX (T_{co2}). The hot side outlet temperature of the SHX (T_{ho}) decreases by about 15 ºC initially before rising to a temperature of 547 ºC, which is 2 ºC higher than the initial value. The cold outlet temperature of the IHX (T_{co2}) drops by about 6 ºC. At about 650 seconds the hot side flow rate of the SHX reaches the limit (120% of initial flow) as seen in Figure 4.10f. At this point the system switches to using the cold side flow rate of the SHX (F_{ci}) as the manipulated variable, as seen in Figure 4.10g. The hot side flow rate of the IHX seen in Figure 10e never reaches the limit and is used as the manipulated variable for the IHX for the entirety of the control. This flow rate increases by about 13%. The hot and cold side flow rates of the SHX change by +20% and -1%, respectively. The system takes around 1100 seconds to come to equilibrium and the duty increases by around 13% to ~11300 kW as shown in Figure 4.10h.

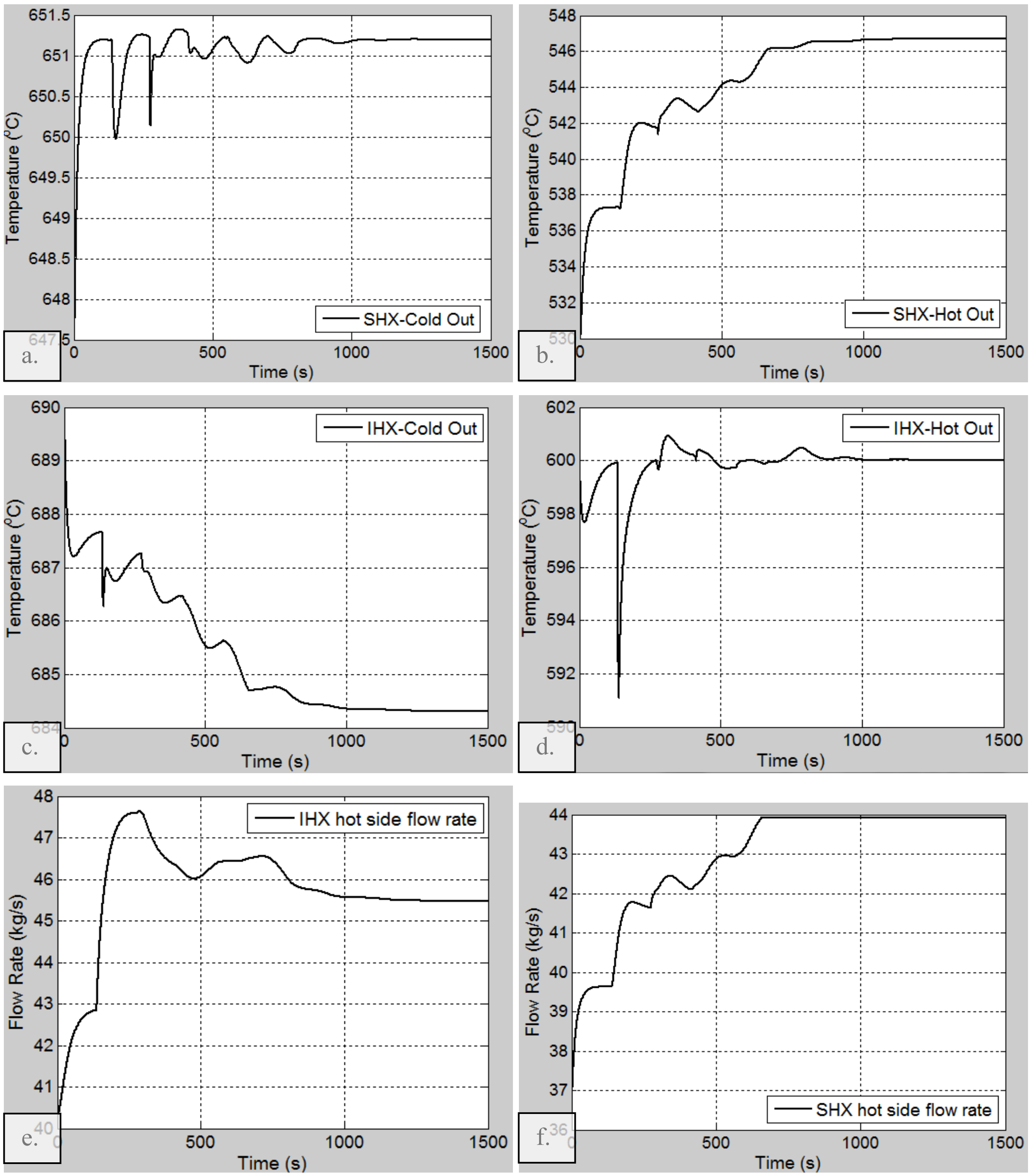

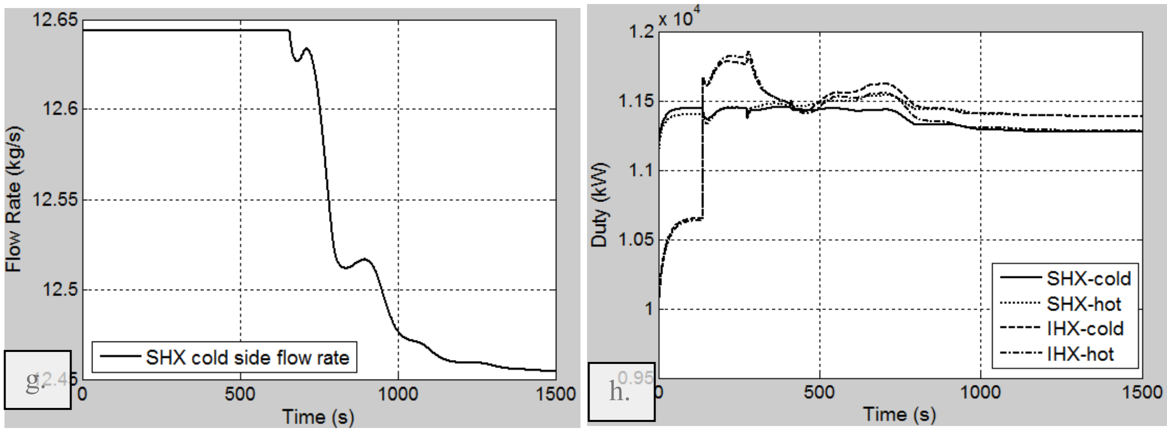

Figure 4.10. Control of IHX and SHX with changing manipulated variables after -22 ºC step change entering the cold side of the SHX. a: SHX cold outlet temperature, b: SHX hot outlet temperature, c: IHX cold outlet temperature, d: IHX hot side outlet temperature, e: hot side flow rate IHX, f: hot side flow rate of SHX, g: cold side flow rate of SHX, h: Duties of the hot and cold side of SHX and IHX.

Figure 4.11 shows the system response to a +30 ºC step increase in the temperature of the stream entering the cold side of the SHX (T_{ci}). Figures 4.11a and 4.11d are the controlled variables for the SHX (T_{co}) and IHX (T_{ho2}), respectively. As shown, both the temperatures spike immediately after the disturbance. The manipulated variables – the hot side flow rate of SHX (F_{hi}) and the hot side flow rate of IHX (F_{hi2}) – decrease in response. Figures 4.11b and 4.11c show the uncontrolled temperatures for the SHX (T_{ho}) and IHX (T_{co2}), respectively. The hot outlet temperature of the SHX (T_{ho}) increases by ~14 ºC. After an initial increase of roughly 3.6 ºC, the temperature of cold outlet stream of the IHX (T_{co2}) stabilizes at a temperature 2.5 ºC higher than the initial value. Again, the manipulated variables are changed once a flow rate has reached the constraint of a change of ±20% in the initial value. In this scenario, the hot side flow rate of the IHX reaches this limit first (80%) at approximately 150 seconds as seen in Figure 4.11e. At this time, the IHX switches to using the cold side flow rate (F_{ci2}) as the manipulated variable. This is the same variable as the hot side flow rate of the SHX (F_{hi}) and thus the SHX must also switch to using the cold side flow rate (F_{ci}) because both controllers can not use the same manipulated variable. Figure 4.11f shows the IHX cold side (SHX hot side) flow rate. It decreases by ~16.4% during the initial phase of control when employed for the control of the SHX, but then increases by 2.5% when it is switched to control the IHX. The overall change in the flow rate of this stream is -13.9%. The cold side flow rate of the SHX, seen in Figure 4.11g, has an initial spike but eventually decreases by 0.4%. The system is in equilibrium at ~700 seconds after the disturbance is introduced, with a decrease in the thermal duty of ~2000 kW or -20% of the initial duty as seen in Figure 4.11h.

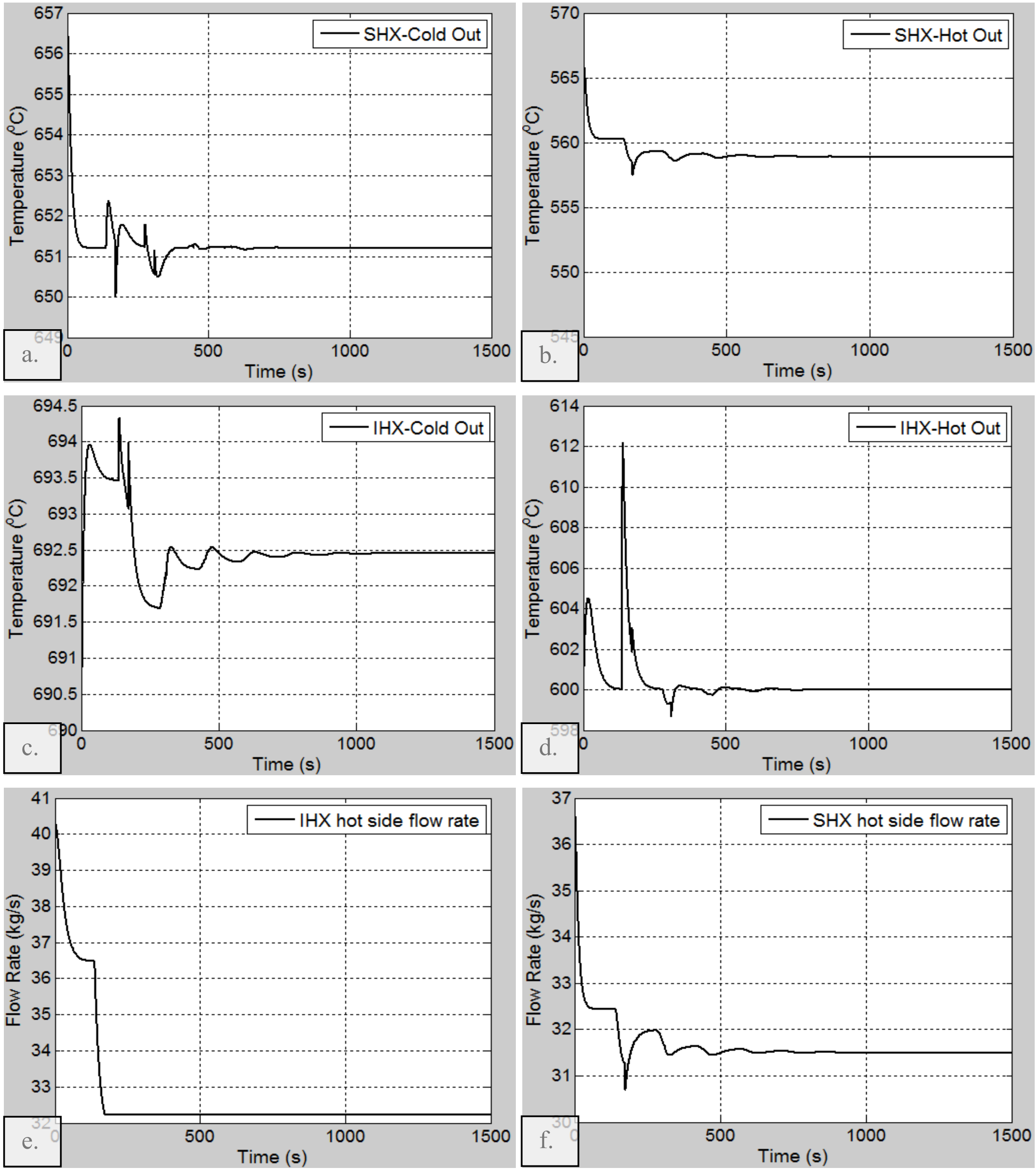
SHX-Cold Out
SHX-Hot Out
IHX-Cold Out
IHX-Hot Out
IHX hot side flow rate
SHX hot side flow rate
Temperature (°C)
Flow Rate (kg/s)
Time (s)
a.
b.
c.
d.
e.
f.

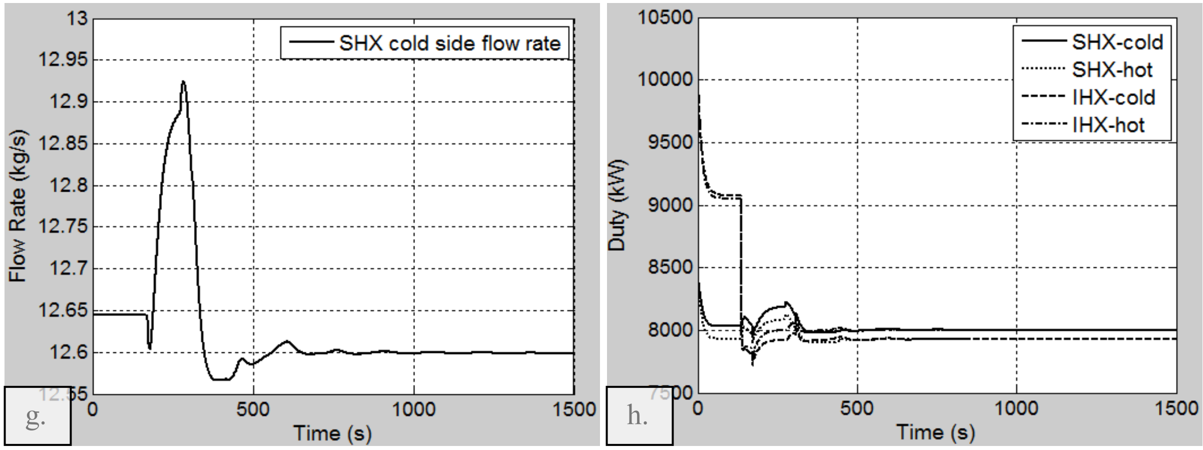

Figure 4.11. Control of IHX and SHX with changing manipulated variables after +30 ºC step change entering the cold side of the SHX. a: SHX cold outlet temperature, b: SHX hot outlet temperature, c: IHX cold outlet temperature, d: IHX hot side outlet temperature, e: hot side flow rate IHX, f: hot side flow rate of SHX, g: cold side flow rate of SHX, h: Duties of the hot and cold side of SHX and IHX.

4.5.1.4 Summary of Control Results

The control system response to various disturbances is summarized in Table 4.7. As seen from the table, the system is able to establish a new steady state for step temperature disturbances in the process and primary streams.

Other potential system disturbances involve changes in flow rates of various streams, arising from leakages or breakages in the piping system or a pump malfunction, etc. The control system described above does not include the dynamics of the nuclear reactor and its control. The next section describes the control system response incorporating the flow disturbances and the reactor dynamics along with feedback effects.

Table 4.7. **Summary of control results for different disturbances**

Loop	Disturbance	SHX flow rate change %	IHX flow rate change %	Change in Thermal Duty kW
		Temperature Disturbances		
Process	-10 ºC	F_{hi}= +6.8%	F_{hi2}= +6.7%	+650 (+6.5%)
	+10 ºC	F_{hi}= -5.0%	F_{hi2}= -6.5%	-650 (-6.5%)
	-22 ºC*	F_{ci}= -1.0% F_{hi}= +20%	F_{hi2}= +13%	+1300 (+13%)
	+30ºC**	F_{ci}= -0.4% F_{hi}= -16.4%	F_{hi2}= -20% F_{ci2}=+2.5%	-2000 (-20%)
Primary	-10 ºC	F_{ci}= -9.5%	F_{ci2}= -6.3%	-1000 (-10%)
	+10 ºC	F_{ci}= +10.3%	F_{ci2}= +8.5%	+1000 (+10%)

*System changes from using F_{hi2}/F_{hi} → F_{hi2}/F_{ci} **System changes from using F_{hi2}/F_{hi} → F_{ci2}/F_{ci}

4.5.2 Controlled response of coupled heat exchangers-reactor system

The reactor model described above was incorporated into the simulations as described below.

4.5.2.1 Optimization of Number of Delayed Neutron Groups

The rigorous reactor model involves using 6 groups of delayed neutrons, which results in the highest accuracy, but also requires increased computational power and time. The delayed neutron groups can be lumped together according to their half-lives creating fewer groups. Table 4.8 shows the neutron fractions and decay constant when 1, 2, 3, or 6 groups of delayed neutrons are considered in the model. The values for the 6 groups were acquired from Lamarsh and Baratta (2001). The β_i values for the situations where delayed neutrons fractions are grouped into 1, 2, and 3 groups are found by summing the β_i values of the fractions in that group. For example, when the fractions are combined into 3 groups, the 3 β_i values are the sum of group 1 and group 2, the sum of group 3 and group 4, and the sum of group 5 and group 6. The λ_i values to be used in the reactor model are found from Eq. 4.24, where the summation is carried over the delayed neutron fractions combined in that group.

$$\lambda_i = \frac{\Sigma \beta_i}{\Sigma \beta_i / \lambda_i} \tag{4.24}$$

Table 4.8. Neutron fraction and decay constant for 1, 2, 3, and 6 groups of delayed neutrons.

<table>
<tr><td></td><td colspan="2">6 Groups</td><td colspan="2">3 Groups</td><td colspan="2">2 Groups</td><td colspan="2">1 Group</td></tr>
<tr><td>Group</td><td>β_i</td><td>λ_i (s^{-1})</td><td>β_i</td><td>λ_i (s^{-1})</td><td>β_i</td><td>λ_i (s^{-1})</td><td>β_i</td><td>λ_i (s^{-1})</td></tr>
<tr><td>1</td><td>0.000215</td><td>0.0124</td><td rowspan="2">0.001639</td><td rowspan="2">0.0256</td><td rowspan="3">0.002913</td><td rowspan="3">0.0386</td><td rowspan="6">0.006502</td><td rowspan="6">0.0767</td></tr>
<tr><td>2</td><td>0.001424</td><td>0.0305</td></tr>
<tr><td>3</td><td>0.001274</td><td>0.111</td><td rowspan="2">0.003842</td><td rowspan="2">0.192</td></tr>
<tr><td>4</td><td>0.002568</td><td>0.301</td><td rowspan="3">0.003589</td><td rowspan="3">0.387</td></tr>
<tr><td>5</td><td>0.000748</td><td>1.14</td><td rowspan="2">0.001021</td><td rowspan="2">1.37</td></tr>
<tr><td>6</td><td>0.000273</td><td>3.01</td></tr>
</table>

Eq. 4.15, in reality, is not a single equation, but represents as many equations as the number of delay groups used. As seen from Table 4.8, there are 6 distinct groups of delayed neutrons, and the greatest accuracy will be obtained by using 6 distinct equations. However, this will result in an increased computation load and complexity in programming as well as an increased possibility of introducing rounding errors in computation. Combining all the distinct delayed neutrons into a single delay group will result in lower computation load and simplified programming, but may introduce inaccuracies in the results. To optimize the number of delay groups to be used in the computations, the 6 delay neutron groups were lumped into 1, 2 and 3 group and the resultant effective neutron fraction and delay constant calculated for each grouping. These values can be seen in Table 4.8. Then the simulations for the 1, 2, and 3 group models were compared to the simulation where all 6 distinct groups were used in the model. A disturbance of -0.2 $ was introduced in the reactor. For each situation the reactor power was found as a function of time. The reactor power error of the 1, 2, and 3 group models from the 6 group model was

then found and is shown in Figure 4.12. The error is defined as the deviation of the results for the 3 different models from the results for the simulation involving 6 groups. The model combining all 6 delay neutrons into a single group of delayed neutrons had the largest error while the model using 3 delayed groups had minimal error. The largest errors were seen during the initial period, with the errors becoming vanishingly small for all combinations at around 600 s. The largest error seen between 1 group and 6 groups was just over 6%, which was the largest error of the 3 models. The 2 delay group model involves a maximum error of just over 2% and with 3 groups the maximum error is roughly 0.5%. For this reason, the delayed neutrons were combined into 3 groups in subsequent simulations as it reduces the computational burden by 50% with respect to Eq. 4.15 while only introducing minor error. With the number of delay groups decided the code can then be developed and simulation of temperature and flow rate disturbances analyzed.

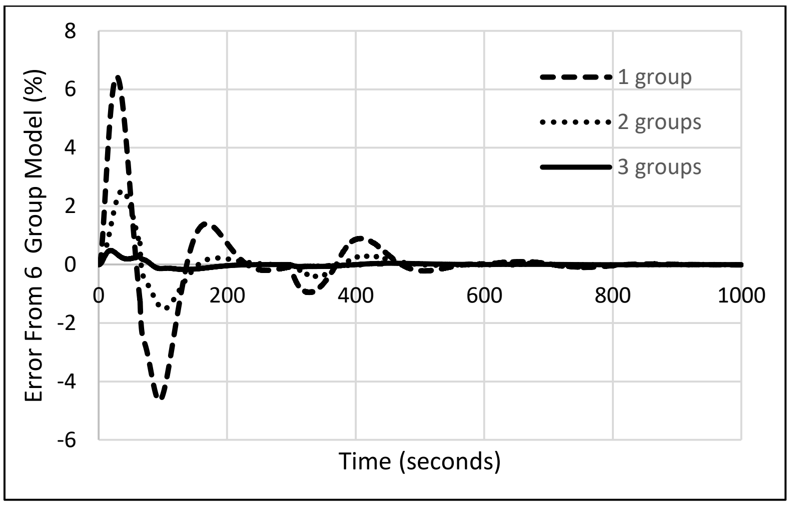

Figure 4.12. Error from model using 6 groups of delayed neutrons.

4.5.2.2 Temperature Disturbances

Figure 4.13 shows the response of the system after a +10 ^oC step increase in the temperature of the stream entering the cold side of the SHX (T_{ci}). Figures 4.13a and 4.13d show the time trajectories of the controlled variables for the SHX (T_{co}) and IHX (T_{ho2}), respectively. As can be seen these figures, the disturbance causes the temperatures to increase initially, followed by the controller action that manages to return the temperatures to their set-point values indicated by the dashed lines. Figures 4.13b and 4.13c, respectively, show the time trajectories of temperatures of other streams of SHX (T_{ho}) and IHX (T_{co2}) that are not controlled. T_{ho} increases by 5.7 ^oC while T_{co2} decreases by ~0.9 ^oC. To counteract the increase in temperature seen in the controlled variables both hot side flow rates (F_{hi}/F_{hi2}) are manipulated, with both the flow rates ultimately decreasing: F_{hi} by 0.8 kg/s (-2.2%) and F_{hi2} by 3.0 kg/s (-7.4%) as seen in Figures 4.13f and 4.13g. Due to a decrease in flow rate going through the reactor an increase in outlet temperature of ~1.0 °C is seen in Figure 4.13e. The system comes to a new equilibrium in approximately 1200 seconds with an overall decrease in the heat duty of ~650 kW (6.5%) as seen in Figure 4.13h.

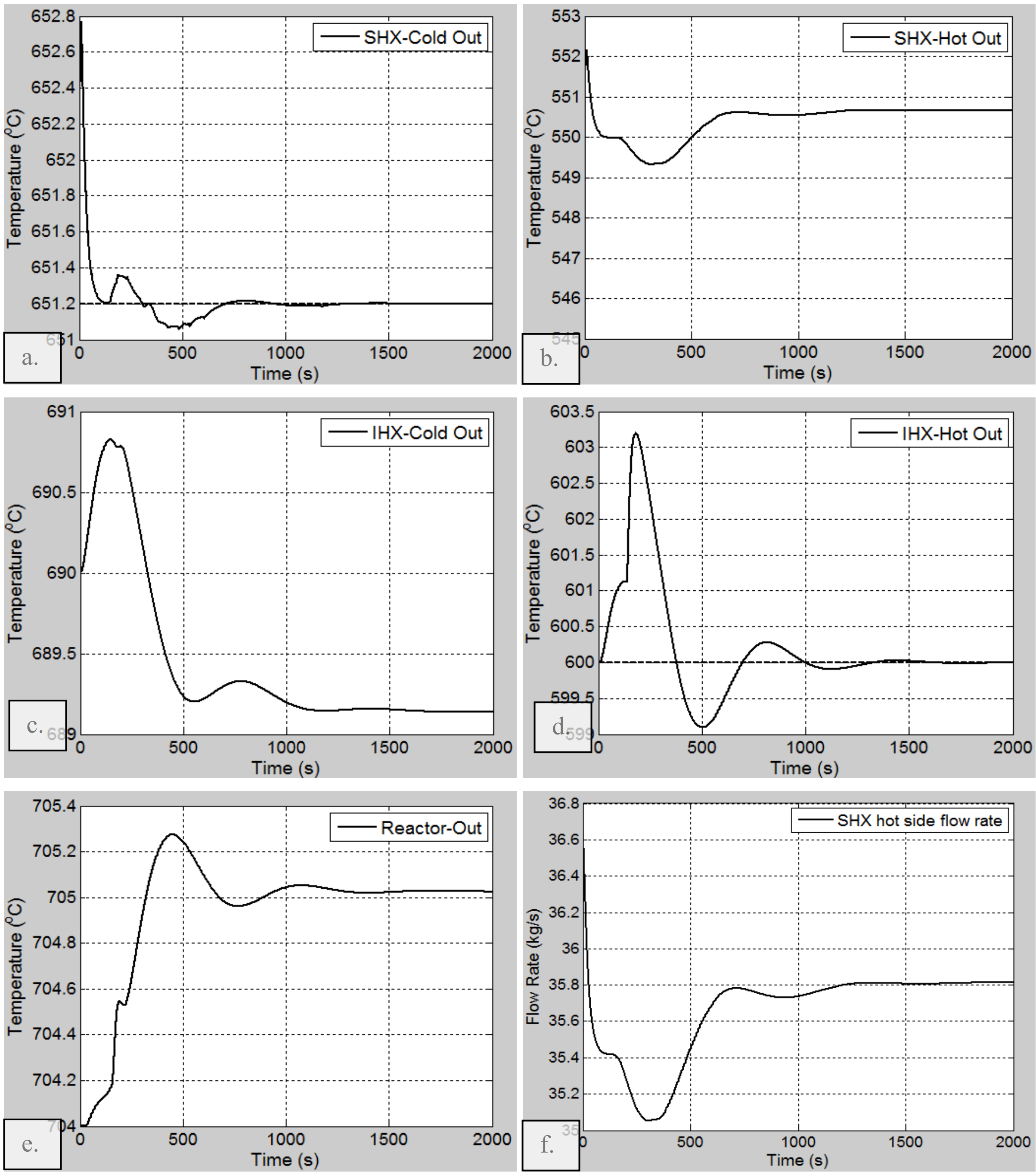

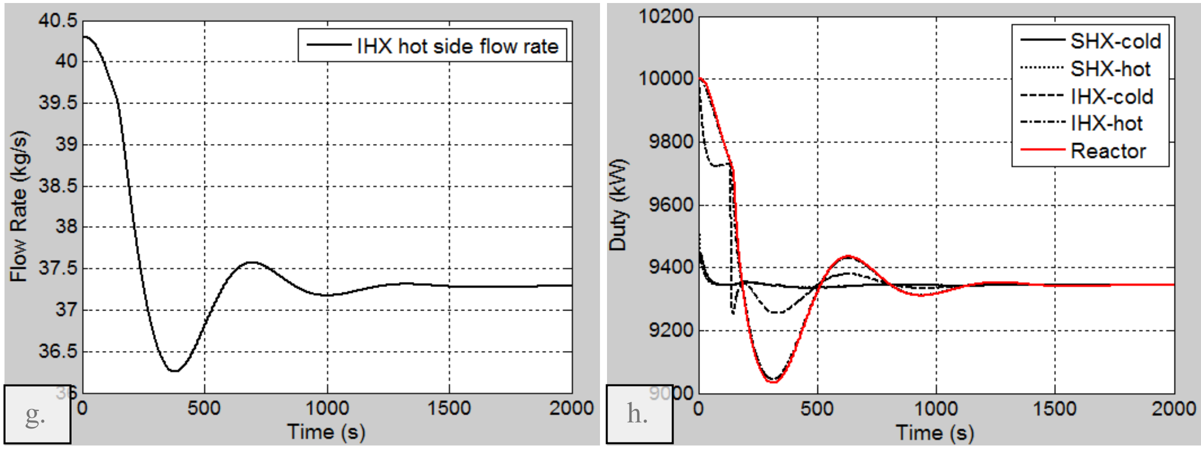

Figure 4.13. Controlled response of system after disturbance of +10 ^oC entering cold side of SHX. a: SHX cold outlet temperature, b: SHX hot outlet temperature, c: IHX cold outlet temperature, d: IHX hot side outlet temperature, e: Reactor outlet temperature, f: SHX hot side flow rate, g: IHX hot side flow rate h: Duties of SHX, IHX, and reactor.

Figure 4.14 shows the opposite case in which a temperature disturbance of -10 ^oC is introduced in the stream entering the cold side of the SHX (T_{ci}). Figures 4.14a and 4.14d show the controlled variables for the SHX (T_{co}) and IHX (T_{ho2}), respectively, returning to their set-point values by manipulating the hot side flow rates. Figures 4.14b and 4.14c, respectively, show the other temperatures not being controlled in the SHX (T_{ho}) and IHX (T_{co2}). At equilibrium T_{ho} increases by ~5.3 ^oC while T_{co2} increases by a little over 0.5 ^oC. To counteract the decrease in temperature of the controlled variables, both hot side flow rates (F_{hi}/F_{hi2}) increase: F_{hi} by ~0.9 kg/s (+2.5%) and F_{hi2} by ~3.1 kg/s (+7.7%) as seen in Figures 4.14f and 4.14g. The increase in the flow rate in the primary loop causes a decrease in the outlet temperature of the reactor of just under 1.0 ^oC as seen in Figure 4.14e. Again, the system is in equilibrium in ~1200 seconds with an overall duty increase of ~650 kW (6.5%) as seen in Figure 4.14h.

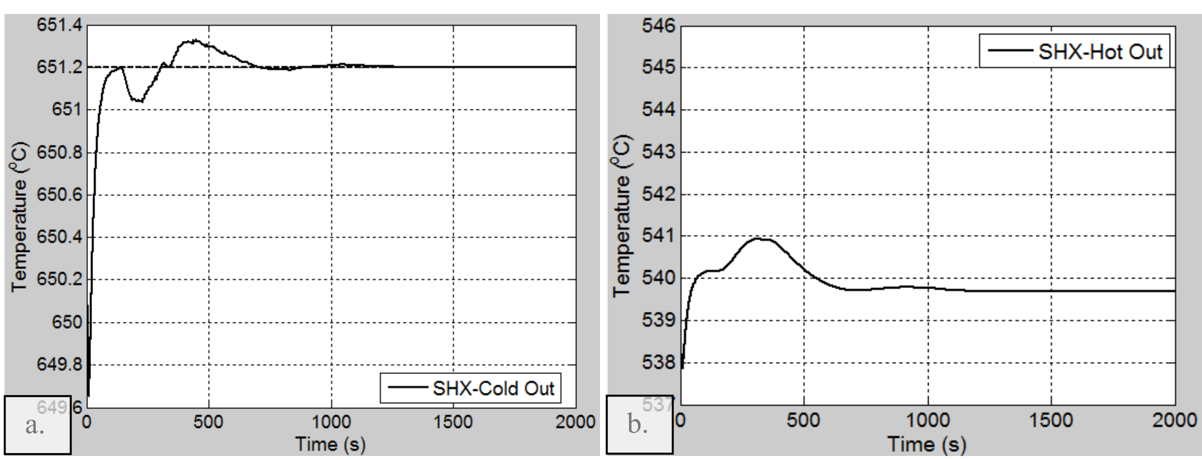

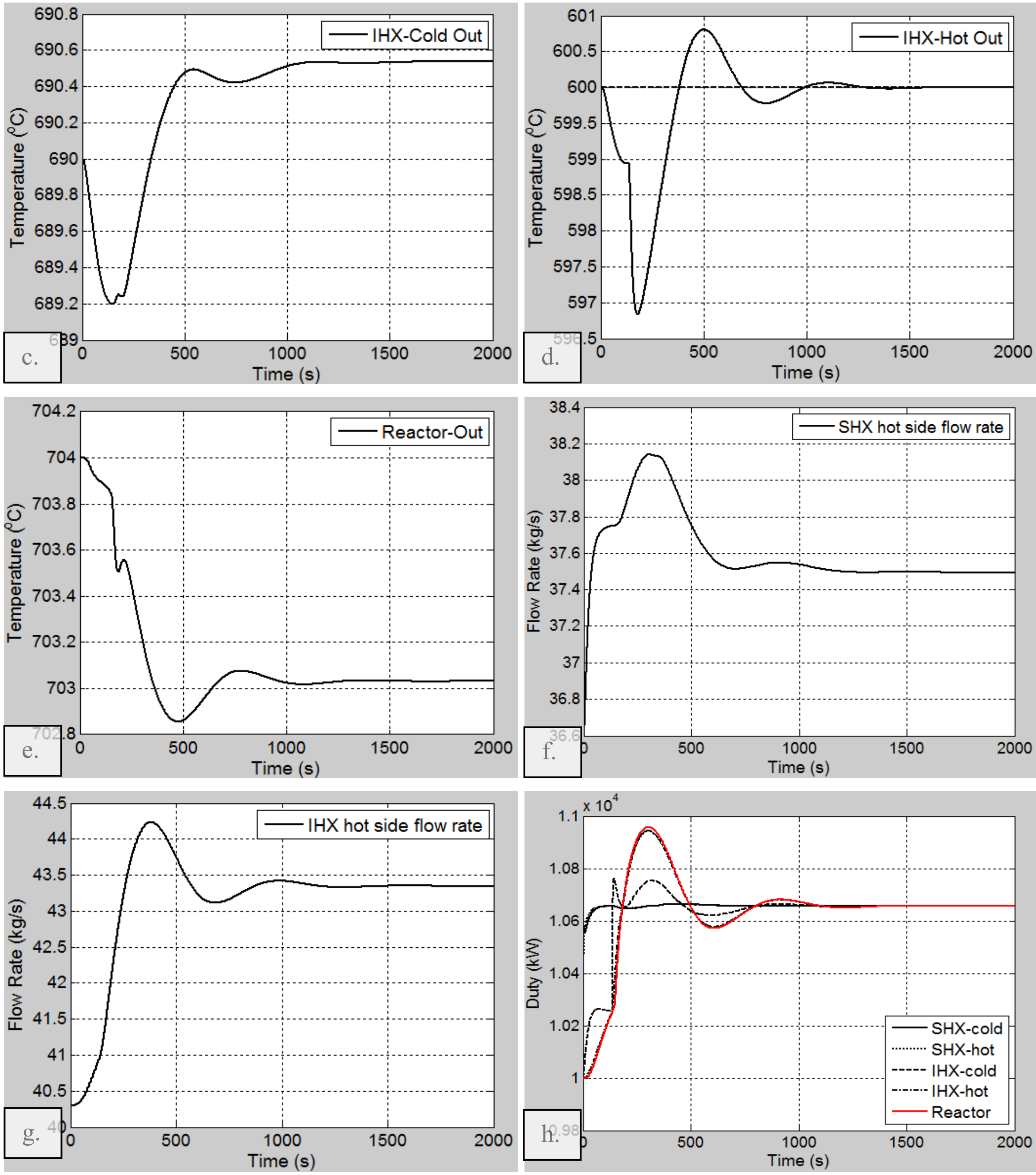

Figure 4.14. Controlled response of system after disturbance of -10 ºC entering cold side of SHX. a: SHX cold outlet temperature, b: SHX hot outlet temperature, c: IHX cold outlet temperature, d: IHX hot side outlet temperature, e: Reactor outlet temperature, f: SHX hot side flow rate, g: IHX hot side flow rate h: Duties of SHX, IHX, and reactor.

4.5.2.3 Flow Rate Disturbances

Figure 4.15 shows the system response after a -10 % step change in the cold side flow rate of the SHX (F_{ci}). Figures 4.15a and 4.15d show the controlled variables for the SHX (T_{co}) and IHX (T_{ho2}), respectively. The decrease in the flow rate causes an initial spike in the controlled temperature, triggering the control system to decrease the manipulated hot side flow rates (F_{hi}/F_{hi2}). The controlled temperatures return to their set-point values as seen in Figures 4.15a and 4.15d. Figures 4.15b and 4.15c show the other temperatures not being controlled in the SHX (T_{ho}) and IHX (T_{co2}), respectively. T_{ho} decreases by ~5.0 ^{o}C while T_{co2} increases by ~3.1 ^{o}C. F_{hi} decreases by 5.4 kg/s (-14.7%) and F_{hi2} decreases by 4.5 kg/s (-11.2%) as seen in Figures 4.15f and 4.15g. After the decrease in flow rate going through the reactor an increase in outlet temperature of ~1.6 ^{o}C is seen exiting the reactor, shown in Figure 4.15e. The system is at equilibrium within ~1000 seconds with an overall decrease in the thermal duty of 1000 kW or 10% of the initial duty as seen in Figure 4.15h.

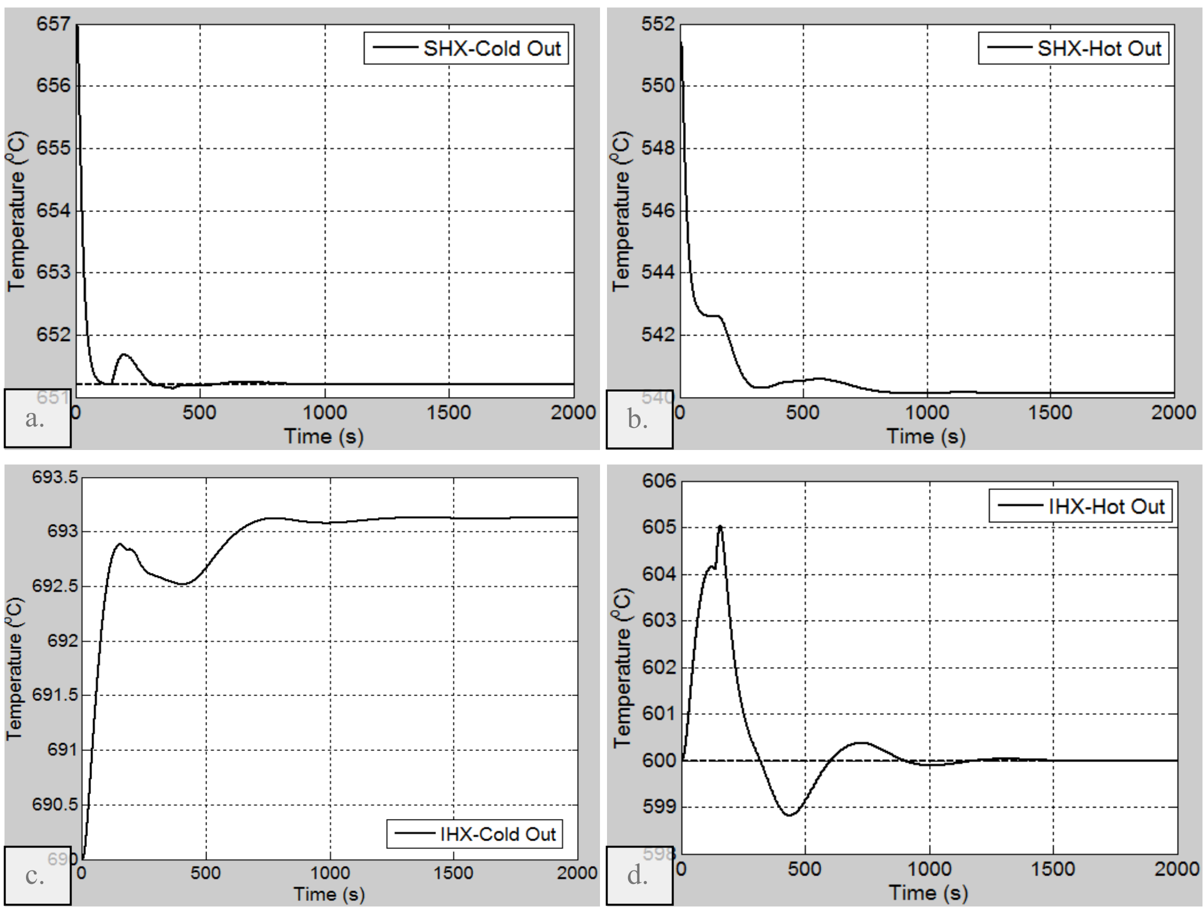

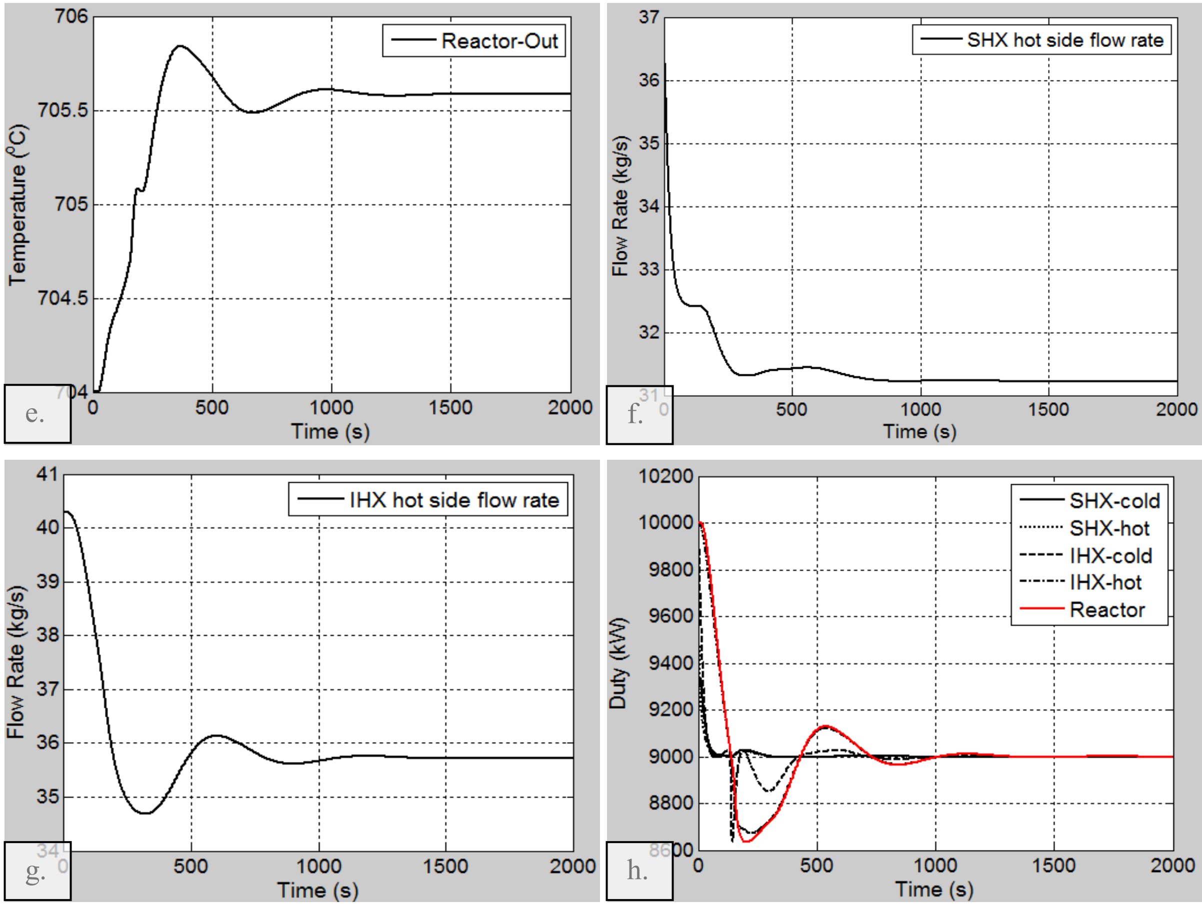

Figure 4.15. Controlled response of system after disturbance of -10% in the cold side flow rate of the SHX. a: SHX cold outlet temperature, b: SHX hot outlet temperature, c: IHX cold outlet temperature, d: IHX hot side outlet temperature, e: Reactor outlet temperature, f: SHX hot side flow rate, g: IHX hot side flow rate h: Duties of SHX, IHX, and reactor.

Figure 4.16 shows the system response after a +10 % step increase in the cold side flow rate of the SHX (F_{ci}). Figures 4.16a and 4.16d shows the controlled variables for the SHX (T_{co}) and IHX (T_{ho2}), respectively. Again, these are controlled around their set-point values after manipulation of the hot side flow rates. To counteract the decrease in temperature seen in the controlled variables both hot side flow rates (F_{hi}/F_{hi2}) must increase. F_{hi} increases by ~6.5 kg/s (+17.8%) and F_{hi2} increases by ~5.0 kg/s (+12.4%) as seen in Figures 4.16f and 4.16g. Figures 4.16b and 4.16c show the other temperatures not being controlled in the SHX (T_{ho}) and IHX (T_{co2}), respectively. T_{ho} increases by ~5.6 °C while T_{co2} decreases by ~3.7 °C. Due to the increase in flow rate going through the reactor, a decrease in outlet temperature of ~1.7 °C is seen exiting the reactor, seen in Figure 4.16e. The system is at equilibrium within ~1000 seconds with an overall duty increase of 1000 kW or 10% if the initial duty as seen in Figure 4.16h.

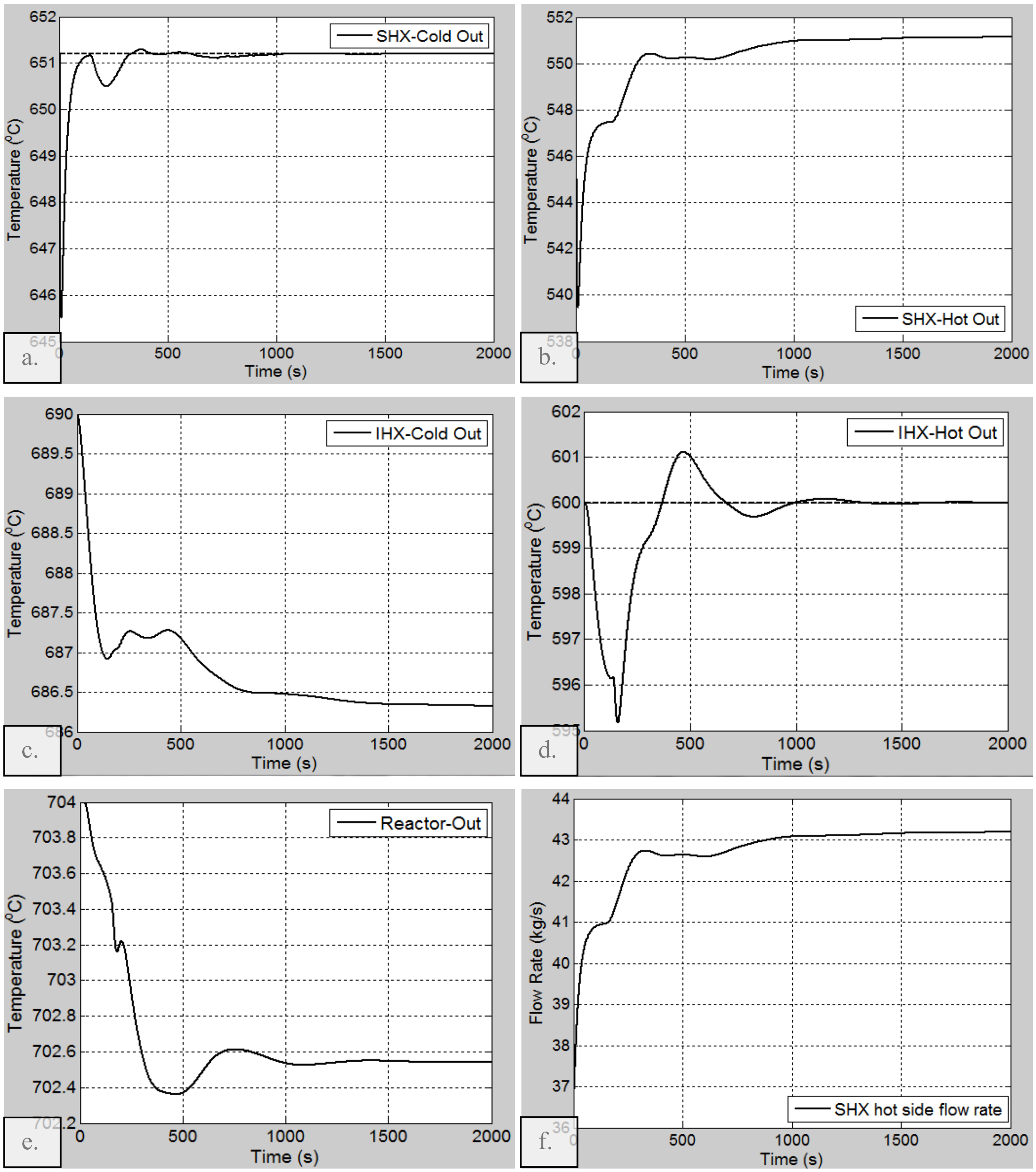
a.
SHX-Cold Out
Temperature (°C)
Time (s)
b.
SHX-Hot Out
Temperature (°C)
Time (s)
c.
IHX-Cold Out
Temperature (°C)
Time (s)
d.
IHX-Hot Out
Temperature (°C)
Time (s)
e.
Reactor-Out
Temperature (°C)
Time (s)
f.
SHX hot side flow rate
Flow Rate (kg/s)
Time (s)

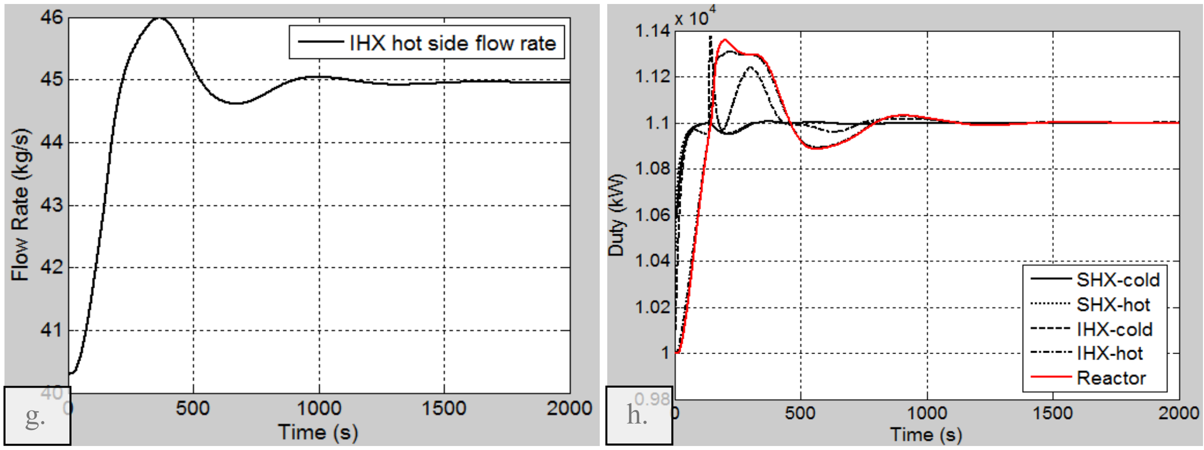

Figure 4.16. Controlled response of system after disturbance of +10 % in the cold side flow rate of the SHX. a: SHX cold outlet temperature, b: SHX hot outlet temperature, c: IHX cold outlet temperature, d: IHX hot side outlet temperature, e: Reactor outlet temperature, f: SHX hot side flow rate, g: IHX hot side flow rate h: Duties of SHX, IHX, and reactor.

4.5.2.4 Alternate Control Method

Control of both the cold side outlet temperature of the SHX (T_{co}) and the hot side outlet temperature of the IHX (T_{ho2}) by manipulation of hot side flow rate of both heat exchangers (F_{hi}/F_{hi2}) has been described above. However, there are other alternatives available for control as described below for the control of the cold outlet temperature of the SHX (T_{co}), which is the temperature of the stream providing the driving force for energy production in the power conversion unit or an alternate process, and hence considered to be the controlled variable of primary significance. The control options are:

- Control of T_{co} by manipulation of flow rate (could be F_{hi} or F_{ci})
- Control of T_{co} by controlling reactor power
    - Changing reactor power to equal the change in duty seen on the cold side of the SHX such that T_{co} will end up at its original value.
- A combination of reactor control and flow rate control
    - Initially reactor power is used to control T_{co}. As the temperature comes close to the set-point value, the system switches to using the hot side flow rate of the SHX to control T_{co}.

A comparison of the three alternatives for a disturbance of +20 °C in the temperature of the cold inlet stream of the SHX (T_{ci}) is described below.

Figure 4.17 shows the system response when the hot side flow rate of the SHX (F_{hi}) is manipulated to control the cold side outlet temperature (T_{co}). The initial increase in cold outlet temperature is mitigated by decreasing the hot side flow rate. As seen from Figure 4.17a, the controlled temperature T_{co} returns to its set point at ~600 seconds. The reactor outlet temperature decreases by about ~3.5 °C as shown in Figure 4.17b. The manipulated variable, the hot side flow rate (F_{hi}), changes by approximately -2.6 kg/s (-7.1%) shown in Figure 4.17c. Figure 4.17d, shows that the duties throughout the system decrease by approximately 1300 kW or 13% of the initial duty.

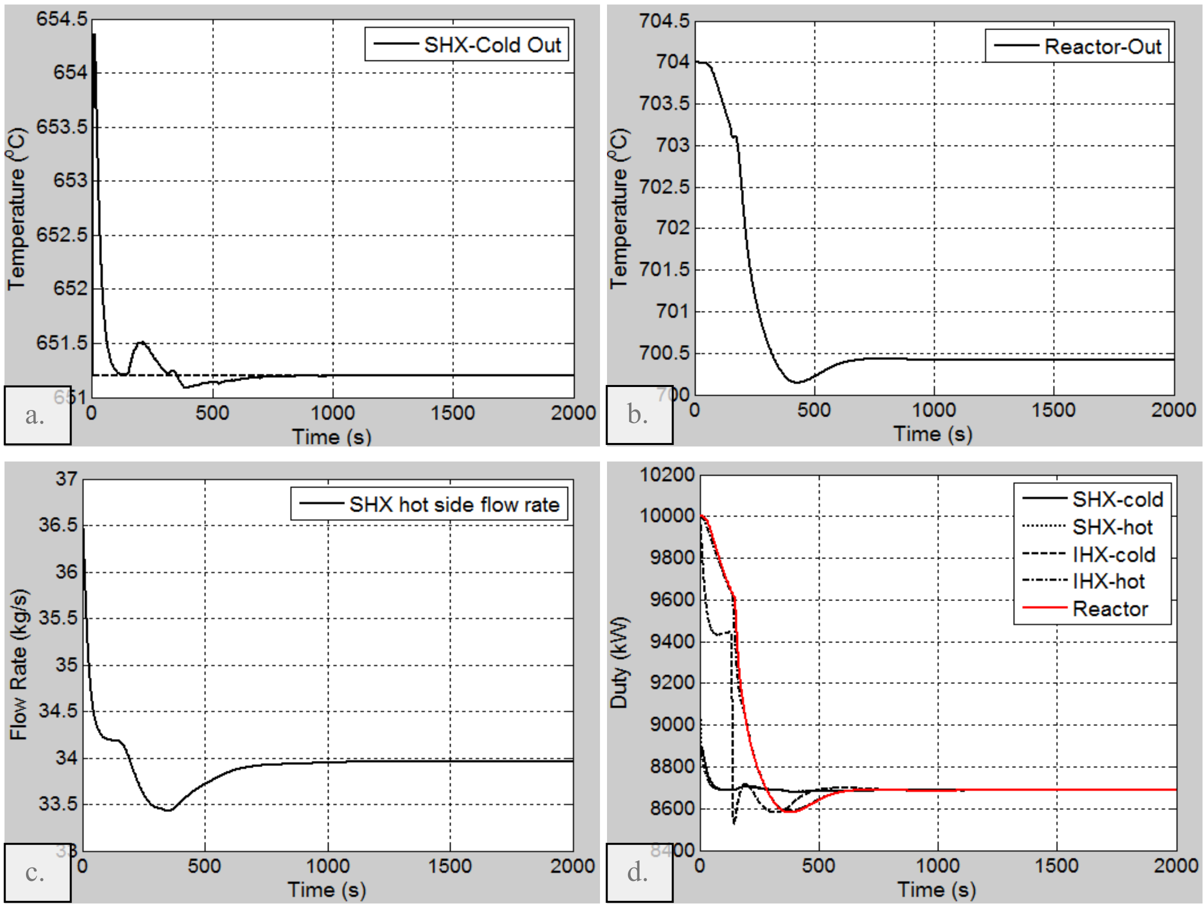

Figure 4.17. Controlled response of system after disturbance of +20 ºC entering cold side of SHX using flow rate for control. a: SHX cold outlet temperature, b: Reactor outlet temperature, c: SHX hot side flow rate, d: Duties of SHX, IHX, and reactor.

Figure 4.18 shows the transients for the same disturbance when the reactor power is used to control the cold side outlet temperature (T_{co}). In this case, the reactor power is controlled to equal the duty of the cold side of the SHX such that the cold outlet temperature will equal its set point value. Figure 4.18a shows that it takes ~1800 seconds to reset the controlled temperature to its set point. The reactor outlet temperature decreases by ~7 ºC as (Figure 4.18b), while the flow rate remains unchanged (Figure 4.18c). The final duty of the system will be the same as for the first option, decreasing by about 1300 kW or 13%, as seen in Figure 4.18d.

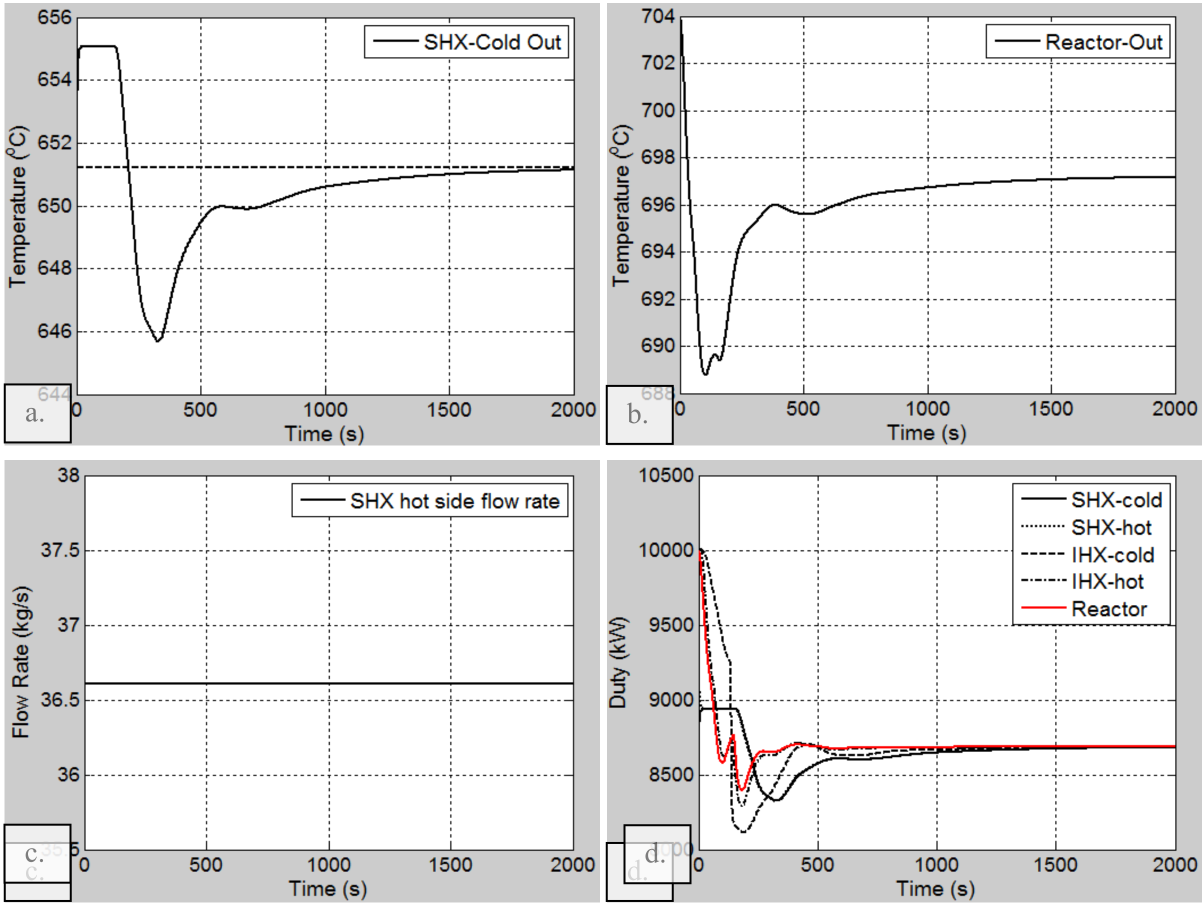

Figure 4.18. Controlled response of system after disturbance of +20 ºC entering cold side of SHX using reactor for control. a: SHX cold outlet temperature, b: Reactor outlet temperature, c: SHX hot side flow rate, d: Duties of SHX, IHX, and reactor.

Figure 4.19 shows the transients when the reactor power is manipulated followed by flow rate manipulation for controlling the cold side outlet temperature (T_{co}) for the same disturbance (20 ºC increase in the temperature of cold inlet stream of the SHX (T_{ci})). Initial control is accomplished by manipulating the reactor power until the controlled temperature T_{co} is within 1 ºC of the set point (at ~800 s), when the system switches to manipulating hot side flow rate (F_{hi}) for the final part of the control. Figure 4.19a shows that T_{co} is reset in ~900 seconds, while the reactor outlet temperature decreases by ~7.5 ºC (Figure 4.19b). As seen in Figure 4.19c, a small flow rate change of +0.75 kg/s or +2.0% is required. Again, the final duty of the system will be the same as seen previously decreasing by ~1300 kW or -13%, as seen in Figure 4.19d.

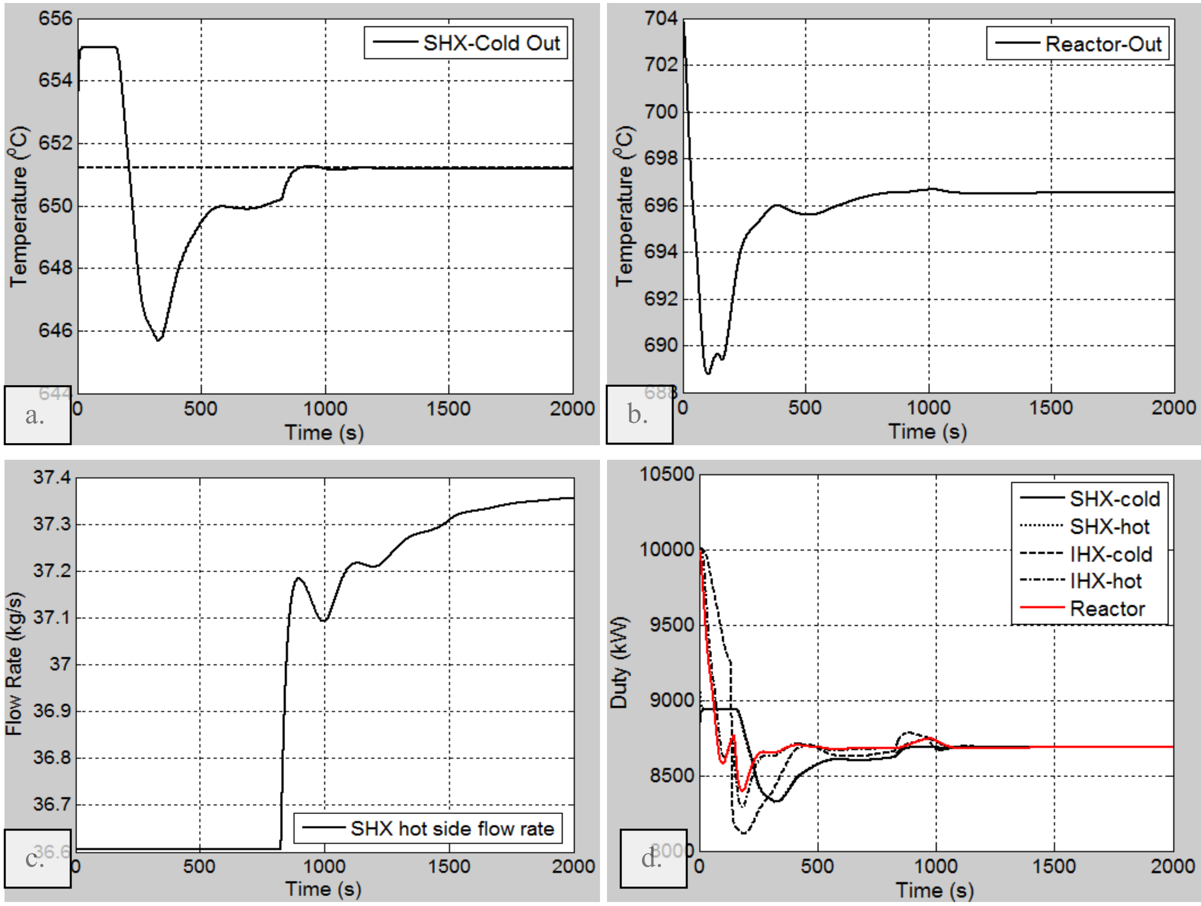

Figure 4.19. Controlled response of system after disturbance of +20 ºC entering cold side of SHX using reactor power followed by flow rate manipulation for control. a: SHX cold outlet temperature, b: Reactor outlet temperature, c: SHX hot side flow rate, d: Duties of SHX, IHX, and reactor.

It can be seen by using just the flow rate for control (the first option) the response is much quicker – new equilibrium is reached in ~600 s. However, a large change in flow rate - -7.1% in F_{hi} – is necessary. When using the reactor power only for control (the second option), the response is much slower (time to new equilibrium state tripled to ~1800 s) but no flow rate change is necessary. With the last scheme (the third option), the response time is between the two (response time ~900 s) and only a small change in flow rate (+2%) is necessary for the control. Depending on the situation, one of these schemes may be preferred over the others.

4.5.2.5 Summary of Control Results

The control system response to various disturbances is summarized in Table 4.9. As seen from the table, the system is able to establish a new steady state for step temperature disturbances and step flow rate disturbances coming from the process loop.

Table 4.9. Summary of control results for different disturbances with reactor.

Loop	Disturbance	SHX flow rate change %	IHX flow rate change %	Change in Thermal Duty kW
		Temperature Disturbances		
Process	-10 °C	F_{hi}= +2.5%	F_{hi2}= +7.7%	+650 (+6.5%)
	+10 °C	F_{hi}= -2.2%	F_{hi2}= -7.4%	-650 (-6.5%)
		Flow Rate Disturbances		
	-10% F_c	F_{hi}= -14.8%	F_{hi2}= -11.2%	-1000 (-10%)
	+10% F_c	F_{hi}= +17.8%	F_{hi2}= +12.4%	+1000 (+10%)

It can be seen that flow rate disturbances require a larger manipulation of the hot side flow rates than temperature disturbances for control. Normalizing the disturbances on the basis of the disturbance in the thermal duty indicates similar level of changes in the hot side flow rate of the IHX ($F_{hi2,}$ column 4) for both flow rate and temperature disturbances. However, for the SHX, a much larger change in the hot side flow rate ($F_{hi,}$ column 3) is necessary for flow rate disturbances than temperature disturbances. Apart from the magnitude of changes in flow rate, another factor of importance is the time period for which the cold side outlet temperature of the SHX (T_{co}) is not around its set point value. The simulation results show that at any given time the temperature does not exceed ~±5 °C from the design value with these disturbances due to the quick responses of the tuned PID controllers. In addition, the SHX responds quickly and within 100 seconds the temperature does not exceed 1 °C. Controlling the cold outlet temperature of the SHX allows for the process to run at high efficiencies. The SHX is much more compact compared to IHX, thus changes in the exchanger affect the parameters at a quicker rate. The larger IHX takes more time to react to changes in the flow rate.

The alternate control strategy results are summarized in Table 4.10.

Table 4.10. Equilibrium time and flow rate change for alternate control strategy.

Control Option	Disturbance	SHX flow rate change %	Equilibrium time s	Change in Thermal Duty kW
1	+20 °C	F_{hi}= -7.1%	600	-1300 (-13.0%)
2	+20 °C	F_{hi}= +0.0%	1800	-1300 (-13.0%)
3	+20 °C	F_{hi}= +2.0%	900	-1300 (-13.0%)

As can be seen from the table, control option 3 (reactor power manipulation followed by flow rate manipulation) response, while 50% slower than option 1 (flow rate manipulation only) is twice as fast as the option 2 (reactor power manipulation only). Further, the flow rate change needed for option 1 is more than 3 times as high as that for option 3. The third control method has a quick response and only a small change in the flow rate is necessary. However, the controlled temperature is far from the set point value for ~300 seconds longer than control option 1. This could have an effect on the efficiency of the process. The process is designed to operate for a narrow range of temperature and a minimum temperature must be present to prevent process failure. A larger disturbance may cause the temperature to dip below the minimum value so a quick response, as seen in control option 1, may be desired. If only minimal changes in the temperature are seen entering the process, control option 3 may be favored in order to prevent large flow rate changes in the secondary loop.

4.5.3 Modeling and simulation of helium Brayton Cycle PCS

The control strategy and system behavior described above has a broad general applicability all process applications including direct utilization of heat and generation of electricity. Further investigations were conducted to determine the transient behavior of the helium Brayton cycle based PCS shown earlier in Figure 4.2.

4.5.3.1 Steady State Design Methodolgy

The recuperator and the precooler are heat exchangers and the established design equations can be used for their design. The design procedure for the turbine and compressor is as follows:

The turbine and compressor the outlet temperature are related to pressure ratios, inlet temperatures and equipment efficiency by Eq. 4.25 and 4.26 (Amin and Rocco, 2006).

$$T_{t2} = T_{t1}\left[1 - \eta_t\left(1 - PR_t^{\frac{1-k}{k}}\right)\right] \tag{4.25}$$

$$T_{c2} = T_{c1}\left[1 + \frac{1}{\eta_c}\left(PR_c^{\frac{k-1}{k}} - 1\right)\right] \tag{4.26}$$

where T is the temperature, η is the efficiency of the unit, PR is the pressure ratio (PR=P1t/P2t or P2c/P1c), and k is the specific heat ratio which is defined as C_p/C_v. The subscripts *1, 2, t,* and *c* stand for inlet, outlet, turbine, and compressor, respectively. Calculation of the outlet temperature involves determining first the pressure ratio and efficiency for each equipment. The technique presented by Wright et al. (2006) based on the turbine and compressor performance maps shown in Fig. 4.20 and 4.21, respectively, was used to determine these parameters. The x-axis is the specific speed (N_s) and the y-axis specific diameter (D_s), both dimensionless parameters and are defined in Eq. 4.27 and 4.28. With a known specific speed and specific diameter the efficiency of the turbine or compressor can be determined from the plots.

$$N_s = \frac{2\pi N\sqrt{\dot{V}}}{H^{3/4}} \tag{4.27}$$

$$D_s = \frac{DH^{1/4}}{\sqrt{\dot{V}}} \tag{4.28}$$

Where N is the rotating speed of the rotar or impeller, $\dot{V}$ is the volumetric flow rate, H is the adiabatic head, and D is the diameter of the rotar or impeller. N must be the same for both the compressor and turbine as they are connected to the same shaft.

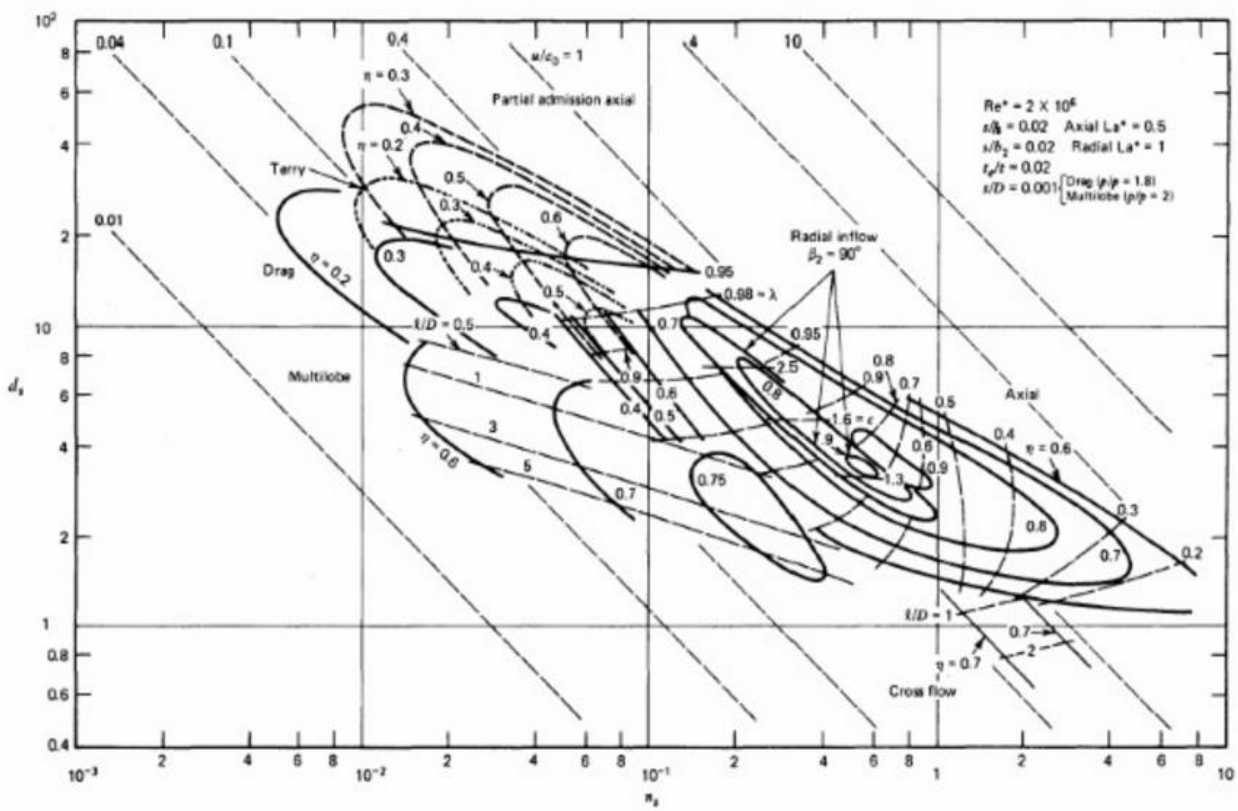

Figure 4.20. Turbine performance map.

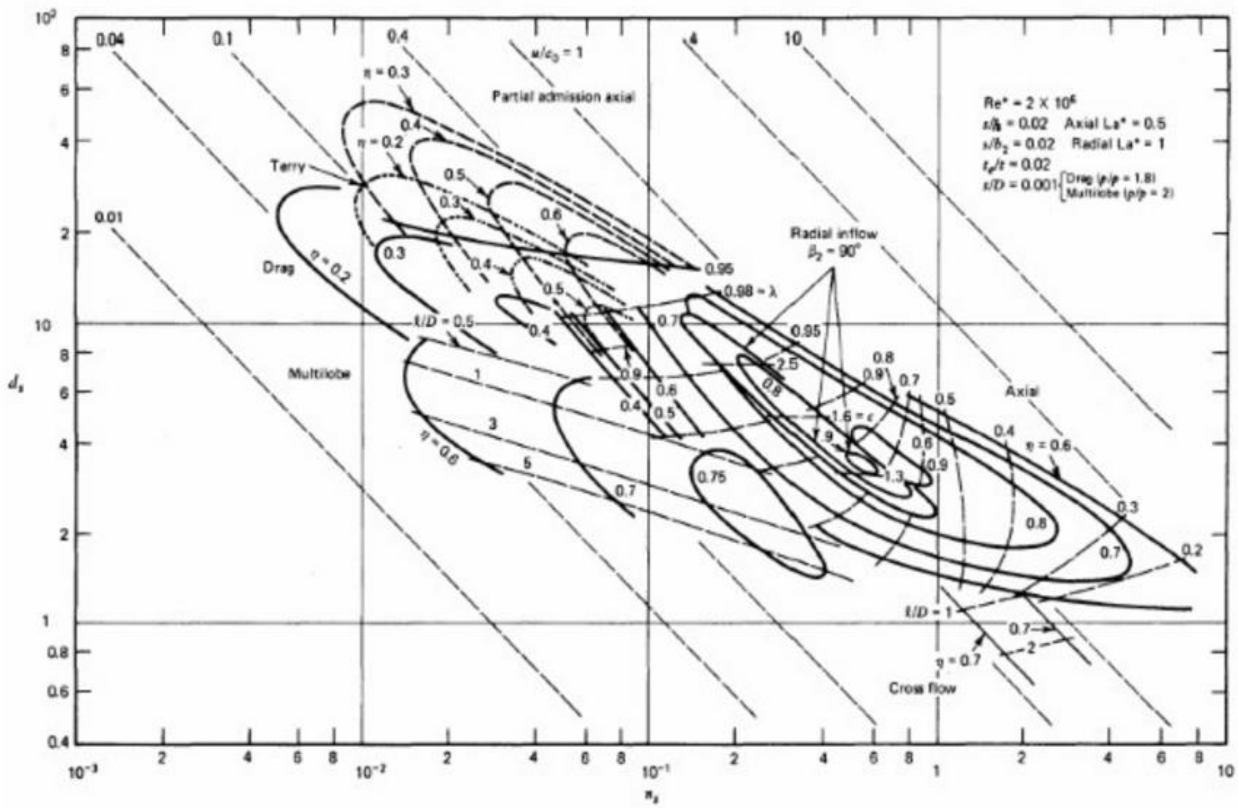

Figure 4.21. Compressor performance map.

It can be seen from the above plots that there is a specific speed and a specific diameter that will make the turbine and compressor the most efficient. For the turbine an N_s of around 0.7 and a D_s of around 3.0 would be the most efficient. For the compressor, the values of N_s and D_s are ~1.5 and ~3.0, respectively. With a given flow rate the volumetric flow rate can be found. Then at a given rotational speed the adiabatic head required for the N_s to be at the optimal point can be found. The adiabatic head is the head required if it assumed that no heat is lost to the surroundings. Using Eq. 4.29, which estimates adiabatic head, the pressure ratio can be calculated.

$$H = C_p T_{in} \left(PR^{\frac{k-1}{k}} - 1 \right) \tag{4.29}$$

Where T_{in} is the inlet temperature for either the turbine or compressor and the other variable as previously stated. The last step is using Eq. 4.28 to find the optimal diameters of the impeller and rotor. Assuming that the turbine or compressor is at the optimum specific diameter, new plots can be made based off the graphs that relate specific speed to efficiency. These are shown in Figure 4.22. These plots will be useful for off-design performance. If D_s stays relatively constant then changes in N_s will determine the efficiency of the turbine or compressor.

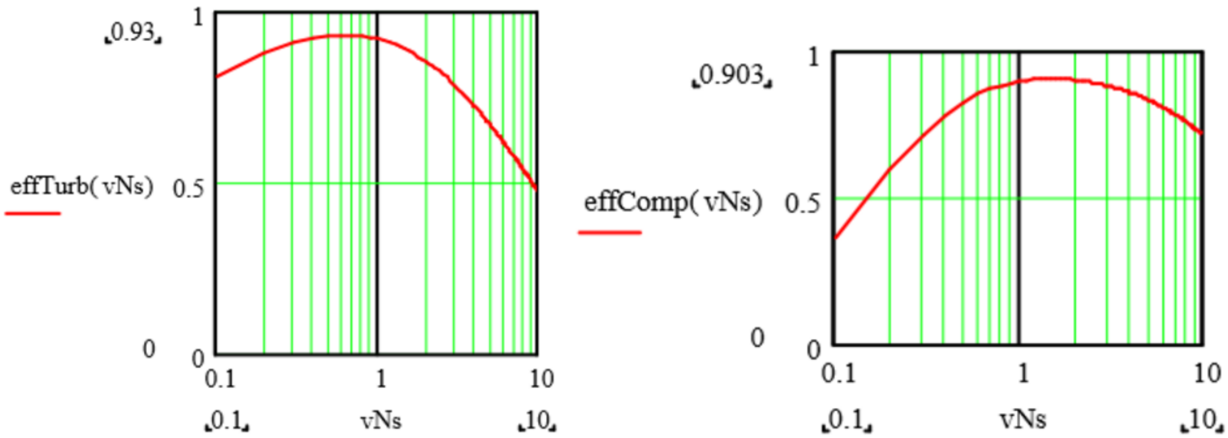

Figure 4.22. Efficiency of turbine (left) and compressor (right) based off specific speed

With known pressure ratios and efficiencies initial outlet temperatures for the turbine and compressor can be found using Eq. 4.24 and 4.25. Some results for a design of a turbine and compressor are shown in Table 4.11. The flow rate in the system is 12.6 kg/s, the inlet turbine pressure is 7 MPa, and the rotational speed is 70,000 rpm. For this design, the nominal net capacity is found to be ~1.34 MWth.

Table 4.11. Design parameters of turbine and compressor.

Unit	N_s	D_s	T_1	PR	η	D	T_2
Turbine	0.7	3.3	651.2	1.4404	0.9117	0.2290	571.0
Compressor	1.5	2.8	200	1.4404	0.8861	0.2267	259.8

4.5.3.2 Transient Analysis

With the design point values found for the turbine and compressor, the model for transient analysis can then be developed. The equations used for the recuperator and precooler are identical and are shown in Eqs. 4.30-4.32.

$$m_h C_{ph} \frac{dT_h}{dt} + F_h C_{ph}(T_{ho} - T_{hi}) = (hA)_h(T_w - T_h) \tag{4.30}$$

$$m_c C_{pc} \frac{dT_c}{dt} + F_c C_{pc}(T_{co} - T_{ci}) = (hA)_c(T_w - T_c) \tag{4.31}$$

$$m_w C_{pw} \frac{dT_w}{dt} = (hA)_h(T_h - T_w) - (hA)_c(T_w - T_c) \tag{4.32}$$

Where *m* is the mass of the coolant or metal in that node, *Cp* is the heat capacity, *T* is the temperature, *F* is the flow rate, *h* is the heat transfer coefficient, and *A* is the heat transfer area. The heat transfer coefficients were calculated based off the models described in the previous report (*3363_2016_Q2.pdf*). These are similar to the differential equations used for the transient analysis of the IHX and SHX. In the model the heat exchangers is discretized and at each node the cold side, hot side, and wall temperatures calculated. Similar to the IHX and SHX the fourth-order Runge-Kutta method is implemented for numerical analysis.

The turbine and compressor require a different set of equations for transient analysis. With known turbine parameters a group of equations can be used to find the change in flow rate and the change in efficiency. Change in the flow rate of the system are dependent on changes that occur within the turbine and are described by Eq. 4.33 (Heng, 2011):

$$F = F_p \frac{P_{in}}{P_{in,p}} \sqrt{\frac{T_{in}}{T_{in,p}}} \sqrt{\frac{1-PR_T^{-2}}{1-PR_{T,p}^{-2}}} \tag{4.33}$$

Where *F* is the flow rate, *P* is the pressure, *T* is the temperature, and *PR* is the pressure ratio. The subscript *p* stands for the parameters at the nominal mode of operations at 100% power. These would be the initial design values. The pressure ratio will need to be estimated based on changes in temperature and pressure and then the change in flow rate may be found which in turn will affect the other units in the system. To find the change in turbine efficiency, Eqs. 4.34 and 4.35 are used.

$$x_{OT} = \frac{N}{N_p} \sqrt{\frac{T_{in,p}\left(1-PR_{T,p}^{-(\kappa-1)/\kappa}\right)}{T_{in}\left(1-PR_T^{-(\kappa-1)/\kappa}\right)}} \tag{4.34}$$

$$\eta_{T,ad} = \eta_{T,ad,p}(2x_{OT} - x_{OT}^2) \tag{4.35}$$

Where *N* is the rotational speed, κ is the specific heat ratio, and η is the efficiency. With the known change in pressure ratio and efficiency, a new outlet temperature may be found using Eq. 4.25. Of course changes that occur in the outlet of the turbine will propagate to the hot side of the recuperator which will then have effect on the parameters within that unit. Changes in the recuperator will further propagate to the precooler and then to the compressor where the changes will have an effect on the efficiency and pressure ratio.

Transient analysis for a compressor is slightly trickier as it requires a compressor map to predict changes efficiency and pressure ratio. These are typically created from the experimental data for that particular compressor. They vary from compressor to compressor so it can be difficult to create this without the necessary information. These charts require corrected match flow rare (F_{cor}) and corrected rotational speed (N_{cor}) and are defined in Eqs. 4.36 and 4.37 (Wenlong et al, 2012).

$$F_{cor} = \frac{F}{F_p}\frac{101325}{P_{C,in}}\sqrt{\frac{288}{T_{C,in}}} \tag{4.36}$$

$$N_{cor} = \frac{N}{N_p}\sqrt{\frac{288}{T_{C,in}}} \tag{4.37}$$

Where the subscript *cor* stands for correct mass flow rate (*F*) or corrected rotational speed (*N*). A typical compressor map is shown in Figure 4.23. The map shows the pressure ratio as a function of the normalized flow rate, with the dashed lines representing the constant efficiency curves. The solid lines represent constant speed with the speed increasing from left to right. This chart is used to find the new pressure ratio and compressor efficiency, if parameters in the compressor change such as inlet temperature, inlet pressure or flow rate.

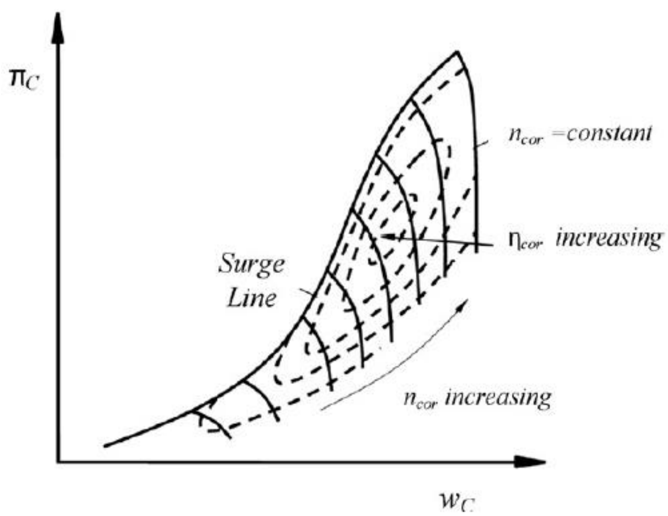

Figure 4.23. Typical compressor performance curve

This typical performance curve can be used to create charts that can represent the system. Assuming the compressor is designed at the most optimal point, we have values for the pressure ratio and corrected mass flow rate at that point. The WebPlotDigitizer tool (http://arohatgi.info/WebPlotDigitizer/) can be used to convert obtain numerical values of x-y coordinates of different curves from the performance chart, such as the one shown in Figure 4.23. From these data, charts can be created and best fit lines made that can be included in the model code. Figure 4.24 and 4.25 show the performance curves created from Figure 4.23. In Figure 4.24 the corrected mass flow rate (x-axis) is used to find the pressure ratio (y-axis). Each of the curves represents different rotational speed, with the green line (100%) representing the design speed. Figure 4.25 uses the corrected mass flow rate (x-axis) to find the efficiency (y-axis) of the compressor. Similarly, each of the lines represents different rotational speed, with the green line (100%) representing the design speed. A large change in the corrected mass flow rate requires changing the rotational speed to maintain high efficiency. For example, from Figure 4.25, the compressor efficiency at the corrected mass flow rate of 0.025 and 100% speed (green line) is close to 90%. If the corrected mass flow rate were to decrease to 0.0235, then the compressor efficiency at the design speed is only ~70%. In this case, higher efficiency can be achieved by decreasing the speed to 90% of the design value, raising the efficiency to ~85%. Figure 4.24 can then be used to obtain the pressure ratio, and the outlet pressure. Thus, the changes in outlet conditions in response to changes in the inlet conditions could be found.

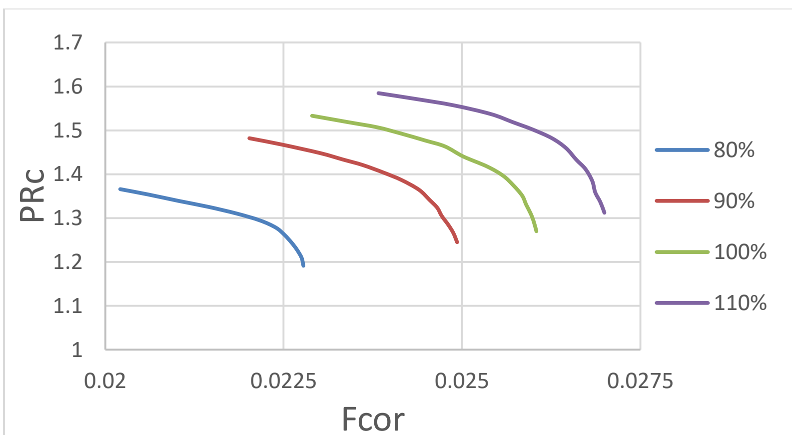

Figure 4.24. Performance curves to find compressor pressure ratio.

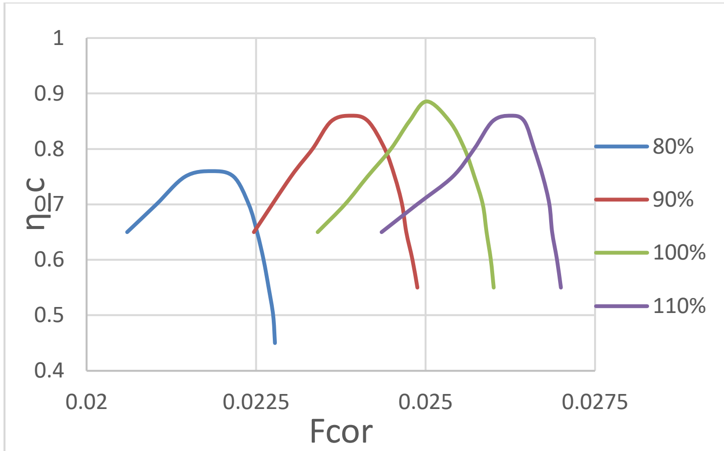

Figure 4.25. Performance curves to find compressor efficiency.

4.5.3.3 Transient Analysis Examples

Preliminary results of the transient analysis conducted for the PCS in response to two different types of disturbances are described below.

Figure 4.26 shows an example of the system response in terms of the temperatures of various streams to a flow rate disturbance involving a 20% increase in the cold side flow rate in the precooler. The precooler cold side outlet temperature decreases by 3 °C (Figure 4.26d), while the recuperator cold outlet stream experiences a temperature change of -1.2 °C (Figure 4.26b). The temperatures at the outlets of the recuperator and compressor decrease by 4.1 °C and 5.3 °C as seen from Figure 4.26c and 4.26f, respectively. The precooler hot outlet stream experiences the greatest decrease in temperature (8 °C, Figure 4.26e), while the turbine outlet temperature remains unchanged (Figure 4.26a).

Turbine Out: 571.0 °C → 571.0 (0 °C)

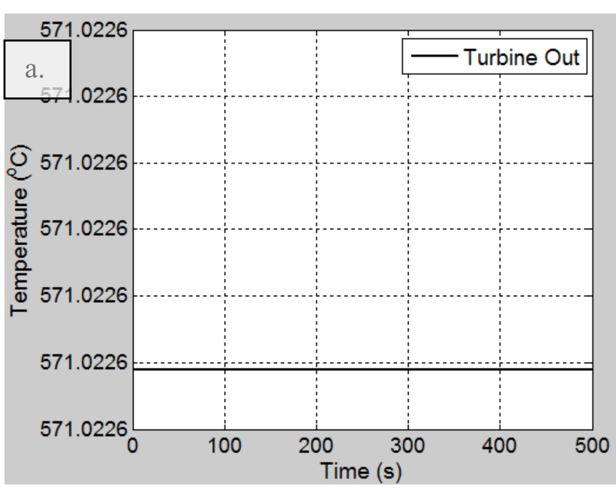

Recuperator Cold Out: 498.9 °C → 497.7 (-1.2 °C)

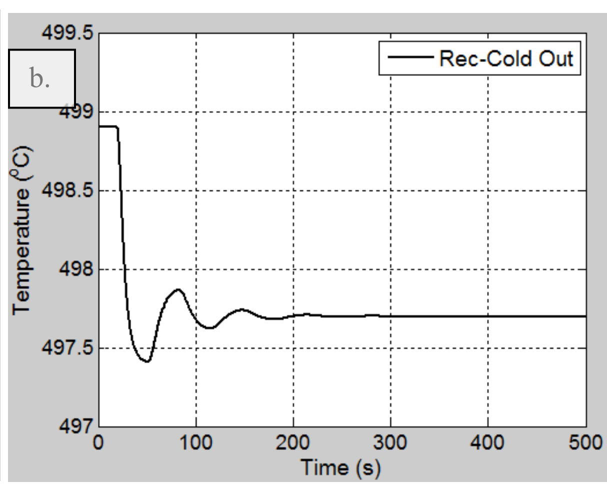

Recuperator Hot Out: 335.6 ºC → 331.5 (-4.1 ºC) Precooler Cold Out: 43.3 ºC → 40.3 ºC (-3.0 ºC)

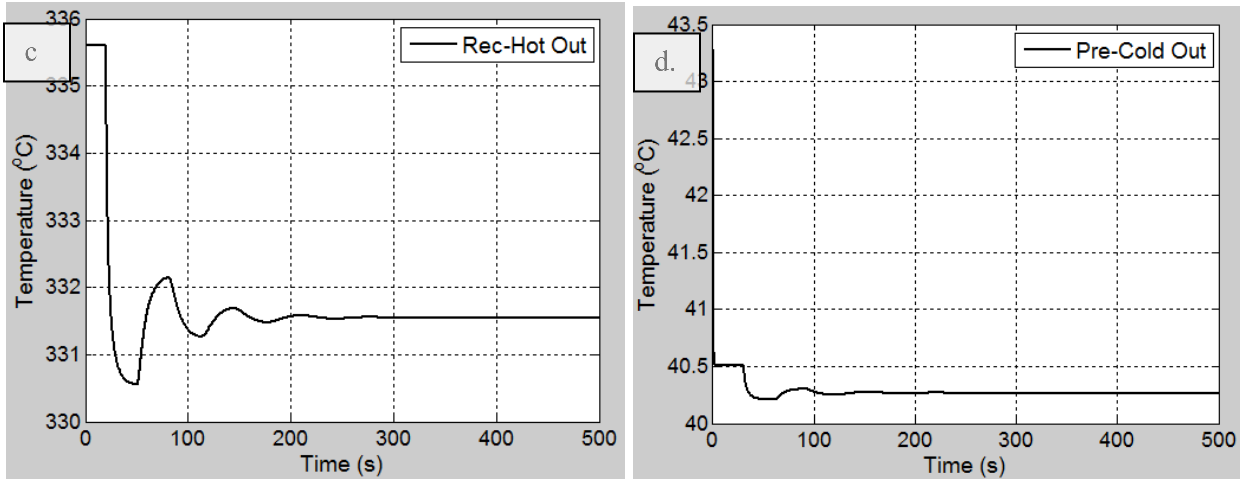

Precooler Hot Out: 200 ºC → 192.0 ºC (-8.0 ºC) Compressor Out: 263.4 ºC → 258.1 ºC (-5.3 ºC)

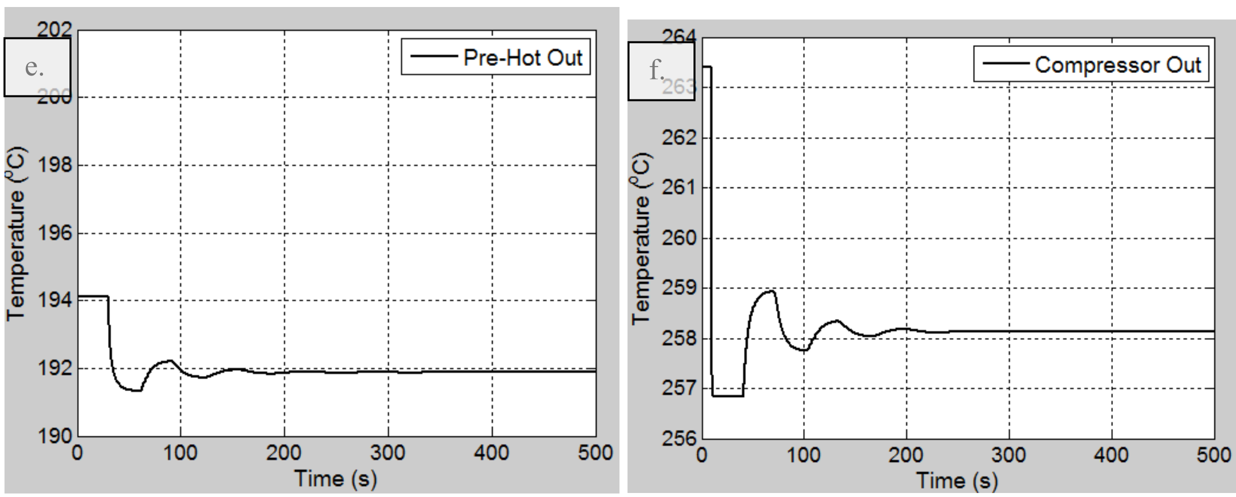

Figure 4.26. Helium Brayton cycle response to a +20% disturbance in the precooler cold side flow rate

Figure 4.27 shows the system response in terms of the temperatures of various streams to a temperature disturbance involving a 15 ºC increase in the temperature of the stream entering the turbine. The greatest changes are observed in the temperature of outlet streams from the turbine and recuperator cold side (15.2 ºC and 11.7 ºC, Figures 4.27a and 4.27b, respectively). Recuperator hot side outlet temperature increases by 3.2 ºC (Figure 4.27c), while the precooler hot outlet temperature increases by only 0.3 ºC (Figure 4.27e). The precooler cold side outlet temperature is unchanged (Figure 4.27d), while the compressor outlet temperature decreases by 0.4 ºC (Figure 4.27f).

Turbine Out: 571.0 ºC → 586.2 ºC (+15.2 ºC)

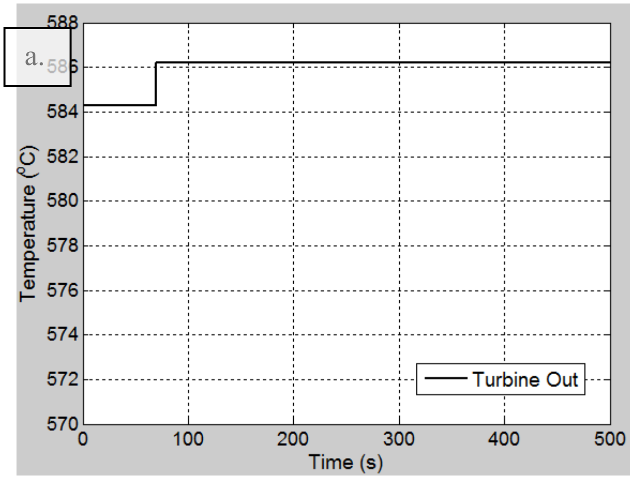

Recuperator Cold Out: 498.9 ºC → 510.6 (+11.7 ºC)

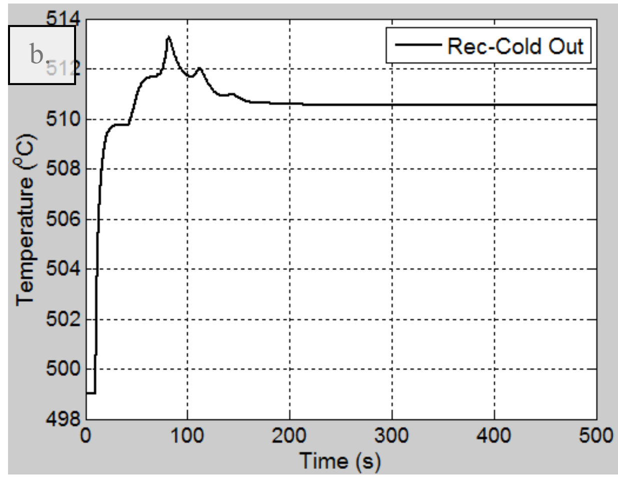

Recuperator Hot Out: 335.6 ºC → 338.8 (+3.2 ºC)

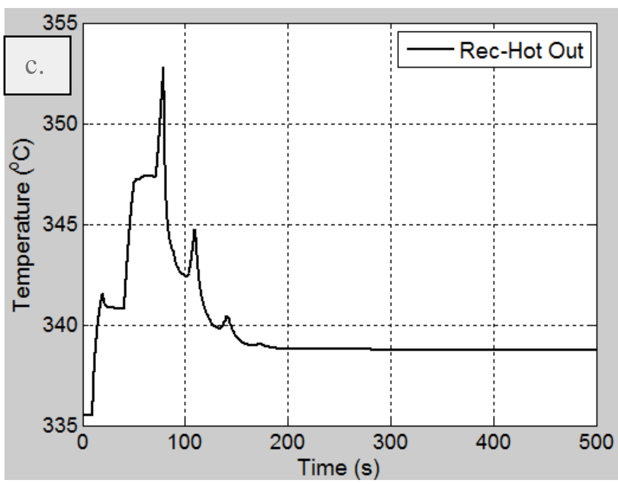

Precooler Cold Out: 43.3 ºC → 43.3 ºC (0 ºC)

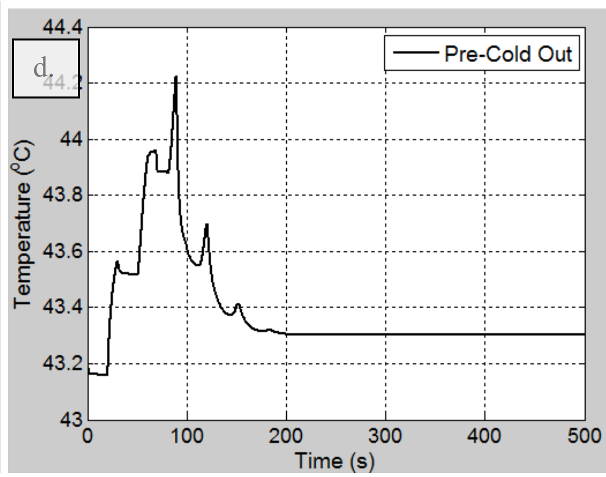

Precooler Hot Out: 200 ºC → 200.3 ºC (+0.3 ºC)

Compressor Out: 263.4 ºC → 263.0 ºC (-0.4 ºC)

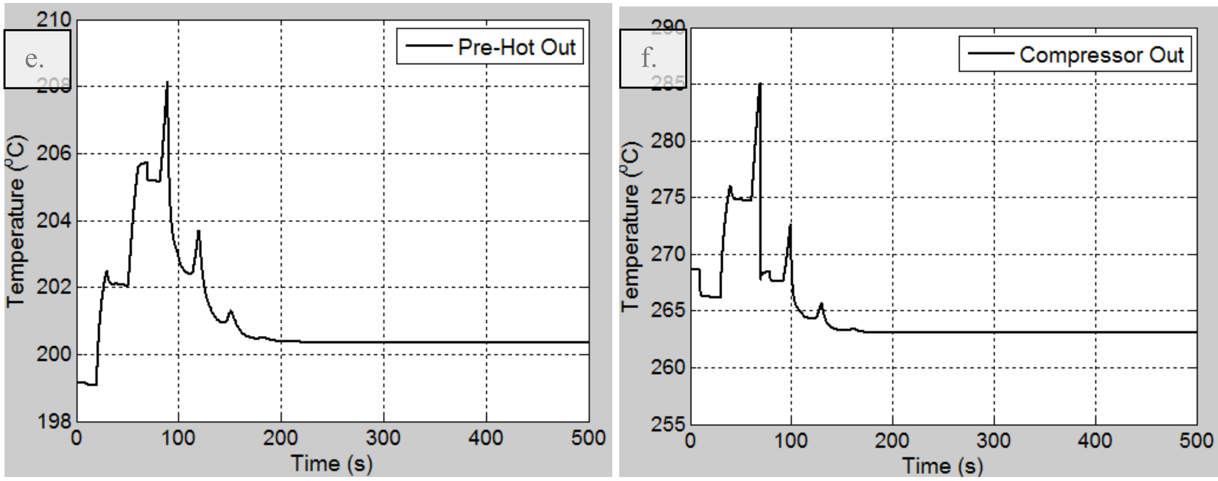

Figure 4.27. Helium Brayton cycle response to a 15°C increase in the temperature of the turbine inlet stream

The preliminary results presented above indicate that the transient analysis technique developed in the research can be employed successfully to predict the response of the helium Brayton Cycle PCS to various temperature and flow disturbances in the system. This analysis provides the foundation for further development of control techniques for a stable operation of the overall system.

4.6 Summary

A control system architecture was developed for the advanced nuclear reactor-heat exchanger system, and the dynamics and control of the system was simulated for various scenarios using user developed MATLAB codes. The control system consisted of two controllers – one to control the temperature of the cold side outlet stream of the SHX (T_{co}) and the other to control the temperature of the hot side outlet stream of the IHX (T_{ho2}) by manipulating either the hot side flow rates (F_{hi}/F_{hi2}), cold side flow rates (F_{ci}/F_{ci2}), or combination of these.

It was found that the disturbances in the primary loop had an overall greater impact on the system. It may be best to have a control strategy in which the manipulated variables depend on where the disturbance occurs. For example, if the disturbance is from the process side then the hot side flow rates (F_{hi}/F_{hi2}) may be the desired manipulated variables. However, if the disturbance comes from the primary loop then using the cold side flow rates (F_{ci}/F_{ci2}) may produce better control. In addition, switching of the manipulated variable after a certain pre-set limit ($\pm$20% change in the manipulated variable) was reached for that variable was investigated. This limit is reached for larger temperature disturbances in the system, which triggered a switching of the manipulated variables. The system was able to come to a new equilibrium state relatively quickly while successfully maintaining the controlled temperatures at their set points.

The behavior of the system under a comprehensive control scheme where the nuclear reactor operation is also controlled was also simulated. The reactor model included the point kinetic equations with 3 groups of delayed neutrons, which achieved the best balance between the computational load and accuracy. Two types of control strategies were implemented into the model. The first was identical to the first MATLAB model and involved 2 controllers in which the cold side outlet temperature of the SHX (T_{co}) and hot side outlet temperature of the IHX (T_{ho2}) are controlled by manipulation of the hot side flow rate of the SHX (F_{hi}) and hot side flow rate of the IHX (F_{hi2}). Temperature disturbances of ±10 ^{o}C required flow rate changes of ±2-8% of their initial value to properly control the system. Flow rate disturbances of ±10% F_c required a larger change in flow rate of ±11-18% of their initial values for control. The second control strategy involved the control of the cold outlet temperature of the SHX (T_{co}) using 3 different control options. The first involved manipulating the flow rate, the second controlling the reactor power and the third a combination of the first two options. The final control option combines the advantages from the other two control options – rapidity of the response from option one, and minimal flow rate change from option two – and is potentially a superior option compared to the first two.

A comprehensive model was developed to obtain the dynamics of the helium Brayton Cycle PCS in response to any system disturbances. The recuperator and precooler were modeled similarly to the any other heat exchanger, while a novel technique was used for the turbine and the compressor. Temperature transients of various streams in response to different disturbance stimuli were obtained indicating the utility of this approach.

5. Experimental Validation

The experimental validation was conducted at The Ohio State University (OSU) utilizing the high temperature helium facility (HTHF) and the high-temperature molten salt facility. Both these facilities are described below.

5.1 Description of Facilities

5.1.1 High-Temperature Helium Facility (HTHF)

The HTHF was constructed to facilitate thermal-hydraulics performance testing of heat exchangers at temperatures and pressures up to 800°C and 3 MPa, respectively. HTHF consists of two heaters, a gas booster to boost the helium pressure, a cooler, pipes, valves, and various instruments. Figure 5.1 shows the layout of the HTHF while figure 5.2 shows the operational schematic under test conditions.

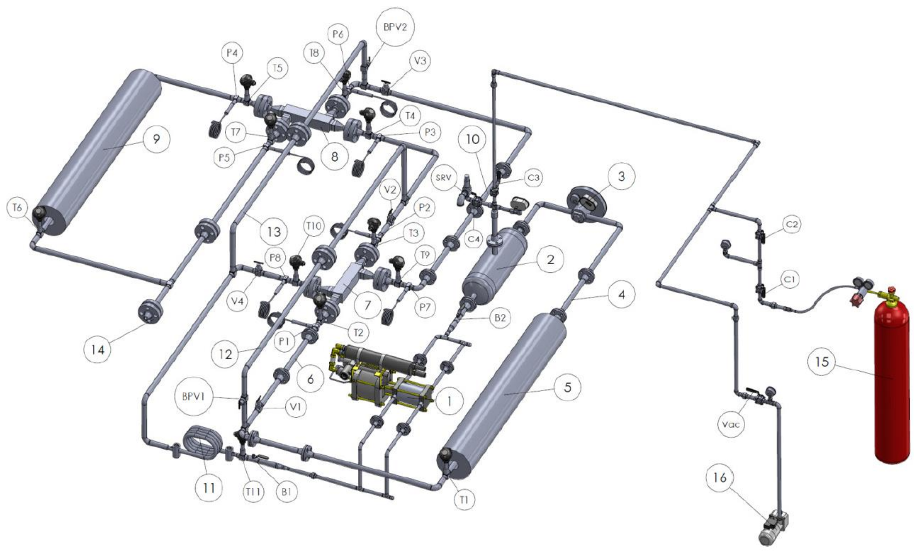

Balloon No.	Test Facility Component
1	Gas booster
2	Surge volume tank
3	Pressure reducing valve
4	Venturi flowmeter 1
5	Pre-heater
6	Venturi flowmeter 2
7	PCHE1
8	PCHE2
9	Main-heater
10	Venturi flowmeter 3
11	Cooler
12	Bypass 1
13	Bypass 2
14	Blind flange for future use
15	Helium gas cylinder
16	Vacuum pump
T1-T11	Thermowells
P1-P8	Pressure taps
V1-V4	Needle valves
BPV1, BPV2	Needle valves in bypass lines
B1, B2	Ball valves at gas booster inlet and exit
C1-C4	Ball valves in helium charging line
Vac	Ball valve in vacuum line
SRV	Safety relief valve

Figure 5.1. Layout of the High-Temperature Helium test Facility (HTHF)

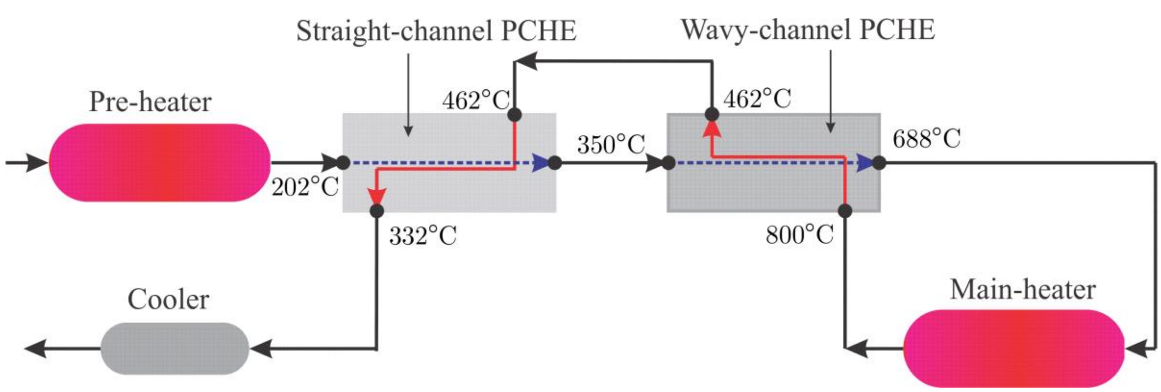

Figure 5.2. Schematic of the HTHF system design with heat exchangers included

The mass flow rate in the loop used for the steady-state operation is 26.5 kg/h. The powers of the pre-heater and main heater are 6.5 and 4.3 kW, respectively; and the heat rejection from the cooler to the chilled water is at most 10.8 kW. The printed circuit heat exchanger (PCHE) in figure 2 refers to an existing straight-channel PCHE, while the wavy-channel PCHE refers to the heat exchangers fabricated for this project. Temperatures shown in the figure are representative of the operating conditions during the testing of the heat exchangers.

5.1.2 High-Temperature Molten Salt Facility

The layout of the base configuration of the scaled-down high-temperature liquid fluoride salt facility at OSU is shown in Figure 5.3. This multipurpose facility is used for various projects. The base configuration indicates its use for reactor auxiliary cooling via DHX (Direct Reactor Auxiliary Cooling System Heat Exchanger) and NDHX (Natural Draft Heat Exchanger). The facility was modified for IHX testing as described later in the report.

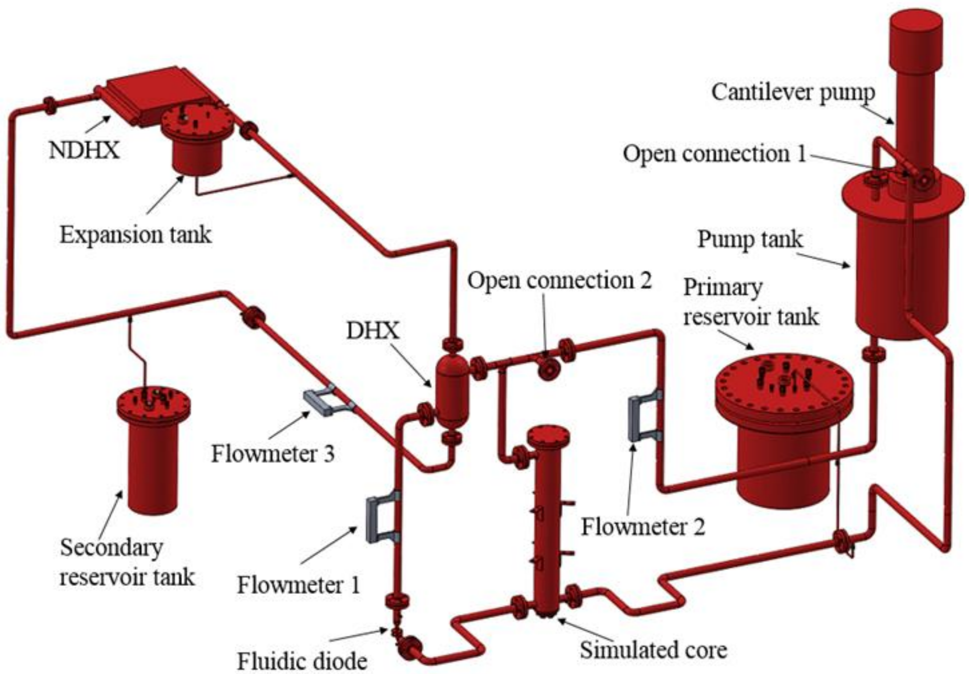

Figure 5.3. 3D Layout of the high temperature molten salt test facility

This facility is designed to for handling fluoride salts. Two different salts can be used in the system. The facility can also handle most other fluids unless there is a materials compatibility issue between the fluids and the material of construction. The other key component of the loop is the heater core, which is rated nominally at 70 kW.

5.2 Design and Fabrication of Heat Exchangers

5.2.1 Wavy Channel PCHE

5.2.1.1 Prototype Design

The operating conditions for the experimental prototype wavy-channel PCHE were defined by the HTHF capabilities shown in Table 5.1.

Table 5.1. HTHF Capability and Operating Conditions

	Hot Channel		Cold Channel	
Parameters	In	Out	In	Out
Nominal Duty [kW]	20.00			
Fluid	Helium		Helium	
T [°C]	800	452.1	326.1	674
P [MPa]	3	2.95	2.45	2.4
$\dot{m}$ [kg/h]	40		40	
ρ [kg/m^3]	1.3416	1.9970	1.9963	1.2586
c_p [kJ/kg-K]	5.193	5.193	5.193	5.193
μ [10^5 kg/m-s]	4.6869	3.5516	3.1370	4.3172
k_f [W/m-K]	0.3746	0.2802	0.2464	0.3435
Prandtl Number	0.6711	0.6749	0.6766	0.6722

The detailed procedure for designing a wavy channel PCHE was described earlier in section 2. The prototype design presented in section 2 was refined to take into account the fabrication considerations from the vendor and the resulting design is shown in Table 5.2.

Table 5.2. Helium-Helium PCHE Experimental Prototype Design Results

	Wavy-Channel	
Parameters	Hot	Cold
ϕ, [deg]	15	
Duty [MW]	19.5	
ΔT_{LMTD} [°C]	126	
A_h [m^2]	0.1288	
Reynolds number	1636	1920
ΔP [kPa]	19.56	25.93
Nusselt number	8.93	9.64
h [W/m^2-K]	2503	2306
U [W/m^2-K]	1200	
Channel Diameter [mm]	2	
Number of Plates	22	
Number of Channels	11	
Core width [cm]	2.75	
Core length [cm]	20	
Plate thickness [m]	1.63	
Compactness [m^2/m^3]	1306	

5.2.1.2 Fabrication

Figure 5.4 shows the detailed features of both the cold and hot side plates of the PCHE. The cross section of the fluid passages is approximately semi-circular with a diameter of 2 mm and a pitch of 2.5 mm. The shape of the flow passage is wavy, and the angle between the flow direction and the edge of block is 15 degree, as shown in Figure 5.4. The PCHE is designed in such way that each side can withstand the maximum design pressure of 3 MPa of HTHF.

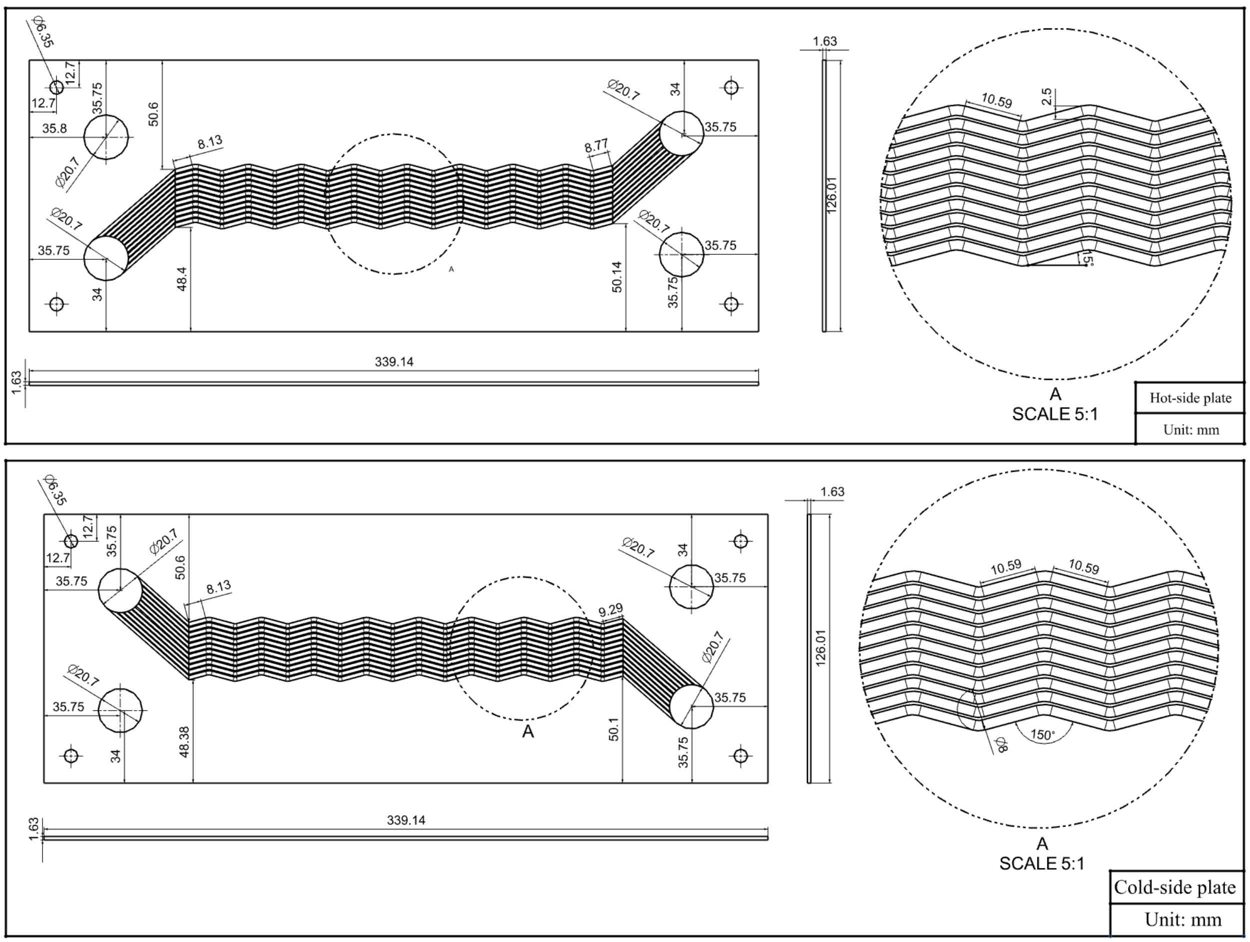

Figure 5.4. Geometry of the wavy-channel PCHE cold and hot side plates.

Figure 5.5 shows an exploded view and schematic of the PCHE. A total of eight holes are designed in each plate. Four of them with a diameter of 20.7 mm are used to direct the flow into the channels. At the topmost plate, those four larger holes are connected with four headers. Another four holes with a diameter of 6 mm are used for alignment during the diffusion bonding process by inserting four pins into the four smaller holes to prevent the plates sliding when adding large load on to the PCHE block surface.

The dimensions of the PCHE block shown in Figure 5.4 were 12 inches in length by 4.4 inches in width, and 2.35 inches thick. The thicknesses of the topmost plate and bottommost plate was both 0.5 inch. The topmost plate provides a strong base for joining the four headers. The headers are made from 1 inch NPS pipes since the piping size in the test facility is 1 inch NPS (corresponding to a pipe schedule of 160).

The flow passages in each plate of the PCHE were made by applying a photochemical etching technique, which uses strong chemical etchants to remove unwanted work piece material on the surface of the plates by controlled dissolution. All eight holes in the plates and the spaces between the channels and 20.7 mm-diameter holes were also made during this chemical etching process.

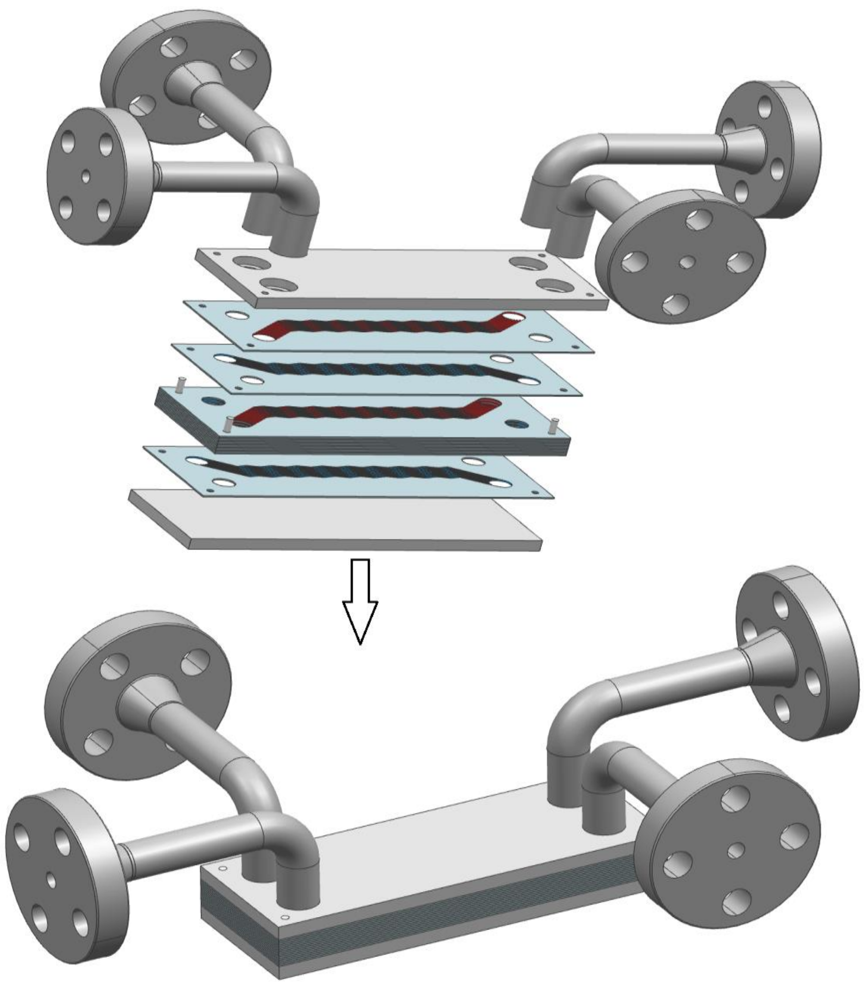

Figure 5.5. The exploded view and schematic of the PCHE

After the channels were photochemically etched on the plates, they were stacked alternately together and put in a furnace for diffusion bonding. Diffusion bonding is a solid-state joining technique, making a monolithic joint at the atomic level. Three bonding variables should be considered for a successful diffusion bonding, namely, bonding temperature, bonding pressure, and bonding time. The bonding temperature is typically lower than the melting temperature of the plate material. The bonding pressure ensures a tight contact between the mating surfaces and should be high enough for metal to creep (Mylavarapu, 2011).

Figure 5.6 shows a picture of the diffusion bonded stack and channel inlets on the plates. The inlet channels were lined and inlet recession surface smoothed. Four inlet-outlet headers were brazed on the PCHE while the plates were diffusion bonded to protect the integrity of the diffusion bonded block and brazed joints. Figure 5.7 shows the final fabricated wavy-channel PCHE that was installed in the HTHF.

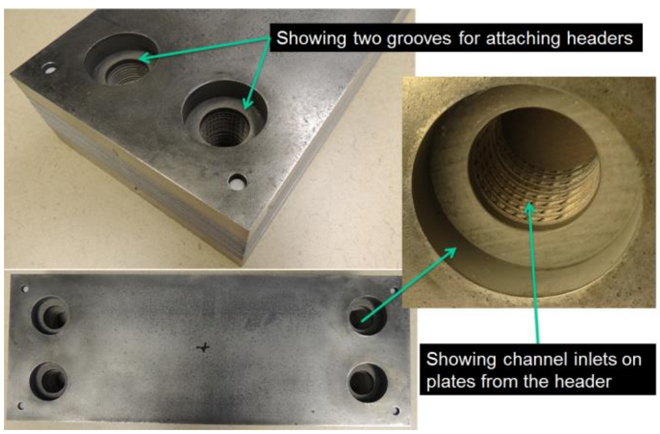

Figure 5.6. Photographs of the diffusion bonded stack and channel inlets on plates

Figure 5.7. PCHE assembly with four headers

5.2.2 Helically Coiled Twisted Tube Heat Exchanger

5.2.2.1Prototype Design

The heat exchangers utilize a twisted tube configuration with a surface feature that is believed to enhance convective heat transfer by inducing swirl into the bulk flow and periodically disrupting the boundary layer. The heat transfer enhancement mechanisms of twisted tubes combine features of several elements such as fins and twisted tapes. The helically-coiled configuration is a significant enhancement feature that induces secondary flow to increase the heat transfer rate. With a no-baffle design, the flow is confined cross flow on the shell side in the helically-coiled configuration. The heat transfer and pressure drop characteristics of twisted tube (same as spirally-fluted tube) were comprehensively studied by Arnold et al. at The Ohio State University. The design is conducted extrapolating the procedure by Garimella and Christensen, which is briefly presented in the flow chart as shown in Figure 5.8.

<u>Correlations: Tube Side</u>

As for the pressure drop calculations on the tube side, the friction factor can be calculated by:

$$f = \frac{64}{\mathrm{Re}-45.0}\left(0.554e^{*0.384}p^{*(-1.454+2.083e^{*})}\theta^{*-2.426}\right) \quad (100 \le \mathrm{Re} \le 1500)$$

$$f = 1.209\mathrm{Re}^{-0.261}\left(e^{*(1.26-0.05p^{*})}p^{*(-1.660+2.033e^{*})}\theta^{*(-2.699+3.67e^{*})}\right) \quad (\mathrm{Re} \ge 3000)$$

As for the heat transfer calculations on the tube side, the Nusselt number can be calculated by:

$$\mathrm{Nu} = 0.014\mathrm{Re}^{0.842}(e^{*-0.067}p^{*-0.293}\theta^{*-0.705}\mathrm{Pr}^{0.4}) \quad (500 \le \mathrm{Re} \le 5000)$$

$$\mathrm{Nu} = 0.064\mathrm{Re}^{0.773}(e^{*-0.242}p^{*-0.108}\theta^{*0.599}\mathrm{Pr}^{0.4}) \quad (5000 \le \mathrm{Re} \le 80000)$$

These range of validity for the above equations is defined in terms of the dimensionless parameters as shown below:

$$0.11 \le e^{*} \le 0.42; 0.41 \le p^{*} \le 7.29; 0.28 \le \theta^{*} \le 0.65$$

<u>Correlations: Shell Side</u>

Confined-flow models are selected for shell side pressure drop and heat transfer calculating. As for the pressure drop calculations on the shell side, the friction factor can be calculated by:

$$f = 20.57p^{*(1.089-1500e^{*})}Re^{-0.463}Nt^{-0.351} \quad (250 \le \mathrm{Re} \le 6350)$$

As for the heat transfer calculations on the shell side, the Nusselt number can be calculated by:

$$Nu = 20.388 Nt^{-0.617} Re^{0.36} e^{*0.703} p^{*-0.68e^{*}} Pr^{0.303} \quad (250 \le Re \le 6350)$$

These two equations are only valid for:

$$0.74 \le e^{*} \le 1.24; 0.92 \le p^{*} \le 8.73; 3 \le Nt \le 5; 6 \le Pr \le 12$$

Dimensionless numbers

$$e^{*} = \frac{e}{D_{vi}};\ p^{*} = \frac{p}{D_{vi}};\ \theta^{*} = \frac{\theta}{90};\ r^{*} = \frac{D_{vo}}{D_{vi}}$$

where D_b is the bore diameter, D_e is the envelope diameter, D_v is the volume-based diameter, e is the fluted depth, p is the fluted pitch, and θ is the flute helix angle.

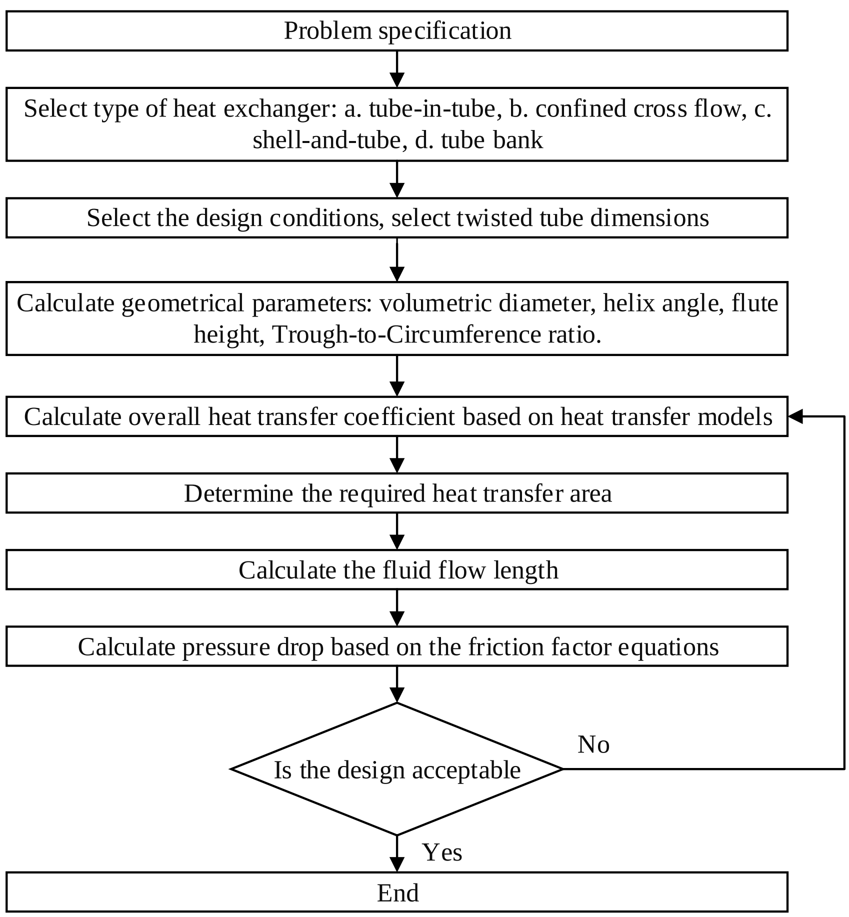

Figure 5.8. General twisted tube heat exchanger thermal design flow chart

Table 5.3 lists some parameters of the designed helically-coiled heat exchanger for liquid salt-liquid salt application. The shell-side diameter was selected to be 0.2 m, the tube length about 3.85 m and the actual heat exchanger height 0.21 m. The overall thermal capacity of the heat exchanger was 15 kW. Pressure drops on both the hot and cold sides were 11 and 4.6 kPa, respectively.

Table 5.3. Helically-coiled twisted tube heat exchanger for liquid salt-liquid salt application

Thermal duty (kW)	15.0	Average tube length (m)	3.85
Tube-side inlet temperature (°C)	722	Number of helical coil turns	7
Tube-side outlet temperature (°C)	707	Overall heat transfer area (m^2)	0.26
Shell-side inlet temperature (°C)	680	Heat exchanger height (m)	0.21
Shell-side outlet temperature (°C)	695	Shell inner diameter (m)	0.2
Tube-side mass flow rate (kg/s)	0.53	Tube-side Reynolds number	1.2×10^4
Shell-side mass flow rate (kg/s)	0.53	Shell-side Reynolds number	321
LMTD (°C)	27.0	Tube-side HTC (FLiNaK) (kW/(m^2-K))	7.1
Number of fluted tube coil	1	Shell-side HTC (FLiNaK) (kW/(m^2-K))	3.5
Outside envelope tube diameter (mm)	28.7	Overall HTC (kW/(m^2-K))	2.1
Outer bore tube diameter (mm)	16.9	Tube-side pressure drop (kPa)	11.0
Tube wall thickness (mm)	0.7	Shell-side pressure drop (kPa)	4.6

The second helically-coiled twisted tube heat exchanger was designed for liquid salt-air application. Compared to the first heat exchanger (i.e., the one for liquid salt-liquid salt application), the second heat exchanger has much small overall heat transfer coefficient due to the low heat transfer capability of air on the shell side. A heat exchanger with small heat transfer coefficient requires a large heat transfer area to accommodate the same thermal duty. Therefore, two coils were selected to reduce the overall heat exchanger height. The detailed parameters of the air heater are listed in the Table 5.4. The required thermal duty of the air heater is 40 kW and the overall heat transfer coefficient is 230.3 W/(m^2-K). The design tube-side and shell-side pressure drops were 4836.9 Pa and 210.5 Pa, respectively. The total length of the two twisted tubes was 3.091 m.

Table 5.4. Helically-coiled twisted tube heat exchanger for liquid salt-air application (air heater)

Thermal duty (kW)	40.0	Air free-flow area (m^2)	0.0147
Tube-side inlet temperature (°C)	722	Tube-side Reynolds number	6279
Tube-side outlet temperature (°C)	680	Shell-side Reynolds number	4300
Shell-side inlet temperature (°C)	30	Tube-side Nusselt number	107.0
Shell-side outlet temperature (°C)	400	Shell-side Nusselt number	97.0
Tube-side mass flow rate (kg/s)	0.51	Tube-side HTC (kW/(m^2-K))	5.545
Shell-side mass flow rate (kg/s)	0.11	Shell-side HTC (kW/(m^2-K))	0.243
LMTD (°C)	467	Required heat transfer area (m^2)	0.37
Inner shell outer diameter (m)	0.14	Overall HTC ((kW/(m^2-K))	0.23
Outer shell inner diameter (m)	0.26	Total tube length (m)	3.091

Number of tube coils	2	Number of helical coil turns	4.8
Outside envelope tube diameter (mm)	28.7	Heat exchanger height (m)	0.14
Outer bore tube diameter (mm)	16.9	Tube-side pressure drop (kPa)	4.8369
Tube-side inlet velocity (m/s)	0.51	Shell-side pressure drop (kPa)	0.2105
Shell-side inlet velocity (m/s)	6.3		

5.2.2.2 Fabrication

Both the heat exchangers were fabricated by vendors specializing in the fabrication of such equipment. It should be noted that fabrication of these heat exchanger is relatively straightforward compared to that of the compact heat exchangers involving photochemical etching and diffusion bonding. Figure 5.9 shows some pictures of the helically-coiled twisted tube heat exchanger. The top-left picture shows the helical coil whose two ends were weld a 90° elbow. The top-right 3-D drawing shows the inside structure view of the heat exchanger. Three supporting legs and one venting tube can be seen clearly. The bottom picture shows the actual heat exchanger after fabrication. Two tube fittings for temperature and pressure measurements were welded on each of the inlet/outlet pipe.

Figure 5.9. Helically-coiled twisted tube heat exchanger

Figure shows an assembly drawing of the second heat exchanger indicating the flow path of the liquid fluoride salt with entrance to the heat exchanger core through the 1-1/2" pipe and flange to the coils from the inlet cap through the tube sheet to the exit from the coils through the tube sheet, collection in the outside of the cap and exit of the heat exchanger by means of the 1-1/2" pipe and flange. Three legs on the inner side of the tube sheet are used for supporting the inner shell. These legs will be made from 1/4''

Stainless Steel rod. Two small holes on both ends of the inner shell caps, whose purpose is to relieve pressure, would be approximately 3/8" in diameter. Figure 5.11 shows the coils and coil arrangement. Figure 5.12 shows the complete heat exchanger configuration. The coil parameters are listed as follows:

a. Coil #1: Straight twisted tube length for the coil: 2.71 m, not including the smooth sections at the both ends. Coil diameter: 172 mm, number of turns: 5.5

b. Coil #2: Straight twisted tube length for the coil: 3.67 m, not including the smooth sections at the both ends. Coil diameter: 233 mm, number of turns: 5.5

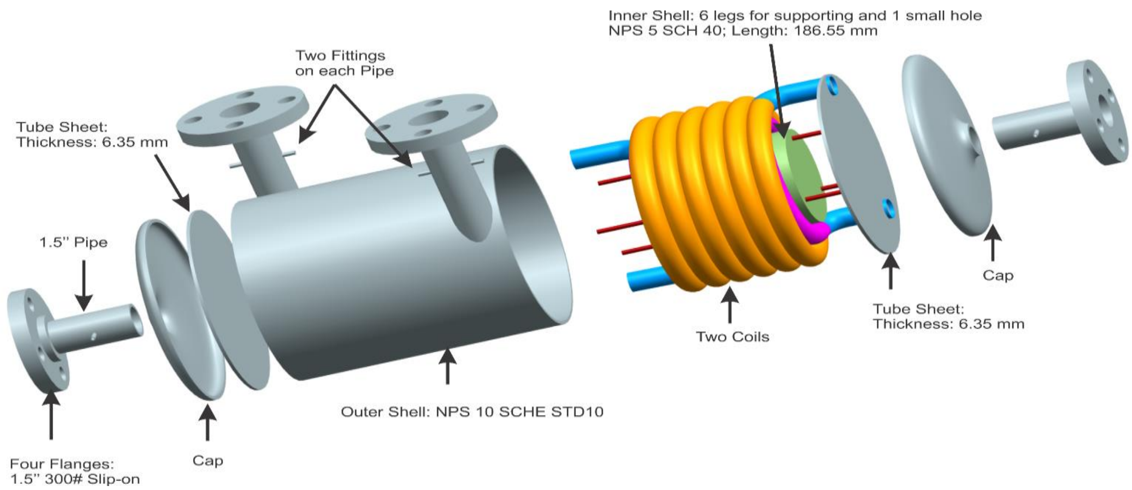

Figure 5.10. Exploded view of the heat exchanger

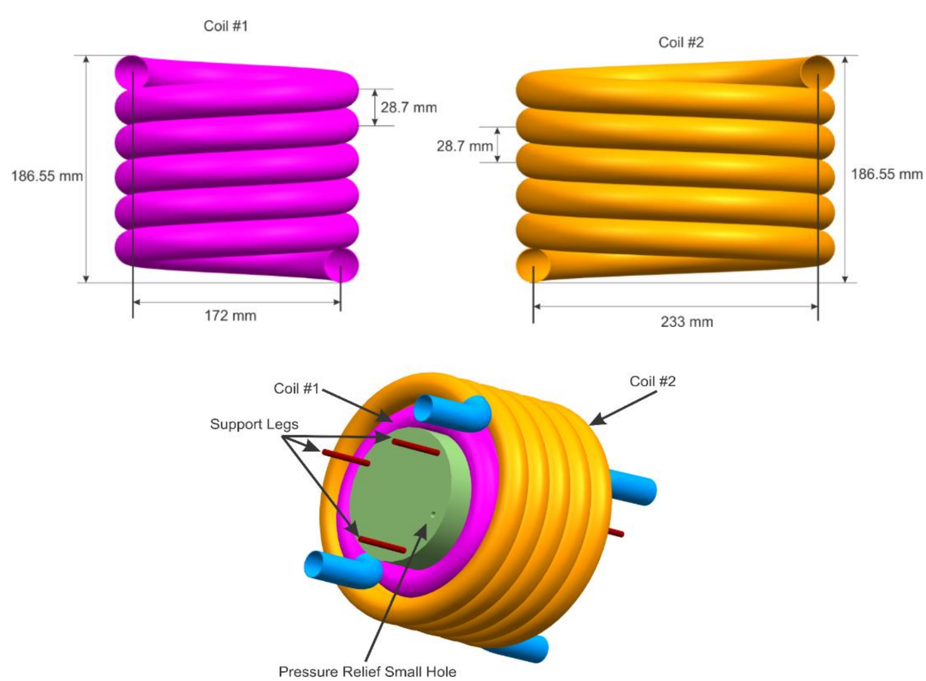

Figure 5.11. Coils and coil arrangement

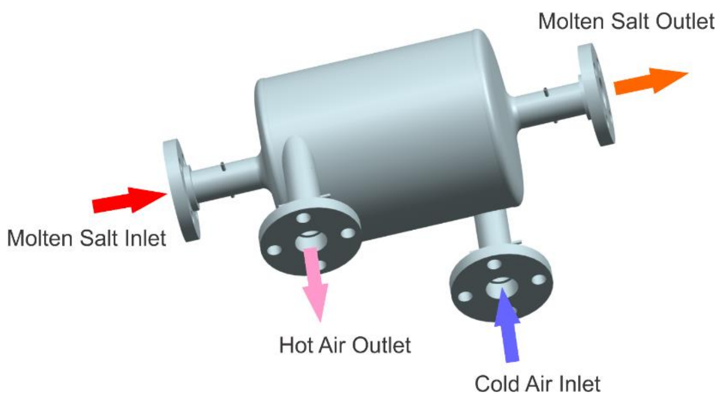

Figure 5.12. Complete heat exchanger configuration

5.2.3 Straight-Channel PCHE

Experiments were also conducted using an existing straight channel PCHE made of 1.6-mm thick Alloy 617 plates for the heat exchanger core and Alloy 800H pipes for the headers. A total of 10 hot plates and 10 cold plates were diffusion bonded together to form a metal block with 12 straight channels in each plate. Figure 5.13 shows one hot-side plate and one cold-side plate and Table 5.5 lists the basic geometric parameters of the fabricated PCHE. The shape of the straight flow channel is approximately semicircular with a diameter of approximately 2 mm and a pitch of 2.54 mm in the span-wise direction. The PCHE was designed in such a way that each side could withstand the maximum pressure of 3 MPa in the High-temperature Helium Test Facility (HTHF). The actual PCHE assembly with four headers is shown in Figure 5.14. The dimensions of the PCHE block were 305 mm in length by 102 mm in width by 73 mm in height.

Table 5.5. Summary of the reduced-scale PCHE parameters

Parameter	Hot side	Cold side
Channel pitch, mm	2.54	2.54
Channel width, mm	2.0	2.0
Plate thickness, mm	1.63	1.63
Channel travel length, mm	305	272
Number of plates	10	10
Number of channels in each plate	12	12

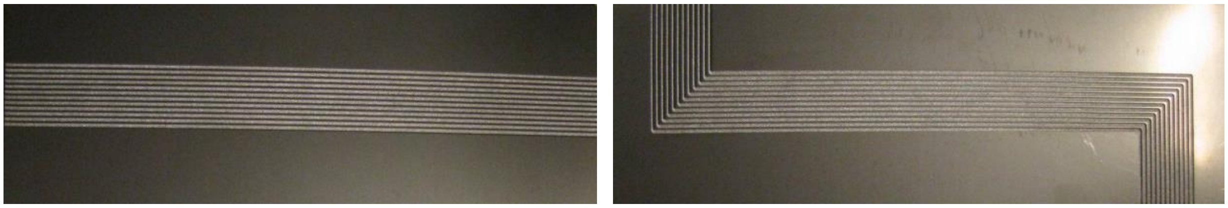
Figure 5.13. One cold-side plate (left) and one hot-side plate (right).

Figure 5.14. PCHE with four headers assembled.

The mathematical model for the straight channel PCHE is essentially identical to the one described above and is not repeated here for the sake of brevity. Similarly a nodalization sensitivity steady conducted for this PCHE yielding identical results is also not repeated here. The details of these were reported earlier and are available in the report *3363_2016_Q2.pdf*.

5.3 Experimental Results

The modeling and simulation of transients for the various heat exchangers was described in section 3. Experiments studies were conducted for verification and validation of the models and the results are described below.

5.3.1 Wavy-Channel PCHE

Three sets of transient tests were experimentally carried out to validate the dynamic model. For the first case, the only variation is the hot-side inlet temperature. The second case involved changes in both the hot-side and cold-side inlet temperatures. Three variations were simultaneously applied to the third transient test, namely, the hot-side inlet temperature, the cold-side inlet temperature, and the helium mass flow rate step increases on both sides. Referring to the schematic of the experimental set up (Figure 5.2), temperature transient tests were performed by changing the temperature controllers' setting points on the two heaters. Flow rate changes were effected by adjusting the drive-air flow rate or drive-air inlet pressure or both. Both operations were simultaneously applied to the third transient test.

5.3.1.1 Change the hot-side inlet temperature only

The heat exchanger inlet temperature step increases are not applicable in the current study due to the limited heater capability and configuration of the HTHF. In the HTHF, helium flow rates are controlled by a gas booster and temperature is governed by the two electric heaters. Although a temperature step increase or decrease is not readily achievable, temperature variations could be captured during experiments via the data acquisition system. After the PCHE reached a steady state condition, temperature variations at the inlet of the PCHE hot side were introduced at around 850 seconds by controlling the main-heater power via the temperature controller in the HTHF as shown in Figure 5.15. During this transient test, the cold-side inlet temperature and mass flow rates on both sides were kept at constants of 94.5ºC and 30.5 kg/h, respectively. The fixed cold-side inlet temperature could be achieved by maintaining the pre-heater power while bypassing the straight-channel PCHE in the HTHF. Once the straight-channel PCHE is bypassed, the zigzag-channel PCHE cold-side inlet temperature is governed by the pre-heater and the hot-side inlet temperature is controlled by the main-heater. A polynomial function could be used to fit the hot-side inlet temperature curve and served as an input in the dynamic model. Figure 5.15 also presents the comparison of the hot-side inlet temperatures and the fitted function value. It can be seen that the fitted values follow the experimental data well. The outlet temperatures for both the hot and cold sides from the numerical simulation were compared to the experimental data, as shown in Figure 5.16. It is observed that the numerical results predict the experimental results well. There are offsets for both sides during the initial steady-state condition, which could be attributed to the heat loss from the heat exchanger surfaces under high-temperature conditions. The numerical simulation on the cold side slightly underpredicts the experimental value during the initial steady state. This could be because the cold side has less heat loss than the hot side. After a second steady state is reached, the hot-side numerical and experimental results are in good agreement. Compared to the experimental results, PCHE outlet temperature differences for the initial and final steady state have deviations of 10.1% and 6.5%, respectively. Cold-side outlet simulation results under predict the experimental results mainly due to the marginal deviations observed.

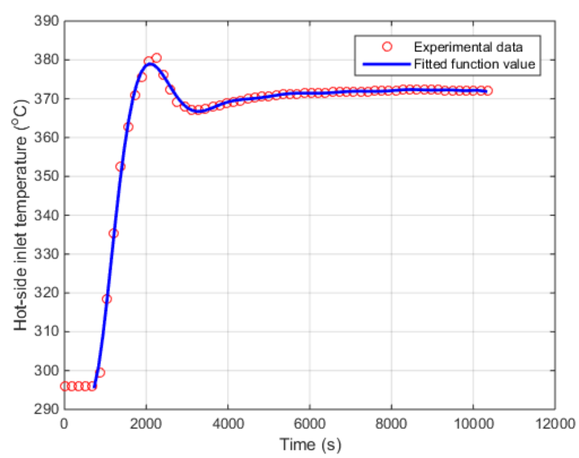

Figure 5.15. Hot-side inlet temperature profile and fitted curve.

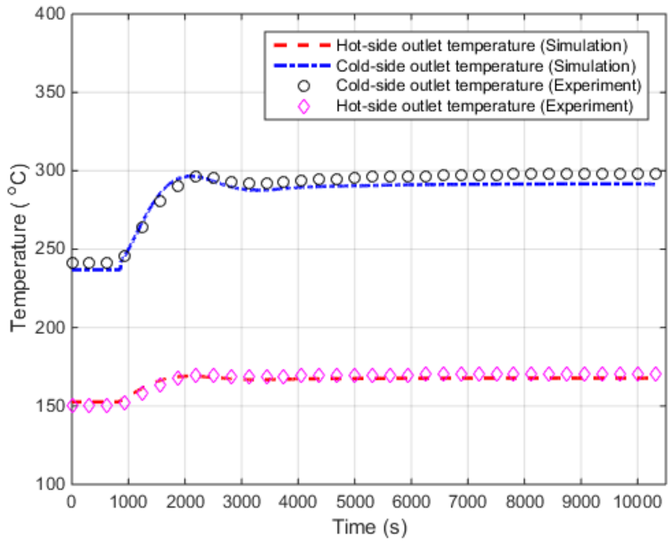

Figure 5.16. Outlet temperature profiles following hot-side inlet temperature variations.

5.3.1.2 Change both the hot-side and cold-side inlet temperatures

In the second transient test, the straight-channel PCHE was not bypassed. Since two PCHEs (i.e., straight-channel PCHE and zigzag-channel PCHE) are coupled in the HTHF, as shown in Figure 5.2, the cold-side inlet temperature would increase if the hot-side inlet temperature increases. Unlike the first case, two fitted functions instead of one for both inlet temperatures monitored in the experiment were fed into the dynamic model to simulate outlet temperature trends. The fitted polynomial functions predict the experimental data well for both the hot-side and cold-side inlet temperatures, as can be seen in Figure 5.17. From the figure, the hot-side inlet temperature increases from 767 to 802ºC and maintains at 802ºC for more than one hour, which represents one of the VHTR typical operation conditions. Comparison of the outlet temperatures obtained from experiments and numerical simulations is shown in Figure 5.18. The cold-site outlet numerical results predict the experimental data well with 0.2ºC overpredicting. Due to large heat loss from the hot side, the numerical model overpredicts the experimental results by 9ºC during the initial steady state and by 2.5ºC during the final steady state. Compared to the experimental results, PCHE outlet temperature differences for the initial and final steady state have deviations of 6.6% and 4.1%, respectively. Although the numerical model slightly overpredicts the experimental results on the hot side, it gives a conservative result on the reactor primary side.

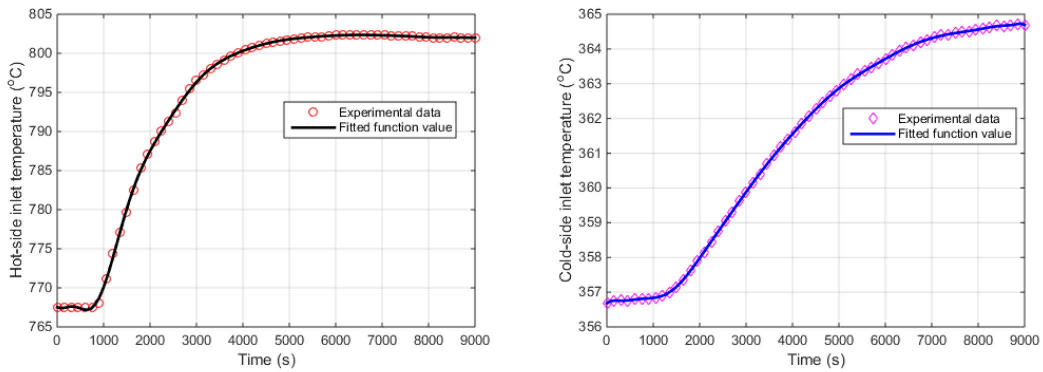

Figure 5.17. Hot-side and cold-side inlet temperature profiles and fitted function value.

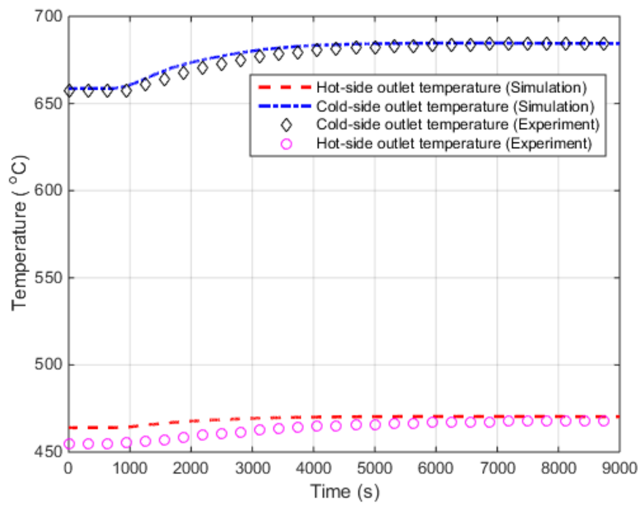

Figure 5.18. Outlet temperature profiles following inlet temperature variations.

5.3.1.3 Helium mass flow rate step change with inlet temperature variations

For the third transient test, three variations were simultaneously applied, namely, the hot-side inlet temperature, the cold-side inlet temperature, and the helium mass flow rate step increases on both sides. The hot-side inlet temperature was raised from 724 to 768.7ºC. As mentioned, the cold-side inlet temperature would change accordingly due to the two coupled PCHEs in the HTHF. Simultaneously, the helium mass flow rate decreased from 35.3 to 31.8 kg/h at around 700 seconds and increased from 31.8 to 34.7 kg/h at about 4,700 seconds, as shown in Figure 5.19. There are some variations in the flow rate, but the standard deviation of each operated flow rate stage is less than 1%. The fitted polynomial functions values and the experimental data for both the hot-side and cold-side inlet temperatures are shown in Figure 5.20. It is clearly seen that the fitted temperature function values follow the experimental trends well. Comparison between numerical results and experimental data shows that there are some discrepancies at the initial condition, however, the numerical results follow the experimental trends well and are in a good agreement with the experimental data in the final steady state as can be seen in Figure 5.21. Compared to the experimental results, PCHE outlet temperature differences for the initial and final steady state have deviations of 6.5% and 2.6%, respectively.

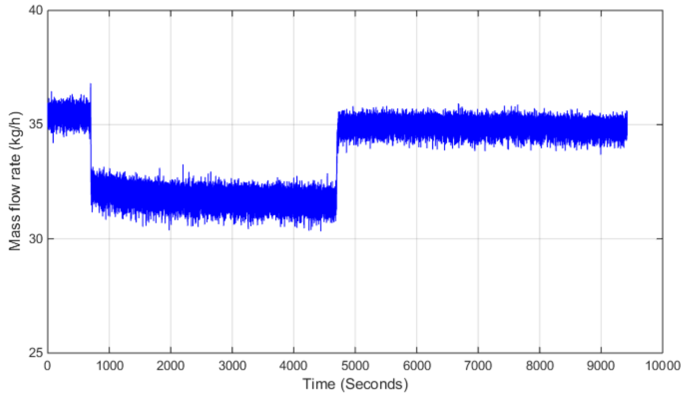

Figure 5.19. Helium mass flow rate step changes.

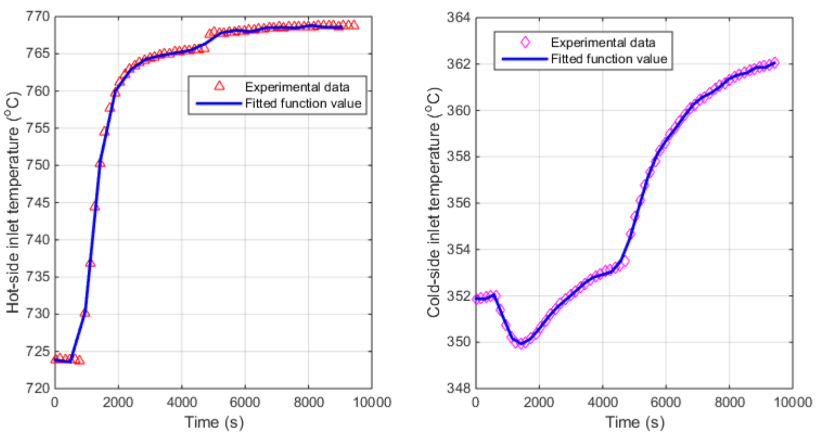

Figure 5.20. Hot-side and cold-side inlet temperature profiles and fitted function value.

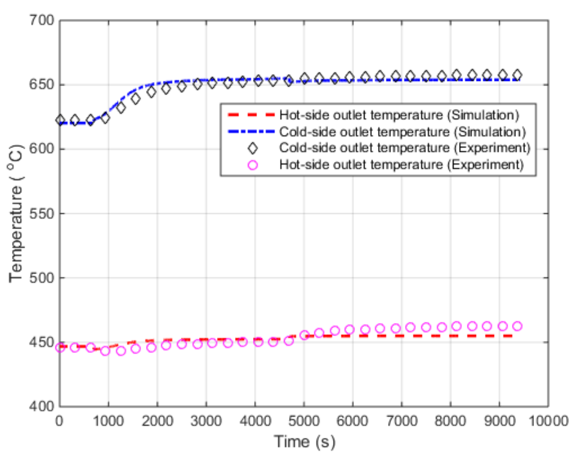

Figure 5.21. Outlet temperature profiles following inlet temperature variations.

Based on the above three transient tests, the close agreement of the numerical results with the experimental data was achieved. While there are some discrepancies, it is clearly seen that the numerical solutions are sufficiently accurate and conservative, and that the dynamic model developed for predicting both steady-state and transient performances of the reduced-scale zigzag PCHE has been validated.

5.3.2 Straight Channel PCHE

Two sets of transient tests were experimentally carried out to assess the applicability of the dynamical model, namely, the test PCHE subject to inlet temperature increase and decrease on the hot side. A temperature step change on the heat exchanger's inlets is not applicable in the current study due to the limited heater capability and the configuration of the HTHF. For experiments carried out in the HTHF, helium mass flow rates were controlled by a gas booster and temperatures were governed by the two electric heaters. Although a temperature step increase or step decrease was not readily achievable, the two heaters' outlet temperatures can be adjusted by changing the temperature controllers' setting points and temperature variations could be captured during the test in the data acquisition system. The hot-side inlet temperature was increased for the first test and decreased for the second test. Cold-side inlet temperatures were maintained at constant values for both experiments. After the PCHE reached a steady state in both experiments, temperature variations at the inlet of the hot side were introduced by controlling the main-heater power via the temperature controller in the HTHF to initiate transients.

5.3.2.1 Increase in the temperature of hot-side inlet stream

During the hot-side temperature increase transient testing, the cold-side inlet temperature and helium mass flow rates on both sides were kept constants at 49.9ºC and 31.7 kg/h, respectively. A polynomial function was used to fit the hot-side inlet temperature data points and was implemented in the dynamic model. Figure 5.22 presents the comparison of the hot-side inlet temperatures and the fitted function value. The outlet temperatures for both the hot and cold sides obtained from the numerical simulation were compared to the experimental data, as shown in Figure . It was observed that the numerical results predicted the experimental trends well. There were some offsets for both outlet temperatures during the initial steady-state condition, which could be attributed to the heat loss from the heat exchanger surfaces. The numerical results on both sides slightly over predicted the experimental value during the initial steady state. After the second steady state was reached, the hot-side temperatures obtained from the dynamic model and experiments were within a good agreement. Compared to the experimental results, outlet temperature differences for the initial and final steady states had deviations of 2.8 and 9.3%, respectively.

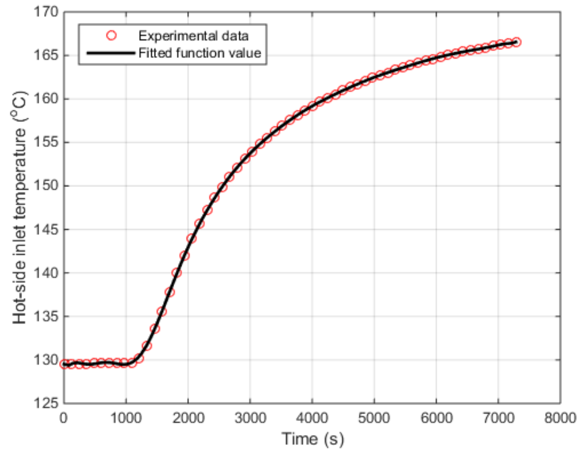

Figure 5.22. Hot-side inlet temperature profile and the fitted curve.

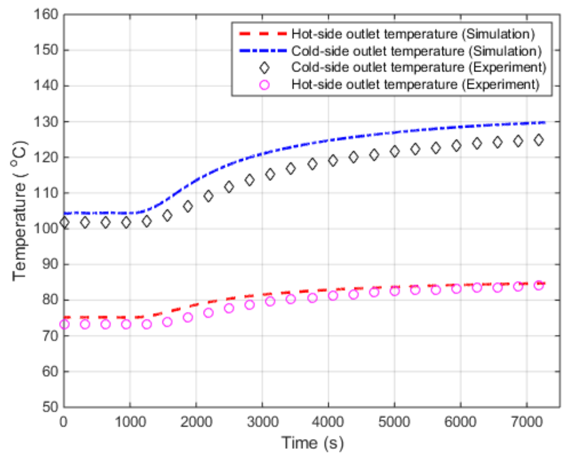

Figure 5.23. Outlet temperature profiles following the hot-side inlet temperature increase.

5.3.2.2 Increase in the temperature of hot-side inlet stream

Similar analysis methodology was applied to the second transient test. The hot-side inlet temperature and the fitted curve were compared as shown in Fig 5.24. The outlet temperatures for both the hot and cold sides from the numerical simulation were compared to the experimental data, as shown in Figure . It was observed that the numerical results also predicted the experimental trends well. However, there were some discrepancies, which also could be attributed to the heat loss from the heat exchanger surfaces. Compared to the experimental results, outlet temperature differences for the initial and final steady states had deviations of 5.1% and 3.1%, respectively.

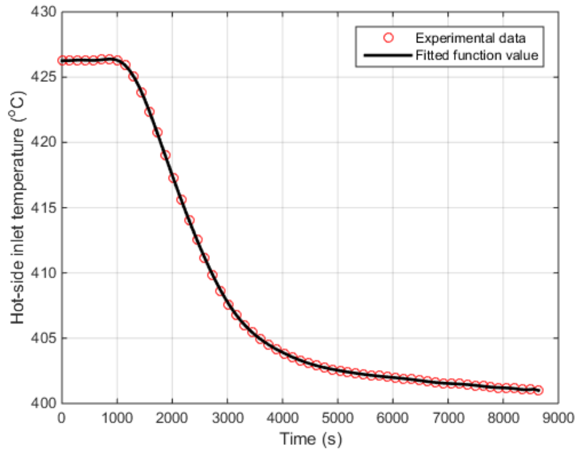

Figure 5.24. Hot-side inlet temperature profile and the fitted curve.

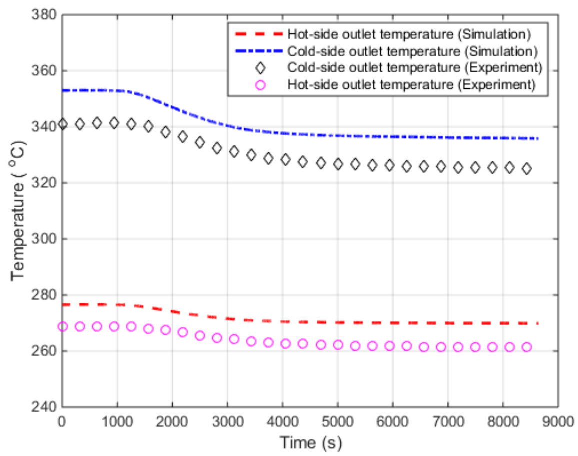

Figure 5.25. Outlet temperature profiles following the hot-side inlet temperature decrease.

5.3.3 Helically-Coiled Heat Exchanger

5.3.3.1 Facility Modification

The second facility (high temperature molten salt loop) described earlier in the report was modified slightly to accommodate the two helically-coiled fluted tube heat exchangers. Figure 5.26 shows a schematic of the existing test loop (shown in the blue box) with an additional test section (showing in the red box). The additional test section added was made in such way that it can be isolated by two valves (valves #4 and 5) from rest of the loop when performing low-temperature DRACS tests. Figure 5.27 is a photograph of the modified test loop with the additional test section. During the heat exchanger testing, valves #1, 2 and 3 are closed. Experiments were conducted using water in this test loop. Water is pumped through the simulated core and then heated to a certain temperature. The heated water flows through the test heat exchanger tube side, serving as the hot-side fluid. On the other hand, city water is filtered and directed into the cold side of the heat exchanger (i.e., the shell side). Four thermocouples were installed at the inlets and outlets of the heat exchanger to measure the four end temperatures. Two differential pressure transducers were installed to measure the differential pressure across each side of the heat exchanger. The volumetric flow rates on both sides of the test heat exchanger were measured by two clamp-on ultrasonic flow meters.

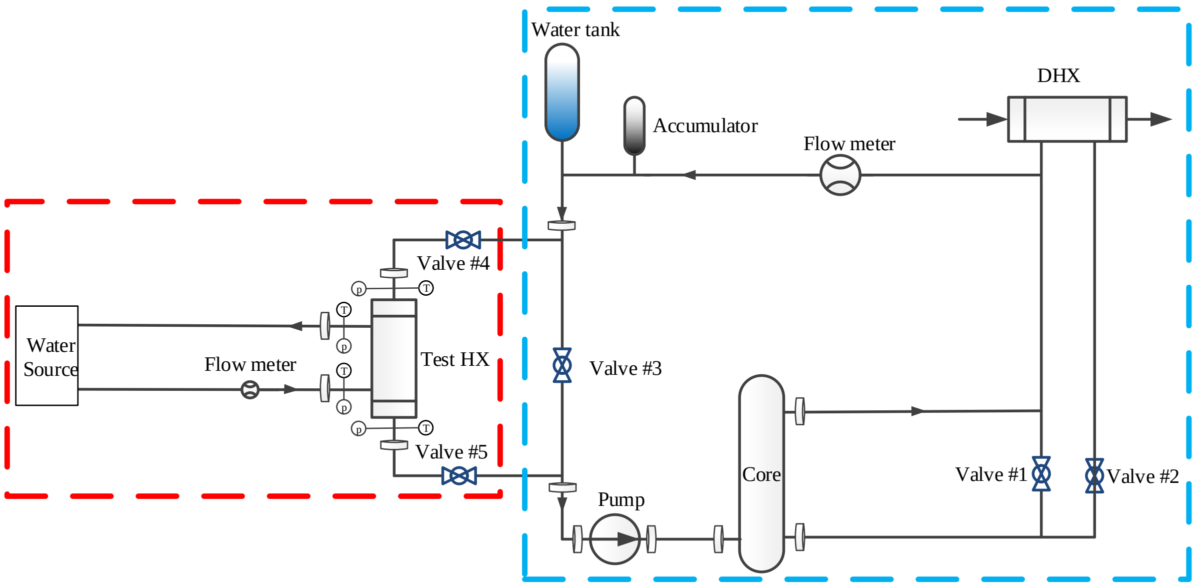

Figure 5.26. Schematic of the low-temperature water test loop with the additional test section.

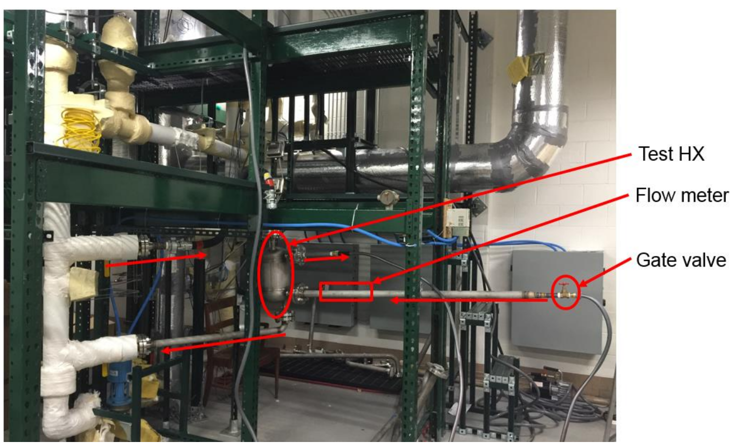

Figure 5.27. Photo of the modified test loop with the additional test section.

5.3.3.2 Results and discussions

Only the helically-coiled fluted-tube heat exchanger designed for fluoride salt to fluoride salt applications was tested under the water to water conditions. The obtained pressure drops on both the shell and tube sides are shown in Figure 5.28. As can be seen from the figure, the pressure drops increase as the mass flow rates increase for both the shell and tube sides. As expected, the pressure drops on the tube side are much larger than those on the shell side since the free-flow area on the tube side is much smaller, resulting in higher flow velocities. Pressure drops on tube side were future reduced. Figure 5.29 shows the comparison of friction factors obtained from experiments and Garimella and Christensen's model [4.2.1]. It can be seen that the experimental data follow the model trend well.

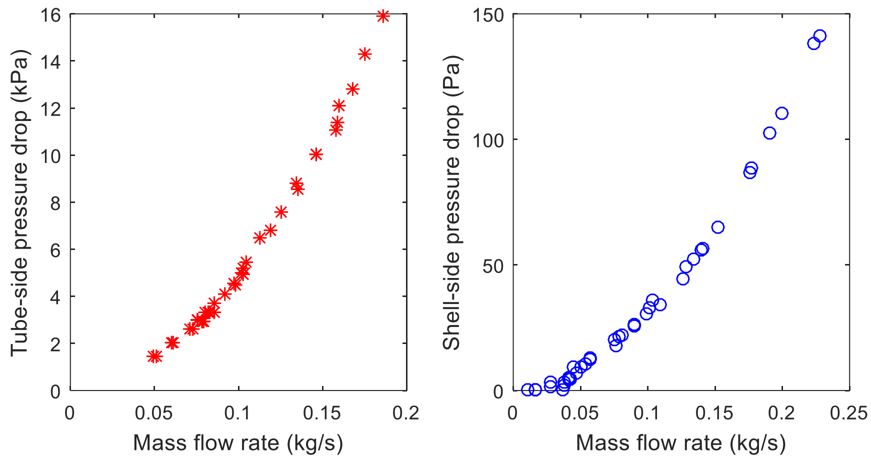

Figure 5.28. Pressure drops on both the tube and shell sides.

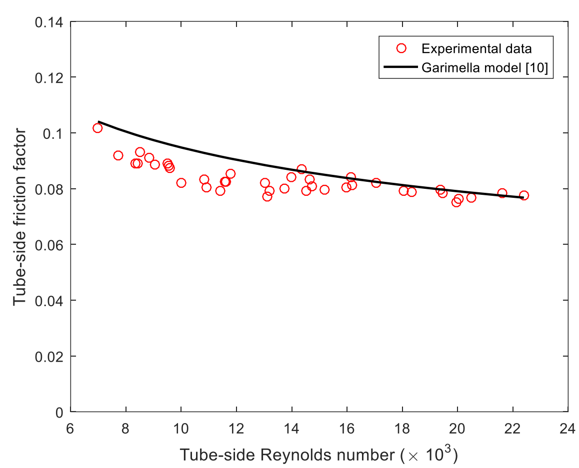

Figure 5.29. Tube-side friction factor.

Figure 5.30 shows the heat exchanger thermal duties under a variety of mass flow rates on both the shell and tube sides. The heat exchanger thermal duty for each steady state was calculated based on the average thermal duty on both the shell and tube sides. The maximum heat exchanger thermal duty reached 5.1 kW among these test conditions. The heat loss from the heat exchanger is defined as the thermal duty difference between the shell side and tube side of the heat exchanger. It can be observed from Figure that the ratios of heat loss to the heat exchanger thermal duty were generally less than 10% except for seven runs. Higher heat loss ratios typically occur when the temperatures are higher and the mass flow rates are smaller on both sides of the heat exchanger.

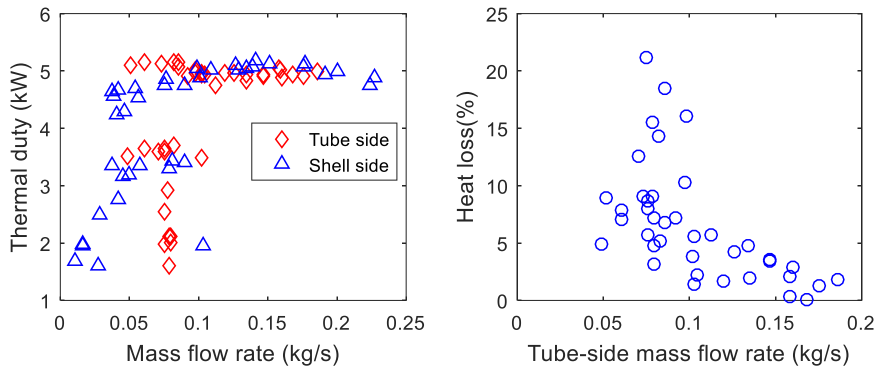

Figure 5.30. Heat exchanger thermal duty and heat loss.

For a countercurrent flow heat exchanger, the effectiveness of the heat exchanger can be computed by:

$$\varepsilon = \frac{1 - \exp(-NTU(1 - C^{*}))}{1 - C^{*}\exp(-NTU(1 - C^{*}))}$$

where NTU is the number of transfer unit and C^* the ratio of the smaller to larger heat capacity rates for the two fluid streams. NTU is a non-dimensional measure of the heat transfer size of the heat exchanger defined as:

$$NTU = \frac{UA}{\dot{m}c_p}$$

The overall heat transfer coefficient, U , specific heat capacity, c_p , and mass flow rate, $\dot{m}$, are determined by the operation conditions. Figure 5.31 presents the heat exchanger effectiveness as a function of NTU. Based on the theoretical calculations, the maximum NTU is about 4.05 in the current study, which gives the largest effectiveness value of 97.4% when C^* is 0.136, resulting in good agreement with the experimental data as shown in the figure. For a constant C^*, the heat exchanger effectiveness increases as NTU increases. The heat exchanger effectiveness decreases as C^* increases for the same NTU. As can be seen from Figure , there are a few experimental data points where the effectiveness decreases when the NTU increases, which is due to the increase of C^*. Figure 5.32 shows the overall heat transfer coefficients of the heat exchanger. It was found that the overall heat transfer coefficients of the helically-coiled fluted tube heat exchanger were three to four times those in the conventional shell-and-tube heat exchangers under water to water test conditions.

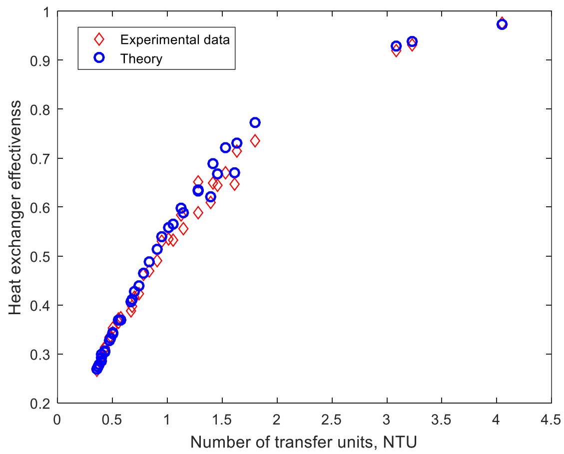

Figure 5.31. Heat exchanger effectiveness as a function of NTU.

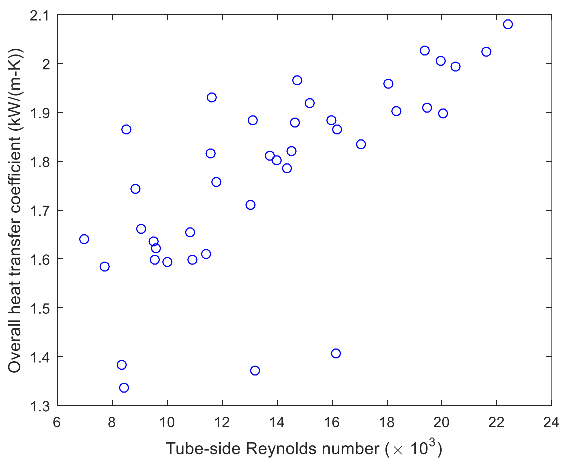

Figure 5.32. Overall heat transfer coefficient of the heat exchanger.

5.4 Summary

Prototype heat exchangers – wavy-channel printed circuit heat exchanger (PCHE) and helically coiled heat exchanger – were designed and fabricated for the study. These heat exchangers, as well as an available straight channel heat exchanger were installed in the experimental facilities at The Ohio State University and subjected to steady-state and dynamic testing. The dynamic tests involved introducing a process disturbance in terms of a change in temperature or flow rate of a stream (or streams), or a combination thereof. The response of the system was monitored through changes in the temperatures, and experimental data analyzed with respect to the thermal hydraulic characteristics. Dynamic models were also developed for the system and the response simulated by user-developed MATLAB codes. The simulation results were compared with the experimental data for validating the models. These comparisons indicate that the models are able to predict the system behavior reasonably well.

6. Conclusions

Advanced reactors derive their potential from their ability to provide, in addition to power generation, high-temperature heat that can be utilized for a variety of process applications including co-generation, conversion of coal to liquids and formulation of chemical feedstocks. The IHX is a critical component in the next generation nuclear plant system and an effective design of the IHX is essential for high efficiency operation. In addition, the transient behavior of IHX and the coupling between the reactor primary system and the secondary system (power conversion system and process heat application) is essential to the reactor safety and therefore is critical to regulators for design certification application. The complexity of the system requires development of advanced modeling and simulation tools to handle the interaction between the various components of the system during normal and off-normal operations, and validating the results through experimental observations.

The research conducted in this project has yielded information on the thermal designs and advanced control strategies for different IHX types for various combinations of coolants and operating temperatures and conditions. The transient behavior of the reactor-IHX-SHX system was simulated for various system disturbances, and the effectiveness of the control system to mitigate the adverse impacts of such events demonstrated clearly. The simulation results were compared with the experimental results, with the close agreement between the two indicating the validity of the theoretical models developed to describe the system. These results and information are valuable in understanding the coupled response of the reactor-IHX-SHX system to various transients and the development of intelligent control systems for the next generation nuclear reactor systems.

The results of the research have been presented at several national and international meetings of various professional societies, and published in refereed technical publications. The project has also resulted in mentoring of several graduate and undergraduate students, with two students graduating with graduate degrees in chemical and nuclear engineering. The project has thus also served to address the need for qualified, technical workforce for the nuclear field.

References

Al-Dawery, S., Alrahawi, A., Al-Zobai, K., 2012. Dynamic Modeling and Control of Plate Heat Exchanger. Int. J. Heat Mass Transfer, 55, 6873-6880.

Amin, M.R., Rocco, R., 2006. “Dynamic modeling of a closed loop Brayton cycle for space auxiliary electric power systems.” Proceedings of 3rd BSME-ASME International Conference of Thermal Engineering, Dhaka, Bangladesh, December 20-22, 2006.

Arnold, J., Garimella, S., Christensen, R.N., 1990. “A Manual for Heat Exchanger Design using Spirally Fluted Tubes,” The Ohio State University.

Bartel, N., Chen, M., Utgikar, V., Sun, X., Kim, I.-H., Christensen, R., Sabharwall, P., 2015. “Comparative analysis of compact heat exchangers for application as the intermediate heat exchanger for advanced reactors,” Ann. Nucl. Energy, 81, 143-149.

Chapra, S., Canale, R., 2010. “Numerical Methods for Engineers,” sixth ed., McGraw-Hill, New York.

Chen, M., Lv, Q., Kim, I.-H., Sun, X., Christensen, R., Utgikar, V., Sabharwall, P., 2015. “Dynamic analysis of a fluoride salt-cooled high-temperature reactor coupled to a helium Brayton power system via an intermediate loop,” Prog. Nucl. Energy, 83, 283-293.

Das, S., Pan, I., Das, A., 2013. “Fractional order fuzzy control of nuclear reactor power with thermal-hydraulic effects in the presence of random network induced delay and sensor noise having long range dependence,” Energy Conv. Manage., 68, 200-218.

Galvez, C., 2011. “Design and transient analysis of passive safety cooling systems for advanced nuclear reactors,” Doctoral dissertation, University of California.

Garimella, S., 1990. “Experimental Investigation of Heat Transfer and Pressure Drop Characteristics of Annuli with Spirally Fluted Inner Tubes,” Doctoral Dissertation, The Ohio State University.

Garimella, S., Christensen, R.N., 1995a. “Heat Transfer and Pressure Drop Characteristics of Spirally Fluted Annuli: Part I: Hydrodynamics,” J. Heat Transfer, 117, 54-60.

Garimella, S., Christensen, R.N., 1995b. “Heat Transfer and Pressure Drop Characteristics of Spirally Fluted Annuli: Part II: Heat Transfer,” Journal of Heat Transfer, 117, 61-68.

Gnielinski, V. 1983. “Forced Convection in Ducts,” in *Heat Exchanger Design Handbook*, Volume 2, Hewitt, G.F., Executive Ed., Hemisphere, New York

Guomin, C., Jinyang, W., Tao, J., Xiangbai, H., 2011. Transfer behavior of heat exchanger. Adv. Mater. Res., 233-235, 1281-1287. doi: 10.4028/www.scientific.net/AMR.233-235.1281.

Heng, X., 2011. “Model Development and Simulation of Transient Behavior of Helium Turbine System,” Ann. Nuc. Energy, 38, 2797-2805.

Hesselgreaves, J.E., 2001. “Compact Heat Exchangers: Selection, Design and Operation,” Gulf Professional Publishing.

Holcomb, D.E., Cetiner, S.M., Flanagan, G.F., Peretz, F.J., Yoder, G.L., Jr., 2009. "An Analysis of Testing Requirements for Fluoride Salt-cooled High Temperature Reactor Components," ORNL/TM-2009/297, Oak Ridge National Laboratory, November 2009.

Ishizuka, T., Kato, Y. Muto, Y., Nikiting, K., Ngo, T.L.,2006. "Printed Circuit Heat Exchanger Thermal-Hydraulic Performance in Supercritical CO2 Experimental Loop," Int. J. Refrig., 29, 807-814.

Jayakumar, J.S., 2013. "Helically Coiled Heat Exchangers" in Heat Exchangers - Basics Design Applications Edt| InTechOpen, InTech: Open Access Publisher [eBooks]. Retrieved at April 20, 2013, from the website Intech: Open Science | Open Minds at http://www.intechopen.com/books/heat-exchangers-basics-design-applications

Kakac, S., Liu, H., 2002. "Heat Exchangers: Selection Rating and Thermal Design," CRC Press, ISBN 0-8493-0902-6.

Kato, R., Nishihara, T., Kumitomi, K., 2007. "Design of the Intermediate Heat Exchanger for High Temperature Gas-Cooled Reactor Hydrogen Cogeneration System," Japanese Nucl. Soc., 692, 141-148.

Kim, E.S., Oh, C.H., and Sherman, S., 2008. Simplified Optimum Sizing and Cost Analysis for Compact Heat Exchanger in VHTR. Nucl. Eng. Des., 238, 2635-2647.

Kim, I.H., 2012. "Experimental and Numerical Investigations of Thermal-hydraulic Characteristics for the Design of a Printed Circuit Heat Exchanger (PCHE) in HTGRs," Doctoral dissertation, Korea Advanced Institute of Science and Technology.

Koch, 2013. Koch Industries website, http://www.kochheattransfer.com/products/twisted-tube-bundle-technology

Kim, I.H., No, H.C., 2012. "Physical model development and optimal design of PCHE for intermediate heat exchangers in HTGRs." Nucl. Eng. Des., 246, 243-250.

Lamarsh, J., Baratta, A., 2001. "Introduction to Nuclear Engineering," third ed., Prentice Hall, Upper Saddle River.

Losier, C.R.D., Subramanian, S., Ponyavin, V., Chen, Y., Hechanova, A.E., Peterson, P.F., 2007. "The Parametric Study of an Innovative Offset Strip-Fin Heat Exchanger," J. Heat Trans., 129, 1453-1458.

Manglik, R.M., Bergles, A.E., 1995. "Heat Transfer and Pressure Drop Correlations for the Rectangular Offset Strip Fin Compact Heat Exchanger," Exper. Thermal Fluid Sci., 10, 171-180.

Mylavarapu, S., Sun, X., R.R., Glosup, R.E., and Patterson, M.W., 2011, "Fabrication and Design Aspects of High-Temperature Compact Diffusino Bonded Heat Exchangers," Nucl. Eng. Des., published on-line, doi:10.1016/j.nucengdes.2011.08.043.

Mylavarapu, S.K., 2011. "Design, Fabrication, Performance Testing, and Modeling of Diffusion Bonded Compact Heat Exchangers in a High-temperature Helium Test Facility," Doctoral dissertation, The Ohio State University.

Oh, C.H., Kim, E.S., 2008. Heat Exchanger Design Options and Tritium Transport study for the VHTR System, INL/EXT-08-14799, Idaho National Laboratory, Idaho Falls, ID.

Ragheb, M., 2013. "Loss of coolant accident, LOCA," University of Illinois at Urbana-Champaign, IL.

Sabharwall, P., Patterson, M., Utgikar, V., Gunnerson, F., 2010. Phase change heat transfer device for process heat application. Nucl. Eng. Des., 240, 2409-2414.

Sabharwall, P., Utgikar, V., Tokuhiro, A., Gunnerson, F., 2009. Design of liquid metal phase change heat exchanger for next generation nuclear plant process heat application. J. Nucl. Sci. Technol., 46(6), 534-544.

Silaipillayarputhur, K., Idem, S., 2011. Step Response of a Single-Pass Crossflow Heat Exchanger with Variable Inlet Temperatures and Mass Flow Rates. *ASME 2011*, Denver, Colorado, November 11-17, 2011, International Mechanical Engineering Congress & Exposition.

Smith, E.M., 2005. "Advances in Thermal Design of Heat Exchangers: A Numerical Approach," Wiley, England.

Srinivasan, V., 1993. "Experimental and numerical investigation of heat transfer and pressure drop in flow through spirally fluted tubes." Doctoral dissertation, The Ohio State University.

Techo, R., Tiekner, R.R., James, R.E., 1965. An Accurate Equation for the Computation of the Friction Factor for Smooth Pipes for the Reynolds Number. J. Appl. Mech., 32, 443.

Wenlong, L., Heng, X., Zuoyi, Z., Yujie, D., 2012. "Development and primary verification of a transient analysis software for high temperature gas-cooled reactor helium turbine power system," Nuc. Eng. Des., 250, 219-228.

Williams, D.F., Toth, L.M., Clarno K.T., 2006. "Assessment of Candidate Molten Salt Coolants for the Advanced High-Temperature Reactor (AHTR)," ORNL.TM-2006/12, Oak Ridge National Laboratory, Oak Ridge, TN.

Wright, S.A., Vernon, M.E., Pickard, P.S., 2006. "Concept design for high temperature helium Brayton cycle with interstage heating and cooling." Sandia National Laboratories.

Zukauskas, A.A., Kakac, S., Shah, R.K., and Aung, W., 1987. "Convective Heat Transfer in Cross Flow," in *Handbook of Single-Phase Convective Heat Transfer*, Eds., John Wiley & Sons, New York, Ch. 5.

Quad Chart

U.S. DEPARTMENT OF ENERGY

Nuclear Energy

Advanced Reactors-Intermediate Heat Exchanger (IHX) Coupling: Theoretical Modeling and Experimental Validation

OVERVIEW

Purpose: The goal of the proposed research is to model the behavior of the Advanced Reactor-IHX-Chemical Process/Power Generation system and develop advanced control techniques (based on genetic algorithms or neural networks) for off-normal conditions

Objectives: 1. To develop the steady-state thermal hydraulic design of the IHX;
2. To develop mathematical models to describe the advanced nuclear reactor-IHX-chemical process/power generation coupling during normal and off-normal operations, and to simulate models using a multiphysics software such as COMSOL Multiphysics;
3. To develop control strategies using genetic algorithm or neural network techniques and couple these techniques with the multiphysics software; and,
4. To validate the models experimentally using the High Temperature Helium Facility (HTHF) at Ohio State University (OSU).

IMPACT

Logical Path: System models will be developed for the reactor-IHX system, initially for normal operation and then for off-normal conditions. The models will be validated experimentally, and control strategy developed for the system. The models developed be further validated experimentally and refined on the basis of the obtained data.

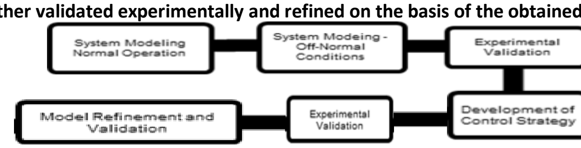

Outcomes: The project will provide information on the thermal designs and advanced control strategies for different IHXs for various operating conditions. Experimental data and information obtained through the research will be valuable in understanding the coupled response of the reactor-IHX system to various transients and in the development of intelligent control systems for the next generation nuclear reactor systems. The graduate students working on the project, mentored by University faculty and National Laboratory Personnel, will represent valuable addition to nation's nuclear workforce.

DETAILS

Principal Investigator: Vivek Utgikar

Institution: University of Idaho (UI)

Collaborators: OSU: Xiaodong Sun, Richard Christensen; INL: Piyush Sabharwall

Duration: 9/10/2012 – 9/30/2016 **Total Funding Level:** $711,947.00

TPOC: Michael McKellar

Federal Manager: Carl Sink

Workscope: NGNP-2

PICSNE Workpackage #:
NU-12-UI-ID-0302-04

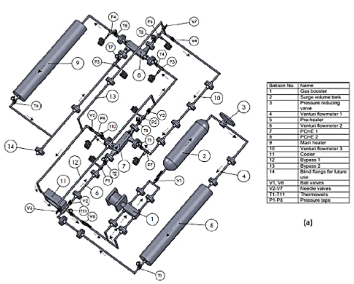

RESULTS

Results:

1. Steady state thermal hydraulic designs developed for the candidate intermediate heat exchangers. 2. Transient behavior of the system simulated for various flow and temperature disturbances using commercially available process simulation software as well as user developed MATLAB programs. 3. Control system architecture developed for the system, and the behavior of the controlled system simulated for various system disturbances. The simulation results demonstrated the effectiveness of the controllers in maintaining the system at the desired operating set points. 4. Prototype heat exchangers were designed and fabricated for experimental testing. The heat exchangers were installed in the experimental facilities and subjected to steady state and dynamic test conditions. The agreement between the experimental results and simulations confirmed the validity of the developed models.

Accomplishments:

1. The research has resulted in 6 refereed journal publications, with two additional publications in process.
2. Various aspects of the research have been presented at technical meetings of professional societies nationally and internationally through 11 presentations.
3. Two graduate students have been mentored to completion of their graduate degrees in chemical and nuclear engineering.